TECHNISCHE UNIVERSITÄT WIEN
Vienna University of Technology

Institute of Sensor and Actuator Systems

Diploma Thesis

Feasibility Study of the Use of Autonomous UAVs in Steel Plants

Johannes Pagitsch

Matr.-Nr. 01226599

Supervisor: Ao.Univ.Prof. Dipl.-Ing. Dr.techn. Franz Keplinger

Assistant Supervisor: Dipl.-Ing. Gregor Lammer, RHI AG

September 2017

Abstract

The process of steel making has been explored exhaustively and can be controlled very well in today's steel plants. Nevertheless, it is rather complex as it depends on many parameters which may not be obvious for people not being experts on this topic. One of these parameters is the quality and state of refractory. Refractory is needed to line vessels containing liquid steel so that they can withstand the extreme temperatures. Since it is stressed thermally, mechanically and also chemically, the refractory lining wears out by the time and has to be renewed. A good knowledge of the current refractory wear is absolutely necessary for the operator of the steel plant to be able to optimise the process time and maximise output. The remaining lining thickness is usually determined with time-of-flight laser measurements. Although there are specialized laser scanners used, which enable to measure the inner surface of a vessel at the harsh environmental conditions, the results are not satisfying. This is not at least because there is a lot of human intervention necessary to operate the measurement device, which leaves margins for many errors. An aim in a research project of RHI AG, a company which is world leader in refractory production, is to completely automatise the laser measuring procedure. One possible approach is to carry the measurement device with an autonomous UAV, which would provide the highest flexibility that can be achieved. The goal of this thesis is to investigate the feasibility of the realisation of this innovative approach.

Using UAVs inside a steel plant meets much more complex challenges than using UAVs outdoors.

A main challenge are the harsh environmental conditions in steel plants. Apart from extreme temperatures, there are very dusty areas and furthermore relatively strong winds due to temperature fluctuations. As there is no measured data of these parameters available, this thesis develops mathematical models to estimate temperature and wind effects. On the basis of these models, the requirements of the UAV concerning temperature and wind resistance are classified.

The second big challenge is the automatic detection of obstacles which is inevitable to guarantee safe operation of the autonomous UAV. In this thesis, an overview of available systems and technologies is given and as a conclusion, the specific systems are rated based on their most relevant characteristics. Furthermore, a sonar-based obstacle detection system is developed and evaluated to get a better view on typical problems that may occur.

The third issue is navigation of the UAV in a steel plant. The problem is that there are no GPS signals available inside. As a result, an alternative system has to be found. The main requirement is an extremely high positioning accuracy, which is necessary to enable a precise laser measurement. The thesis examines systems with both high and low state of development from different perspectives. Again, a short conclusion points out the most promising technologies.

Zusammenfassung

Die mit der Produktion von Stahl einhergehenden chemischen und physikalischen Vorgänge sind äußerst gut erforscht und können in modernen Stahlwerken sehr gut gesteuert und beeinflusst werden. Dennoch ist die Prozesskette sehr komplex und hängt von vielen Faktoren ab, die von wenig sachkundigen Personen auf den ersten Blick eher nicht in Betracht gezogen würden. Ein Beispiel für diese Faktoren ist die Qualität bzw. der Zustand des Feuerfestmaterials. Damit werden Gefäße, welche flüssigen Stahl beinhalten, ausgekleidet, um den extremen Temperaturen widerstehen zu können. Da das Feuerfestmaterial hoher thermischer, mechanischer und chemischer Beanspruchung ausgesetzt ist, nützt es sich mit der Zeit stark ab und das Gefäß muss neu ausgekleidet werden. Für den Stahlwerksbetreiber ist das Wissen über den aktuellen Abnützungsgrad essentiell, da er damit die Prozesszeiten optimieren und dadurch die Produktionsmenge maximieren kann. Nach aktuellem Stand der Technik wird die sogenannte Reststeinstärke, also die noch vorhandene Dicke der Auskleidung, mittels Laserlaufzeitmessungen bestimmt. Die dazu verwendeten Geräte sind auf diesen Anwendungsfall spezialisiert und können die innere Oberfläche eines Gefäßes unter den vorliegenden extremen Umweltbedingungen messen. Trotzdem sind die Ergebnisse der Messungen nicht zufriedenstellend genau. Das liegt nicht zuletzt daran, dass das Messgerät von Menschenhand bedient werden muss, was großen Spielraum für diverse fehlerhafte Einflüsse lässt. Das Teilziel eines Forschungsprojektes des Feuerfestherstellers RHI AG ist es, den Messvorgang weitgehend zu automatisieren. Ein möglicher Ansatz dafür ist die Montage des Lasermesskopfes auf ein unbemanntes Flugobjekt (Drohne), was sehr viel Flexibilität im Hinblick auf die Messung mit sich bringen würde.

Ziel dieser Arbeit ist es, die Machbarkeit der Realisierung dieses Ansatzes zu prüfen. Der Einsatz von Drohnen in einem Stahlwerk bringt viel mehr Herausforderungen mit sich als der Einsatz im Außenbereich, wo Drohnen momentan schon sehr erfolgreich für eine Vielzahl von Aufgaben verwendet werden.

Eine der größten Herausforderungen sind die außerordentlich rauen Umweltbedingungen in Stahlwerken. Abgesehen von extremen Temperaturen gibt es dort sehr schmutzige und staubige Bereiche sowie nicht zu vernachlässigbaren Wind, der durch die großen Temperaturschwankungen verursacht wird. Da keine Messwerte der genannten Parameter vorliegen, werden in der Arbeit mathematische Modelle entwickelt, um die Temperatur und den Einfluss des Windes auf eine Drohne abzuschätzen. Basierend auf diesen Modellen werden die Anforderungen der Flugdrohne bezüglich Temperatur- und Windresistenz definiert.

Eine weitere Herausforderung ist die automatische Detektion von Hindernissen. Diese ist unabdingbar, um einen sicheren Betrieb des Messsystems zu gewährleisten. Die vorliegende Arbeit gibt einen Überblick über diverse vorhandene Systeme und Technologien zur Hinderniserkennung. In einer kurzen Schlussfolgerung werden die Systeme anhand der relevantesten Eigenschaften bewertet. Weiters wird ein ultraschall-basiertes Hinderniserkennungssystem gebaut und dessen Leistungsfähigkeit beurteilt. Ziel ist es,

dadurch einen besseren Einblick in typische Probleme derartiger Aufgaben zu bekommen.

Zum Dritten stellt sich die Frage, wie man die Flugdrohne durch das Stahlwerk navigieren kann. Ein herkömmliches GPS kann dafür nicht in Betracht gezogen werden, da in Innenräumen keine ausreichend starken GPS-Signale zur Verfügung stehen. Die wichtigste Anforderung an ein alternatives Navigationssystem ist eine sehr hohe Genauigkeit, da diese als Grundvoraussetzung für eine präzise Lasermessung gegeben sein muss. In dieser Arbeit werden sowohl marktreife Systeme als auch Systeme, die sich noch im Entwicklungsstadium befinden, aus verschiedenen Blickwinkeln betrachtet. Auch hier werden anschließend wieder überblicksmäßig die vielversprechendsten Technologien bewertet.

Contents

1 Introduction **1**
1.1 Steel production . . . 1
1.2 RHI AG . . . 3
1.3 APO . . . 3
1.4 State of the art . . . 5
1.5 Problem definition . . . 5

2 Development Methods for Industry 4.0 **7**
2.1 Industry 4.0 . . . 7
2.2 Visual Roadmap . . . 8
2.3 Virtual Teaming . . . 9
2.4 Industrial Internet Reference Architecture IIRA . . . 10
2.5 RAMI 4.0 . . . 11
2.6 Requirements definition . . . 13

3 Environmental Influences **17**
3.1 Thermal aspects . . . 17
3.1.1 Heat transfer model . . . 17
3.1.2 Temperature resilience . . . 29
3.2 Aerodynamic aspects . . . 33
3.3 Test flight in industrial environment . . . 37
3.3.1 Equipment . . . 37
3.3.2 Observations . . . 43

4 Obstacle Detection **47**
4.1 Available systems . . . 47
4.1.1 Single camera systems . . . 47
4.1.2 Stereo camera systems . . . 49
4.1.3 Structured light . . . 51
4.1.4 Laser . . . 52
4.1.5 Infrared . . . 54
4.1.6 Sonar . . . 55
4.2 Summary . . . 56

5 Setup and Evaluation of a Sonar Obstacle Detection System **59**
5.1 Measurement setup . . . 59
5.2 Software . . . 61
5.3 Static measurement . . . 63
5.4 Dynamic measurement . . . 69
5.4.1 Lateral movement . . . 69
5.4.2 Rotational movement . . . 73

6 Positioning and Navigation **77**
6.1 Available systems . . . 77
6.1.1 Dead reckoning . . . 77
6.1.2 UWB . . . 80
6.1.3 Further RF-technologies . . . 82
6.1.4 Optical systems . . . 83
6.1.5 Ultrasound systems . . . 86
6.1.6 Cameras . . . 87
6.1.7 Pseudolites . . . 88
6.2 Summary . . . 89

7 Conclusion and Future Outlook **91**

List of Abbreviations **96**

List of Tables **97**

List of Figures **100**

Bibliography **108**

1 Introduction

1.1 Steel production

Steel is a metallic alloy which primarily consists of iron. In contrast to cast iron, steel can be transformed mechanically (e.g., rolled). Depending on the desired properties of the produced steel (e.g., hardness or rust resistance), different alloying elements are added during production, whereas the most important one is carbon. The amount of carbon in steel is less than 2 %.

In today's steel plants both steel producing and steel processing are performed. The former refers to the path of making steel out of iron ore and scrap. The corresponding steps and methods are described below. The latter encompasses a multitude of reshaping procedures, however providing steel in defined properties and shapes (e.g., plates, bars or rails [53]) is not relevant in the context of this thesis.

There are primarily two ways to produce steel. About 70 % of the globally manufactured steel is produced on the process route from blast furnace to oxygen converter [20]. At the beginning of the process, raw iron is made out of iron ore and coke. This step usually takes place in a blast furnace. Iron ore in the form of pellets or sinter, coke and other components (e.g., SiO_2 or CaO) are mingled and poured into the furnace. Afterwards, preheated air is blown into it and the coke burns. Heat and carbon monoxide are released and the iron ore is reduced. The reaction products are raw iron and slag, which are periodically tapped. In the next step, the raw iron has to be refined by blowing air or oxygen on it. There are several processes for this purpose, however the most common one is the Linz-Donawitz process (LD process), which is sometimes also called basic oxygen furnace (BOF) process. In this process, fluid raw iron and about 20 % iron scrap are given into a so-called BOF or oxygen converter. Through a water-cooled lance, oxygen is blown on the melt and impurities in steel, such as phosphorus, sulphur or carbon, are removed.

Due to the high cost of coke and massive production of carbon-dioxide, there are ambitions to replace the reduction process in the blast furnace by another process called direct reduction. The reaction product of a direct reduction is a porous alloy with a concentration of iron of about 92 - 95 % which is called directly reduced iron (DRI) or sponge iron. However, until now no direct reduction process has been able to completely replace the blast furnace.

The second steel-making process, which covers the remaining 30 % of the whole amount of produced steel, is called electric-arc-furnace process (EAF process). For this process, steel scrap and sponge iron are melted with an electric arc. There are two types of EAFs: an AC- (alternating current) and a DC-EAF (direct current). In an AC-EAF the electric arc is generated between three graphite electrodes which are fed with three-phase current. In a DC-EAF the electric arc is generated between the anode in the bottom of the furnace and the cathode above the metal. Due to the fact that electric arcs with temperatures up to 3500 °C can be generated, every kind of steel can be produced because even alloys with high-melting metals like wolfram or molybdenum are possible. Since production

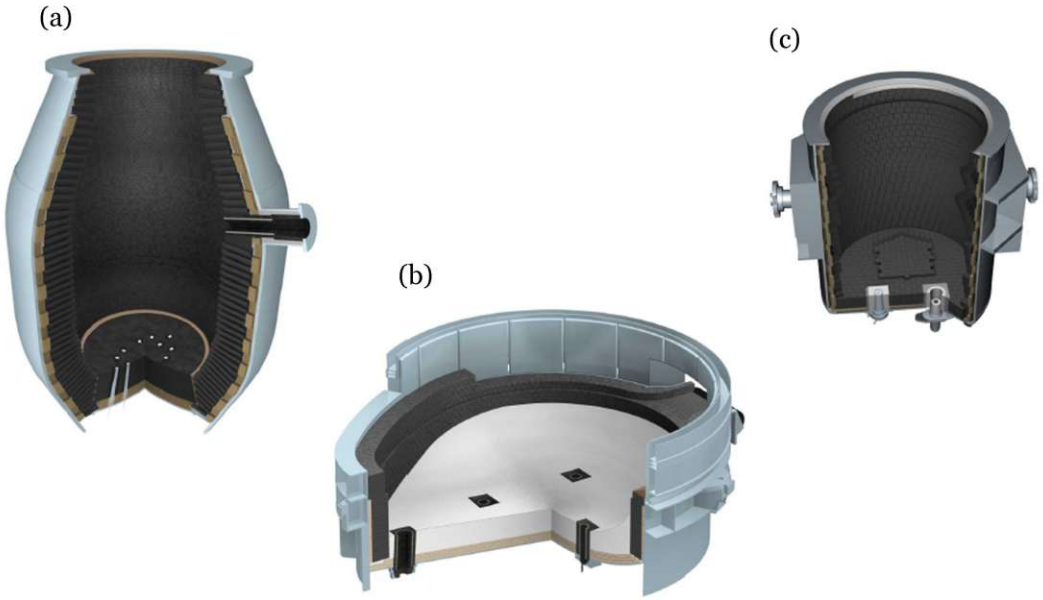

Figure 1.1.1: Lined vessels: basic oxygen converter (BOF) (a), electric arc furnace (EAF) (b) and ladle (c). The black material is the refractory [75].

cost is very high, the EAF-method is only used for the production of high-quality- and high-grade-steel [95].

The reaction temperatures of iron- and steel-production processes are between 1200 and 2500 °C. For this reason, all vessels and machines that are needed to transport or process steel have to be lined with refractory. These are ceramic materials with high temperature resistance. Figure 1.1.1 shows an EAF, a BOF and a ladle (vessel to transport liquid steel) that are lined with refractory. There are three influencing factors which lead to refractory wear:

- thermal stress
- mechanical stress (erosion)
- chemical stress (corrosion and oxidation)

Once the refractory layer becomes too thin, the vessel has to be lined with new bricks to avoid breakouts of liquid steel. As the vessel has to cool down for this purpose, it is a rather time-consuming and costly procedure. That is why every steel plant operator is interested in maximizing the duration of a campaign (a campaign is the time difference between two complete exchanges of the refractory lining). For this reason, many steel plants apply maintenance processes. The amount of maintenance that is performed is different in every steel plant. Some repair the lining after every heat (the process of oxidising raw iron is called “heat”), others do not apply maintenance at all.

The most flexible way of doing maintenance is so-called gunning repair or gunning maintenance. It can be applied for oxygen converters and ladles as well as EAFs. In the first step, it has to be determined which areas of the lining are damaged. This is not as easy as it seems to be, because maintenance is done immediately after tapping and

therefore the vessel is still very hot and glowing. Currently, special laser scanners are used to scan the vessel's inner surface. In the next step, a steel worker has to repair the lining by remote controlling a so-called gunning manipulator – a vehicle with a moveable nozzle mounted on a lance. With this machine, refractory shotcrete is gunned onto damaged lining areas (see figure 1.1.2). The whole process may only last for a few minutes so that

Figure 1.1.2: Manual gunning maintenance of a ladle. The gunning manipulator is remote controlled by the steel worker. The machine needs a heat shield, because the empty ladle is still extremely hot [96].

the vessel does not cool down too much and a new heat can be started immediately after maintenance.

1.2 RHI AG

RHI AG is a manufacturer of refractory products and provider of services all over the world with customers primarily from the steel industry. The group has nearly 100 sites for production and service worldwide and employs about 7500 people. Its annual revenue accounts for nearly 2 billion euro. About 2 million tons of refractory material are sold per year. RHI products are mainly based on magnesite and dolomite which is mined to 80 % in the group's own mines. Therefore, the company is widely independent of the raw material's market prices. About 1 % of RHI's annual revenue is invested in research and development (R&D), which is why the company can steadily build a growing understanding of the behaviour of its refractories in the application processes [19]. This thesis was written in the context of an R&D project called Automatic Process Optimisation (APO), which will be described in section 1.3.

1.3 APO

As mentioned in section 1.1, the whole maintenance process including laser measurement and gunning is done manually. This has several disadvantages. On the one hand the execution of these tasks is very dangerous. The steel worker stands closely to the vessel

and is exposed to very hot temperatures due to heat radiation. On the other hand, there are a lot of possible errors that can be made during a laser measurement (e.g., positioning the laser measurement device incorrectly). Furthermore, manual gunning cannot be done very properly. It is very difficult to steer the nozzle exactly to the damaged areas based on the laser measurements that have been done beforehand, because one cannot see directly inside the vessel because it is very bright due to the high temperature. Hence, the actual shotcrete layer thickness can only be estimated, which requires a lot of experience on the part of the steel worker.

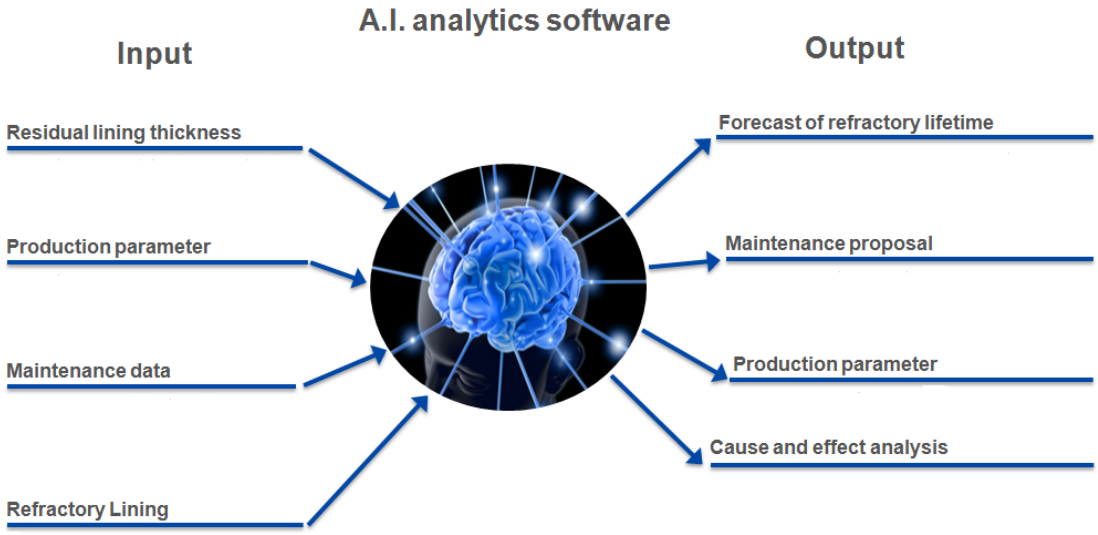

Figure 1.3.1: Input- and output-parameters of APO. The core of the system is an analytics software module with artificial intelligence and machine learning algorithms [64].

To compensate all these disadvantages of manual maintenance, an Automated Process Optimisation (APO) is developed by RHI. As its name implies, the aim of APO is to automate and optimise the whole maintenance process. The input- and output-parameters are shown in figure 1.3.1. The **residual lining thickness** is measured with the laser scanner. It is the same data which is currently used for the manual maintenance process. The **production parameters** describe further parameters of a heat which are relevant for refractory wear. These parameters are, e.g., tapping temperature and the re-blow rate of oxygen in a BOF. The **maintenance data** describes parameters of the gunning process itself, like the amount of gunned shotcrete. The **refractory lining** describes relevant aspects of the current condition of the lining, as for example the quality of the refractory bricks and the lining design (there are several ways to arrange bricks in a vessel). Based on a complex model and machine learning and artificial intelligence analytics methods, the APO-outputs are created. A **forecast of refractory lifetime** tells the customers the remaining lifetime of refractory without further maintenance. A **maintenance proposal** gives the customers information about the necessary maintenance to reach a targeted lifetime (e.g., required gunning time or required quantity of shotcrete). In relation to these two aspects, the customers can decide whether to start a fully automated maintenance process or not. The output-sided **production parameters** identify the most impor-

tant conditions that are relevant for refractory wear. This gives steel plant operators the possibility to extend refractory lifetime by adapting their production processes. To gain information about improvement and development of refractory material, a **cause and effect analysis** is done, which aims at a holistic understanding of refractory wear mechanisms [64]. In addition to the data output, APO provides a completely automated and optimised operation of the gunning manipulator.

1.4 State of the art

The results of the laser measurements are an input to APO which strongly depends on human interaction and is at the same time very fundamental for a correct functionality of the whole process. To avoid malfunction of the system due to human errors, a device should be developed which allows to automate this step. One approach is to use an unmanned aerial vehicle (UAV) (note: in this thesis, the terms "UAV", "drone" and "multicopter" are used synonymously) to carry the laser measurement system to the necessary measurement points in a steel plant. Besides the possibility of an autonomous measurement, this would entail further advantages. The quality of the measurement could be improved as there always occur shading effects due to the vessel's shape (see also figure 1.1.1) in current measurements. With the measurement system on a drone, a vessel could be scanned from several spots and the shading effects could be removed. Additionally, the drone could be used to carry not only a laser scanner but also gas measurement equipment. In steel plants it is required to measure various gas emissions regularly and prepare a gas emission report. A further possible application would be the use of the drone for monitoring activities in dangerous areas.

The requested system consists of two main parts:

- **Drone**: its tasks have already been described above. The most important property is the drone's autonomy. It does not make sense to remote control the drone, because the autonomy-grade of APO would not be improved. For the same reason, the drone should have no or almost no maintenance requirements. When the drone is not flying it should be deployed in a

- **Base station:** this is a dust-protected area with several specialities. There should be an autonomously opening and closing gate to let the drone in and out and guarantee dust-protection at the same time. Furthermore, the base station should provide an interface which allows to load the measured data from the drone in the base station and in further consequence on an RHI data server. The base station should also contain a battery charger which automatically plugs when the multicopter enters.

1.5 Problem definition

The aim of this thesis is to carry out a feasibility study of the use of an autonomous drone in a steel plant. This thesis is not going to concentrate on the implementation of the base station as this task is much easier compared to the automation of a drone.

One main challenge are the environmental conditions in a steel plant which are much harsher than in other areas where UAVs are already used successfully. Temperature in steel plants can be extremely high as well as extremely low. Steel plants are usually open

on the side to a certain part, which means that the average temperature inside is about the same as outside. The temperature can for example go up to 40-50 °C somewhere in a steel plant in a desert region and on the other hand, steel plants in cold regions may have an inside temperature way below 0 °C. Furthermore there are extreme temperature fluctuations as temperature is extremely high near vessels containing liquid steel. These fluctuations may cause strong winds and turbulences of the air inside a steel plant. These conditions and their effects on a UAV are discussed in chapter 3.

Furthermore, there are extremely dusty and dirty areas in steel plants and the illumination is rather poor. This makes it challenging to find a suitable system to detect obstacles in the multicopter's way, which is essential for safe operation. Chapter 4 discusses some possible systems and evaluates their performance.

A third challenge is the navigation of the drone. The most commonly used GPS is not available and therefore it is necessary to find alternative possibilities (chapter 6).

At first, the system requirements have to be developed with respect to the desired functionalities of the autonomous drone as an Industry 4.0-device. This is done in chapter 2 with an innovative architecture model specialised on Industry 4.0-applications.

2 Development Methods for Industry 4.0

To discover the feasibility of a product or process, it is necessary to have a rather clear idea of the product's specifications and properties. In this section some modern product development methods are discussed and one specific method is used to build a model describing the autonomous drone. This will pave the way to test the feasibility of its features in the following sections.

2.1 Industry 4.0

In its origins, the term "Industry 4.0" was invented by the German "Forschungsunion" as a strategy to boost technological progress and cope with the upcoming digitisation. By the time, the term has been used in highly diverse contexts and interpreted in different ways, which makes it nowadays quite difficult to exactly define what Industry 4.0 stands for. Originally, Industry 4.0 describes the Fourth Industrial Revolution.

The First Industrial Revolution started about 200 years ago when machines were used for mass production for the first time. The first manufacturing facilities were built and water- and steam power were used to drive machines. Thus, many industrial sectors, as coal mining, heavy industry or the textile industry, could rise up to new dimensions.

The Second Industrial Revolution began with the advent of electricity at the end of the 19^{th} century. Various factories expanded the grade of automation in their production line, first automobiles were built and the focus on mass production grew due to the principle of division of labour. Through the invention of telecommunication systems, first steps in the direction of globalisation were done. These changes did not only affect technology but also the trading sector.

The Third Industrial Revolution started in the 1970s when the usage of computers became more and more easy and the computers' performance was rising steadily. Due to the growing number of sold personal computers, a new industrial sector developed.

The Fourth Industrial Revolution focuses on digitisation of systems that were primarily analogue in former times. Electronic devices are interconnected through cyber-physical systems which enables new ways of communication on the one hand and more flexibility on the other hand. Furthermore, products and systems communicate more and more interactively with the user which often facilitates human intervention [48].

Besides the outstanding amount of new possibilities, Industry 4.0 also leads to more and more complex systems. The users do not realize this in most cases, as user-friendliness is one important aspect of Industry 4.0-systems. In fact, the product developers are the ones who have to meet this challenge. Many methods and models that were used to design and develop products without Industry 4.0-properties cannot be used any more as they are too simple and don't face all the different aspects. Thus, the need of new methods and models arises.

2.2 Visual Roadmap

The method of Visual Roadmapping was developed by the German "Institute for Innovation and Technology" (IIT) and is based on the traditional and well established method to plan the way of developing a product with a roadmap. A roadmap is a graphical depiction describing a development process from its beginning to its end. Usually this is done in one dimension: the different processes and stages during product development are arranged along a timeline. The additional issue in visual roadmaps is a second dimension to divide the aspects of single process steps into content-related subareas.

The process of visual roadmapping is carried out within the scope of an expert discussion, however the roadmap can also be developed by a single expert [10].

In [48], a roadmap for Pervasive Computing is presented (see figure 2.2.1). Pervasive

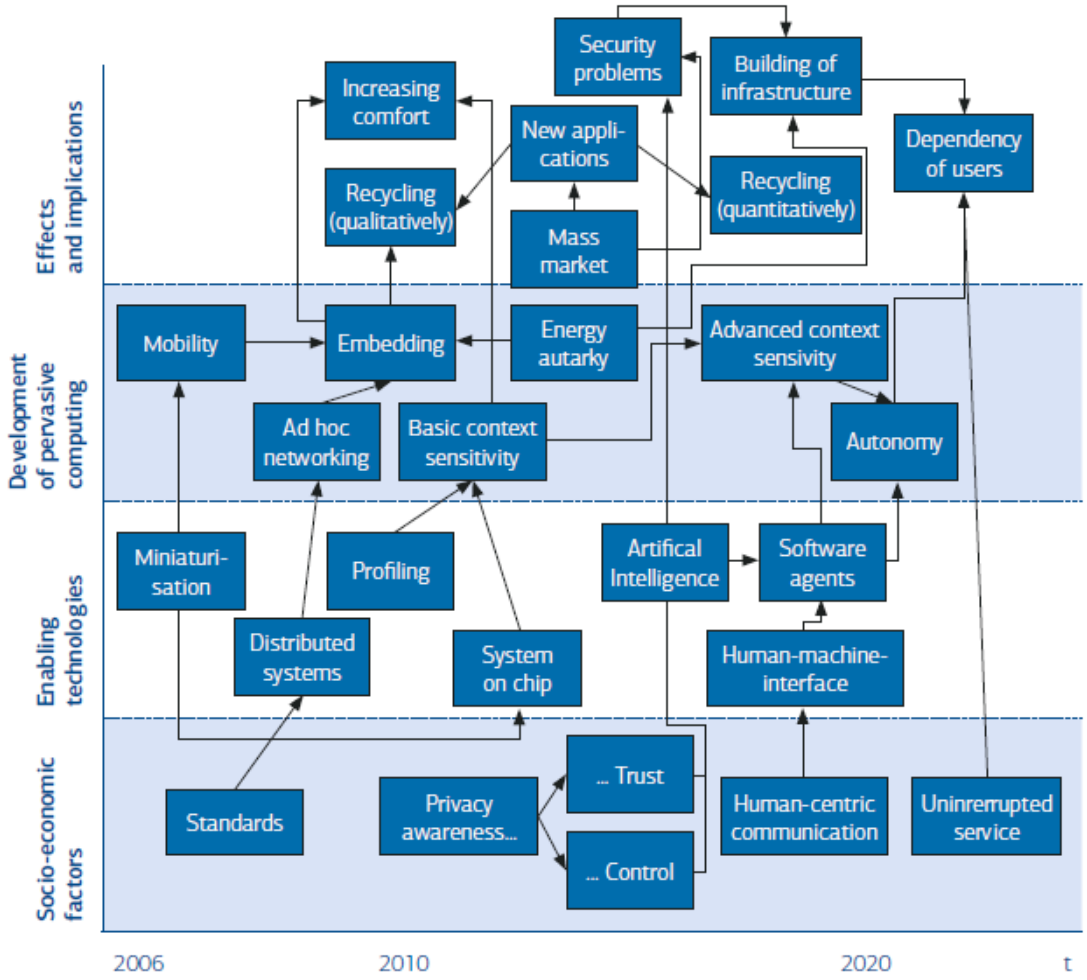

Figure 2.2.1: Visual roadmap for Pervasive Computing. The ordinate represents special aspects of different process steps, the abscissa shows the timeline. Components are represented by the blue rectangles. Specific paths during product development are represented by arrows [48].

Computing is a term describing the pervasive interconnection of everyday life with "intelli-

gent" objects. In the roadmap, socio-economic factors, enabling technologies, development of production technologies and effects and implications are considered in the second dimension. The diagram can be read by following the paths given by arrows. E.g., privacy awareness is an important socio-economic factor of Pervasive Computing. This is because the intelligent object takes over control of a specific task in the user's life which should not lead to the loss of the user's confidence and trust. Such an issue somehow has to be considered when using the upcoming technology of artificial intelligence in a software agent. Artificial intelligence leads to new security problems which raises the need of new infrastructure which will in the end influence the dependency of the users.

To represent this path more vividly, autonomous driving is taken as a specific example. It is obvious that autonomous driving takes over **control** of an everyday activity. Car accidents caused by humans have an astonishingly high social acceptance, however the same is not applicable for accidents of autonomous cars. Hence, autonomous cars have to provide extremely high safety. This means that the amount of car accidents caused by autonomous cars has to be 0 %, otherwise people will soon lose confidence in the technology. To achieve this goal, **artificial intelligence**, e.g., self-learning algorithms, can be used. These algorithms are able to take decisions on their own (based on a huge data set) and therefore arise new **security problems**. In this example, a narrow street with a wall to its left and right is assumed. A car with a pregnant woman inside is overtaken by a car with three teenagers. A truck is coming towards them and halting is no longer possible. It is in the computer's responsibility to decide with which car the truck is going to crash (note: the MIT-platform "Moral Machine" is gathering similar scenarios of moral decisions of machine intelligence). One possibility to cope with this problem is to **build infrastructure**. In this case, the situation could have been avoided if all three vehicles had been fully autonomous and if there had been additional communication infrastructure between them. Thus, the computer could have foreseen the occurrence of a crash and the three teenagers would not have been able to overtake the car with the pregnant woman. This would of course have the effect that the **dependency of users** on the technology increases.

All in all, Visual Roadmapping is a simple, cheap and flexible tool to support product developers. Nevertheless, even for simple product development processes it may soon become unclear and confusing. Furthermore, in its core it is still a very conventional method and in many cases more advanced possibilities would be helpful.

2.3 Virtual Teaming

Especially in international companies a strong development of so-called Virtual Teams can be observed. A Virtual Team is neither artificial nor unreal, as the designation may suggest. In fact, it is an organisational form with its members working together temporarily (in some cases also continuously), on different locations, at different times and across company boundaries but with the same goals. Virtual Teams are in general more flexible than "real" teams, they can be built quickly and have in most cases a diverse know-how [67]. In the literature there are numerous tests and studies to verify the effectiveness of Virtual Teams in product development. A good overview of the main advantages of Virtual Teams can be found in [44]. Some insights are given below:

- Virtual Teams reduce time-to-market significantly. Therefore cost is reduced as well.
- The team outcomes are better than in "real" teams. This means that quality and productivity as well as satisfaction of the team members increase.
- Information exchange is more formal. This means that less socio-emotional information is exchanged and the team tends to be more task oriented.
- Decisions of R&D continuation are more effective.
- Virtual Teams attract better employees and can generate competitive advantage from limited resources.

Virtual Teaming is not a development method in the narrower sense but rather an innovative form of project coordination. It will not be needed in the course of this thesis, however it is mentioned for the sake of completeness as it can often be found together with Industry 4.0-product development approaches.

2.4 Industrial Internet Reference Architecture IIRA

A very common practice to structure and categorize new products or software architectures is the use of layer-based reference models. The idea is to divide a complex system into different aspects which are represented by one layer each. The dependencies between the aspects are restricted in a way that aspects in a higher layer are only allowed to use aspects of lower layers. Depending on the described system and the level of detail of the consideration, the aspects assigned to a layer can either be a functionality, a component or, which is more abstract, a class. A layer-model reduces the system's complexity and especially the complexity of the dependencies in the system. This brings clear advantages for the understanding of the system and later on also for maintenance: occurring errors and malfunctions can be localised and repaired faster. Conventional layer models primarily differ in the number of layers. Easy systems can be depicted in two-layer models which are often also called client-server models. This is because of the rule that only the higher layer has access to the lower layer and therefore the lower layer is the service provider of the upper layer [77]. The more complex systems become, the more layers are needed.

There are many examples for layer-based reference models. The most popular one may be the OSI-model (Open Systems Interconnection model) which is a reference architecture for network protocols. Besides the already mentioned purposes, another important aim of this model is standardisation. It should ensure that communication is possible among different technical systems using the same network protocol [41].

The area of application of layer models is not restricted to software systems as discussed above. On the contrary, modern layer model approaches tend not to make a clear difference between a system's hardware and software part but see it as a whole unit. A model which was especially designed for Industry 4.0-applications is the so called IIRA-model (Industrial Internet Reference Architecture model). It was first published in 2015 by the IIC (Industrial Internet Consortium) and aims at supporting system design based on a common framework and on common concepts [18]. The core of the IIRA-model are the four layers (often also called "viewpoints") implementation, function, usage and business.

The implementation layer is located on the bottom of the layer stack. It deals with technologies that are used to implement the functional components of the modelled system. Furthermore, lifecycle procedures and communication schemes of the components are considered.

The functional layer describes the functional components in the system. It doesn't focus on their implementation but rather on their general structure, interrelation and the interfaces and interactions between them. This layer also contains the interaction with external systems.

The usage layer describes how a system is used. Usually sequences of activities of a user (this can either be a human or, in case of modelling a subsystem, another system) are employed to depict the functionality. A remarkable feature of this layer is that it does not only aim at product developers but also at other stakeholders like those who have to specify and verify the product's function during the test phase.

The business layer is the top layer and describes how a system can be used as part of a business model. Similar to the usage layer, also stakeholders who do not stand in a direct connection to product development are involved. As this layer is strongly business-orientated, it involves business decision-makers as well as, of course, product managers and system engineers [66].

Besides the layers or viewpoints, the IIRA-model consists of two further parts. One part is a set of the key system characteristics that have to be considered. These are issues like reliability, user friendliness or maintainability. The other part are the so-called key system concerns that embrace the whole system from a more technical point of view (e.g., connectivity, data management, data processing and analytics).

All in all, the IIRA model has a wide area of application. Nevertheless, there are a few points of criticism: it is a one-dimensional layer model and neither considers the product's life cycle nor different levels of hierarchy. Considering the life cycle is helpful as the model could then not only be used during development and design phase but also during production and usage. An additional hierarchy would enable to make the different parts of the system visible and to depict how they interact with each other. In the IIRA model this has to be done implicitly. These missing points imply that the model is rather useful for software products. In software development, single stations in a product life cycle do not differ strongly (e.g., software maintenance is not a fundamentally different procedure compared with software development – in both cases the basic operation is programming). Moreover, the structure of single product components (e.g., software modules) is more or less the same – every component is a piece of program code.

This is why a different architecture model is used to specify the important aspects of the UAV.

2.5 RAMI 4.0

The abbreviation RAMI 4.0 stands for Reference Architecture Model Industry 4.0. The model was developed by the German ZVEI (Zentralverband Elektrotechnik- und Elektronikindustrie) with the idea to create a simple, vivid and flexible architecture model. A graphical representation is shown in figure 2.5.1. RAMI 4.0 is a three-dimensional model: the vertical axis (layers) represents different perspectives of the product, one horizontal

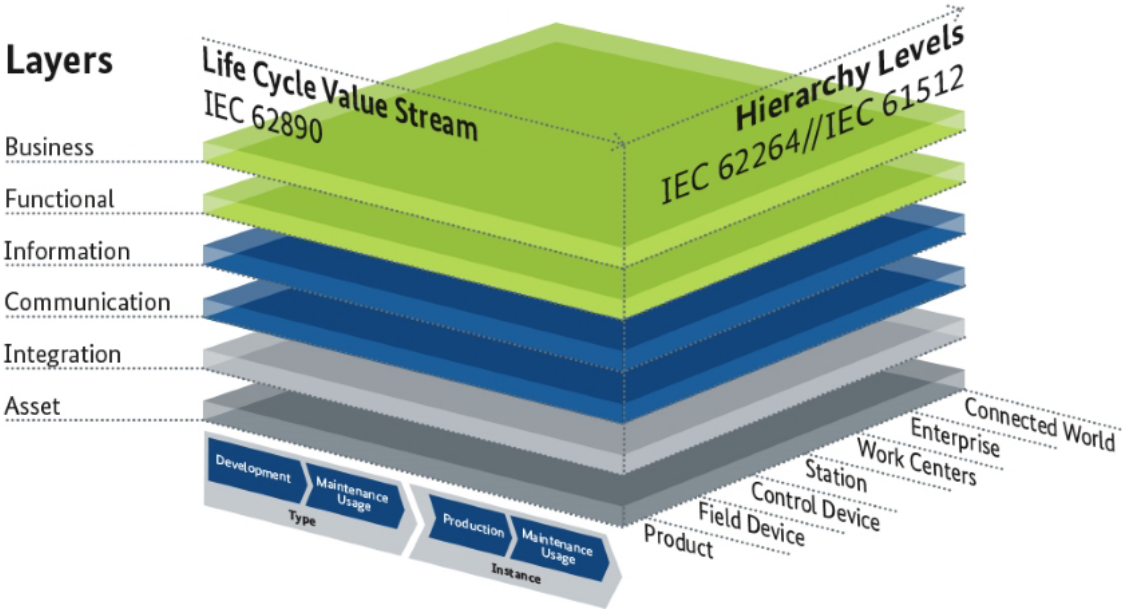

Figure 2.5.1: Reference Architecture Model Industry 4.0. The hierarchy levels represent the product and its environment, the layers represent different product perspectives [47].

axis represents the product hierarchy levels and the second horizontal axis represents the product life cycle.

The business layer depicts the business models and its resulting processes. This layer should ensure the integrity of the functions in the value chain including the juridical and regulatory parameters.

The functional layer formally illustrates the product's functions. Inside this layer, rules and decision logic are created. Properties like remote access or horizontal integration take place in this layer. This ensures integrity of information and states during development.

The information layer defines the runtime environment of information processing. In other words, the layer represents how data is processed in order to gain new, higher-order data.

The communication layer is the connection between the higher information- and the lower integration-layer. It describes the unification of communication between the two layers.

The integration layer describes the transition of the physical world to the digital world. If there is any human interaction it will happen on this layer too.

The asset layer eventually represents reality, e.g., physical elements but also documents, ideas or circuit diagrams.

On the horizontal life cycle axis, a distinction between "type" and "instance" is made. A type can be understood as the product during development phase whereas the instance is the functioning product during disposal and operation. Changes in the type also result in changes in the instance and vice versa.

The hierarchy levels are a functional classification of a thing in terms of Industry 4.0. The product-level describes the product itself (e.g., a car), the field device-level describes a specific part of the product (e.g., motor, intelligent sensor) and the control-device level describes the controller which controls the field device. In other words, these three levels are a precise specification of the product. The next three levels, namely station-, work center- and enterprise-level, describe the product's surrounding. E.g., the assets of a robotic arm in an automobile factory could be "mounting left front wheel", "assembly line 3", "car factory in Spartanburg" for "station", "work center" and "enterprise". The other layers would describe how the robotic arm is connected to the controller, how it communicates with the other components along the assembly line and so on [22].

RAMI 4.0 combines different perspectives of the user and enables to compare different products from the point of view of Industry 4.0. With the help of the model, possible gaps in the development process can be found and closed and the requirements of products of different industrial sectors (automation of manufacturing, chemistry, process engineering or mechanical engineering) can be defined and discussed. This will be done with the UAV in the following section.

2.6 Requirements definition

To be able to face the challenges of an autonomous drone in a steel plant, a clear concept of the drone's requirements is needed. In figure 2.6.1, RAMI 4.0 is applied to the autonomous UAV. As the sense of this picture is not obvious, a detailed explanation is given below. First of all, the product life cycle is not drawn in the image. This is because the intention is not to develop the drone but to find out whether its operation in a steel plant would in general be feasible. Therefore it is necessary to look at the instance, which is on the right side of the product life cycle. This also explains why the single layers are not congruent as in figure 2.5.1 but shifted against each other.

To begin with, the product-level in the horizontal axis is considered. The asset-layer describes the product itself, which is the UAV (7). The UAV can "see" the digital world via the base station (11) which can be found in the uppermost level of the asset-layer. The integration to the base station is effected by means of any wireless data transmission as for example WLAN or Bluetooth (5). The function of the drone is to carry a measurement system and to buffer the measurement data which is later on copied to a storage medium in the base station. The carrying and buffering is taken together in the term "measurement" (1) in the functional layer. The process of copying is divided into the information-, communication- and integration-layer: the information layer describes the software executing the data management (2), the communication layer describes the protocol used, which could for example be FTP (3). The integration layer eventually describes the connection to the base station, as already mentioned before. To go further on the logical part of the measurement data, the connected world level is considered next. The asset here is the base station, which gets the data from the drone after its measuring flight. The base station is connected to the digital world via Ethernet (13), the protocol is TCP/IP (14). The base station is the link between the drone and a data server of the RHI AG, so its function is to transmit the measurement data (17). The transmission is

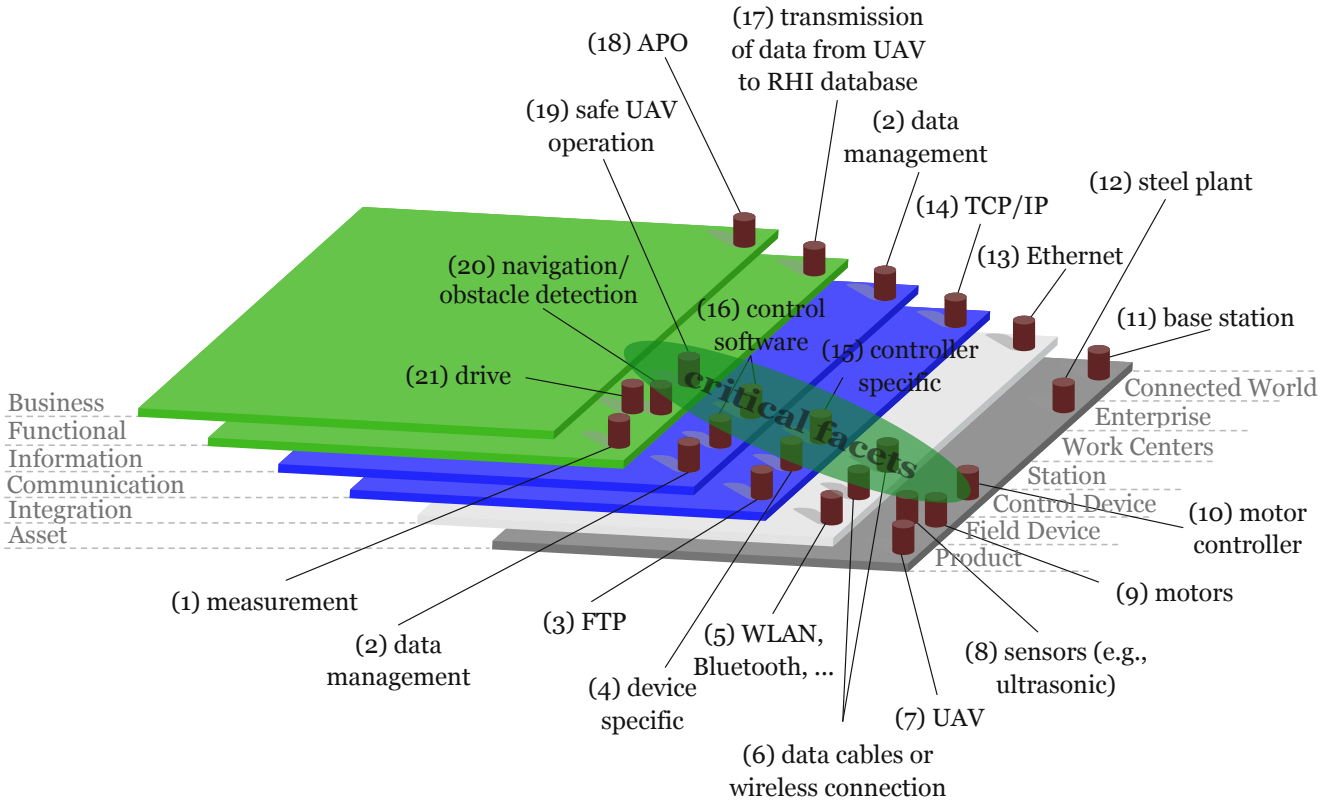

Figure 2.6.1: RAMI 4.0 applied to the UAV. The layers of the model are shifted as the development process is not considered. The critical aspects of the drone that are relevant for this thesis are marked with the green elliptical area.

again organized by any data management software (2). The connected world level is the only level with an element in the business layer. This is because the base station is the last element of the system on the way to APO (18).

The depicted configuration of RAMI 4.0 indicates the following process operation: the drone starts its flight from the base station and buffers the measurement data on any portable storage medium. It would principally also be possible to continuously transmit the data to the base station, however experience shows that wireless transmission over longer distances causes problems inside a steel plant. When the measurement is finished, the drone flies back to the base station, the data is copied to a storage medium in the base station via WLAN, Bluetooth or any other wireless transmission protocol. Wireless transmission is suited better in this case as the drone does not have to be physically connected to the base station, which would be more complicated to implement. Besides this, the amount of data to transmit is not very big (at most 90 MB per laser measurement). The base station eventually initiates data transmission to an RHI database. It would be possible to perform some data processing as for example an outlier detection and removal in the base station as well, so that the data can immediately be used as an input for APO.

The drone will be used in the whole steel plant (12), therefore the station- and work center-levels are empty. The enterprise level only contains an asset, because the steel plant itself is not connected to the digital world, or, what is more significant, it is not relevant for the drone.

Two field devices of the UAV are considered more closely: the motors (9) and the sensors (8). One could say that a drone consists of more field devices as for example the propellers. This argument is of course correct, however it should be considered that field devices as propellers or the frame do not have Industry 4.0-character. The digital world is connected to the motors and sensors via not further specified data cables or via a wireless connection (6). The bridge to the information layer is built over a device-specific communication (4) represented in the communication layer. The control software (16) in the information layer is responsible for data processing of the sensor data and furthermore establishes a connection between control- and field-devices. Finally, the function of the sensors is to enable the possibility of safe navigation and obstacle detection (20) and the motors' function is to drive the drone (21).

As it can be seen in figure 2.6.1, the motor controller's (10) features in the particular layers are quite similar to the features of the field devices. The reason simply is that in the case of an autonomous drone field- and control device have to cohere strongly. There is a data exchange between the sensors and the motor controller and of course also between the motor controller and the motors. The format how this data is given to the software is determined by the system programmer and thus controller specific (15). The motor controller ensures safe UAV operation (19), which of course also requires the field devices' functions, which are navigation and obstacle detection.

This study primarily concentrates on the green marked elliptical area in figure 2.6.1. The area covers the critical facets of the drone system, whereas "critical" means that their feasibility is not ensured.

3 Environmental Influences

3.1 Thermal aspects

Temperature is a very challenging environmental condition in steel plants. It may be assumed that temperature in steel plants is in general extremely high. This is partly correct as there are of course extremely high temperatures near hot vessels like a BOF or EAF containing fluid steel. On the other hand, steel plants are usually not completely closed for reasons of ventilation. That means that the temperature inside a steel plant also depends on the outside temperature. As a result, the temperature in a steel plant could be extremely low as well if the plant was located in a cold region. In combination with hot areas near furnaces this leads to extreme temperature fluctuations.

This section is divided into several parts. In 3.1.1, a mathematical model is developed to estimate temperatures of hotspots on possible routes of the UAV in a steel plant. This is necessary as no measurement data of these temperatures is available but their knowledge is essential to evaluate the system's feasibility. In 3.1.2, the temperature stability of the drone's components is evaluated. Section 3.2 deals with aerodynamic influences on the drone. To gain practical experience, eventually a test flight with a UAV is made and documented in section 3.3. For organisational reasons the test flight cannot be done directly in a steel plant, however it is performed in one of RHI's factories which provides a harsh industrial environment as well.

3.1.1 Heat transfer model

The prerequisite to specify temperature in the immediate surrounding of a drone during a measurement flight is the specification of the air route. As stated in section 2.6, the drone starts from a base station, flies to several vessels to measure the thickness of the refractory lining and returns to the base station after the measurement has been finished. The route from base station to vessel and back can be chosen more or less freely and therefore only depends on the average temperature in the steel plant. As mentioned earlier, this temperature is much the same than the outside temperature and depends on the plant's location, the weather conditions and the season of the year. In some cases it could be problematic as well, however usually the drone's measuring position near a vessel will be more critical. Principally, the optimum position would be directly in the middle above a vessel. However, heat convection leads to extremely high temperatures in this area which makes such a measurement practically impossible. Another possibility is to measure straight above or slightly outside the vessel's edge. In this case, several measurements have to be done from at least two different positions to get a picture of the complete inner surface. The situation is depicted in figure 3.1.1 exemplary with an EAF.

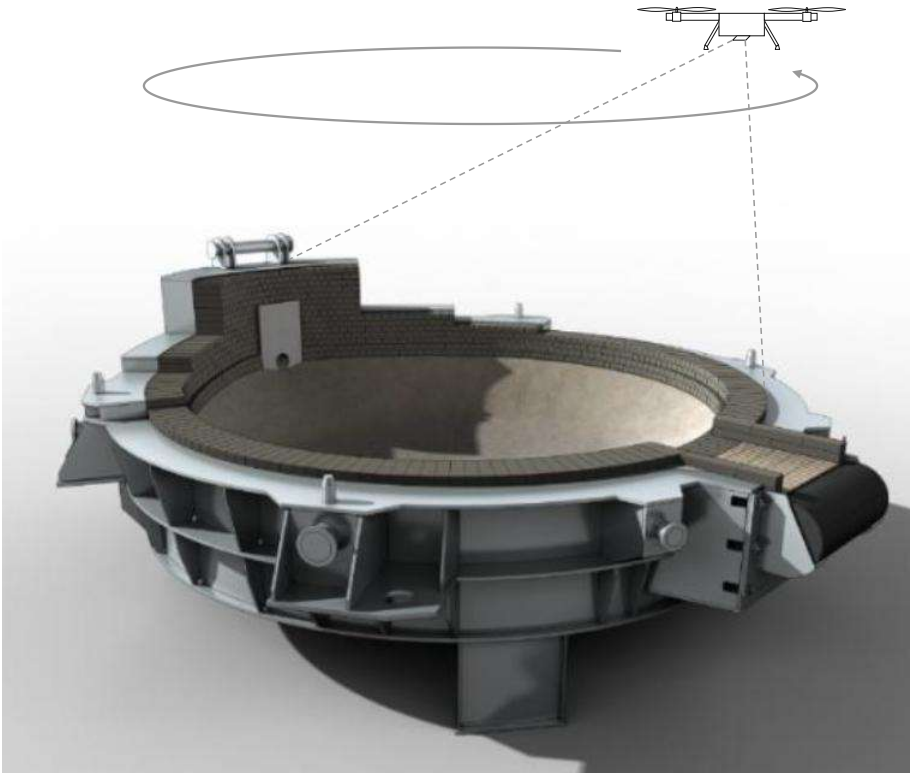

Figure 3.1.1: UAV measuring the surface of an EAF. The drone measures from different positions straight above or slightly outside the vessel's edge. At least two measurements are necessary to gain a full view of the inner surface.

Basics of heat transfer

The basic definition of heat transfer is the transport of energy between solids, liquids and gases due to temperature differences. Heat is always transferred from the place with higher temperature to the place with lower temperature (second principle of thermodynamics). It can be distinguished between three types of heat transfer [28]:

- **Heat conduction.** The transport of energy due to heat conduction is caused by the interaction of neighboured atoms and molecules of a specific material. The inner energy of atoms or molecules with a higher energy level flows to those with a lower energy level. During this process, stochastic microscopic vibrations and movements lead to collisions of the particles. Heat conduction occurs in solids, liquids as well as gases and the resulting heat flow depends on the material's thermal conductivity. As an example, the thermal conductivity of air is 0.0262 W/mK, compared to a well thermally-conducting material like copper with 401 W/mK. As the thermal conductivity is not only low for air, but for gases in general, it is easy to understand that heat conduction plays a subordinated role in those materials.
- **Heat convection.** In liquids and gases, the transport of thermal energy is additionally effected by macroscopic flow of material, which is called convection. It can

be distinguished between natural and forced convection. Forced convection requires an outer impact (e.g., pump, blower) to maintain material flow. Free convection results from temperature-related local density differences which cause buoyancies.

- **Heat radiation.** The third heat transfer mechanism transports energy in the form of electromagnetic waves. They are caused by the inner energy of the material, which is in a local thermodynamic equilibrium. Heat rays transport energy with the velocity of light and have a wavelength of 0.1 µm to 1 mm. The most outraging difference of heat radiation to the other mechanisms is that it does not need any transport medium and therefore also works in vacuum.

Concerning the situation depicted in figure 3.1.1, heat radiation will be a crucial heat transfer mechanism. Assuming that there are no forced air movements in the steel plant, convection is relevant as well in an area directly above the hot vessel. Even if the multicopter is not placed directly above the vessel, it can be supposed that convection still plays a big role at its position (not at least because the case of a windless steel plant is very unlikely). As mentioned before, the influence of heat conduction is often irrelevant in gases which is why it will not be taken into account in the following.

Heat radiation

Every object with a temperature above the absolute zero emits heat radiation [28]. The basis of calculations in the context of heat radiation is in most cases the model of the black body. A black body is a (in reality non-existent) object which absorbs all impinging radiation at its surface. The object itself emits heat radiation which only depends on temperature (for real objects it also depends on further factors like shape and surface). Planck's radiation law describes the spectral distribution of the radiation emitted from a black body:

$$E_{\lambda,b}(\lambda, T) = \frac{2\pi h c_0^2}{\lambda^5 \left(\exp\left(\frac{hc_0}{\lambda k T}\right) - 1\right)}. \tag{3.1.1}$$

In this equation, $h = 6.626 \cdot 10^{-34}\,\mathrm{Js}$ is Planck's constant, $c_0 = 299\,792\,458\,\mathrm{m/s}$ is the speed of light and $k = 1.38 \cdot 10^{-23}\,\mathrm{J/K}$ is the Boltzmann constant. When integrating (3.1.1) over all wavelengths λ, the result is the Stefan-Boltzmann law which describes the totally emitted radiation of a black body:

$$E_b(T) = \int_0^\infty E_{\lambda,b}(\lambda, T)\,\mathrm{d}\lambda = \sigma T^4 \tag{3.1.2}$$

with the Stefan-Boltzmann constant $\sigma = 5.67 \cdot 10^{-8}\,\mathrm{W/(m^2K^4)}$. This simple correlation is only valid for black bodies, which do not exist in reality. When multiplying (3.1.2) with a wavelength- and direction-independent emissivity $\varepsilon(T) \in [0, 1]$, it can be used to calculate the emission of so-called grey bodies:

$$E_g(T) = \varepsilon(T)\,\sigma T^4. \tag{3.1.3}$$

With a known emissivity and the assumption that refractory emits direction- and wavelength-independently like a grey body, the heat radiation of a vessel like the EAF in figure 3.1.1 can be calculated. However, this still doesn't help to figure out the incoming radiation at

the drone's position. One possibility to calculate heat exchange between two objects is the net radiation method ([51], [63]), which is outlined in the following.

Figure 3.1.2 depicts two surfaces A_i and A_j with the temperatures T_i and T_j. $\mathrm{d}\mathcal{A}_i$ and $\mathrm{d}\mathcal{A}_j$ are infinitesimal surface elements with the normal vectors $\vec{n_i}$ and $\vec{n_j}$. The distance between the two elements is defined as s_{ij} with the angles θ_i and θ_j to the normal vectors.

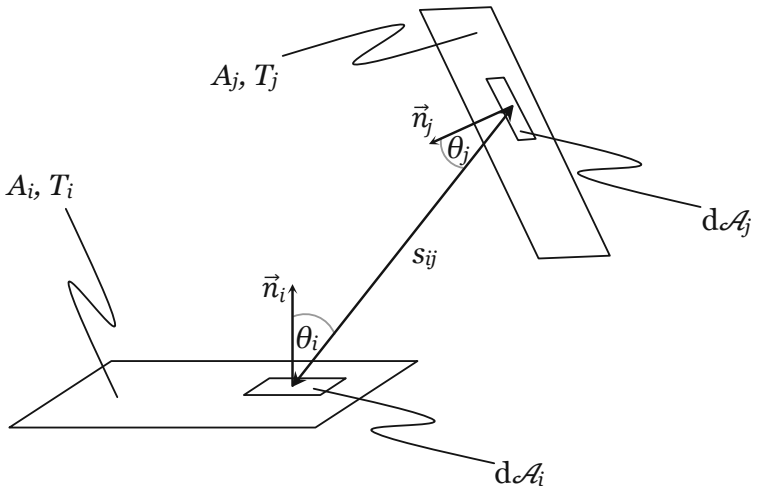

Figure 3.1.2: Surfaces A_i and A_j with temperatures T_i and T_j. The heat exchange between the surfaces is calculated with the net radiation method [51].

Additionally to the emissivity, a wavelength-independent absorptance α, reflectance ρ and transmittance τ can be defined for any arbitrary grey body, whereas

$$\alpha + \rho + \tau = 1. \tag{3.1.4}$$

These three parameters describe the amounts of impinging radiation on a grey body that are either absorbed, reflected or transmitted. Let G_i be the impinging radiation (with the unit $\mathrm{W/m^2}$) on A_i and E_i the total radiation emitted from A_i. Assuming $\alpha = \tau = 0$ and $\rho \neq 0$, E_i can be written under consideration of (3.1.3) as

$$E_i = \varepsilon_i \sigma T_i^4 + \rho_i G_i \tag{3.1.5}$$

Let $V_{ij}E_i$ be the amount of E_i impinging on A_j. $V_{ij} \in [0, 1]$ is a dimensionless value called view factor which still has to be designated. It solely depends on the shape and geometrical arrangement of A_i and A_j. The totally emitted radiation power of the surface element $\mathrm{d}\mathcal{A}_i$ is $\mathrm{d}\mathcal{A}_i E_i$. It follows that the emitted radiation power in in an arbitrary direction defined by s_{ij} is

$$\mathrm{d}\mathcal{A}_i E_i \frac{\cos(\theta_i)}{\pi} \tag{3.1.6}$$

with the normalization factor $\frac{1}{\pi}$. This factor is necessary to ensure that the integral of (3.1.6) over the surface of a hemisphere above $\mathrm{d}\mathcal{A}_i$ results in $\mathrm{d}\mathcal{A}_i E_i$ again, which is a

compelling necessity caused by the assumption of a grey body emitting radiation direction-independently. From the view of $\mathrm{d}\mathcal{A}_i$, the solid angle covered by $\mathrm{d}\mathcal{A}_j$ at the distance s_{ij} is

$$\frac{\cos(\theta_j)\,\mathrm{d}\mathcal{A}_j}{s_{ij}^2}. \tag{3.1.7}$$

The square in the denominator of (3.1.7) results from the fact that the surface of a sphere grows quadratically with its radius. E.g., a surface element of constant size covering 1/10 of the surface of a sphere with radius R will only cover 1/40 of the surface of a sphere with radius $2R$ and only 1/90 of a sphere's surface with radius $3R$. It can be seen that the covered surface is proportional to $\frac{1}{R^2}$. Combining (3.1.6) and (3.1.7), the impinging radiation power at $\mathrm{d}\mathcal{A}_j$ caused by the totally emitted power $\mathrm{d}\mathcal{A}_i E_i$ of $\mathrm{d}\mathcal{A}_i$ is

$$\mathrm{d}\mathcal{A}_i E_i \frac{\cos(\theta_i)}{\pi} \frac{\cos(\theta_j)\,\mathrm{d}\mathcal{A}_j}{s_{ij}^2}. \tag{3.1.8}$$

The result of an integral of (3.1.8) over the surfaces A_i and A_j delivers the entire radiation power transmitted from A_i to A_j, which is $V_{ij} A_i E_i$. It follows that the view factor can be calculated with

$$V_{ij} = \frac{1}{A_i} \int_{\mathcal{A}_i} \int_{\mathcal{A}_j} \frac{\cos(\theta_i)\cos(\theta_j)}{\pi s_{ij}^2} \mathrm{d}\mathcal{A}_j \mathrm{d}\mathcal{A}_i. \tag{3.1.9}$$

Assuming that A_i is the surface of an EAF and A_j is the surface of a UAV, (3.1.9) can be used to calculate the heat radiation that a UAV is exposed to during a surface measurement. To simplify the calculation, a few assumptions are made:

- The radiating surface of the EAF has the shape of a circle. Indeed, EAFs are not circular but rather have an egg-shaped cross section.
- The drone's surface is parallel to the EAF. This assumption is largely correct as the drone doesn't tilt when it is not moving. This leads to the simplification $\theta_i = \theta_j$ (also see figure 3.1.3).

To solve the integral, universal expressions for the variables $\theta_i = \theta_j = \theta$ and s_{ij} have to be found. For this issue it is helpful to look at figure 3.1.3. The sketch shows a circular surface A_i which represents the EAF and a rectangular surface A_j representing the UAV. $\overrightarrow{n_i}$ is the normal vector on A_i and $\overrightarrow{n_j}$ is the normal vector on A_j. A_i is in the Cartesian coordinate system S with the coordinates (x, y, z) and A_j is in the Cartesian coordinate system S' with the coordinates (x', y', z'). The origins of both coordinate systems are in the center of the surfaces, and the origin of S' is located at $(W, 0, h)$ in S. This position represents the position of the UAV. Positioning the center of the drone at $y = 0$ is not necessary, however it simplifies the calculation and can be done without loss of generality. P_i is an arbitrary position in A_i with the coordinates (x_i, y_i, z_i) and P_j is an arbitrary position in A_j with the coordinates (x'_j, y'_j, z'_j). To evaluate the integral in (3.1.9), the angle $\theta_i = \theta_j = \theta$ and the distance s_{ij} have to be determined and S' has to be transformed into S. This transformation can be done with the following relations:

$$\begin{aligned} x &= x' + W \\ y &= y' \\ z &= z' + h. \end{aligned} \tag{3.1.10}$$

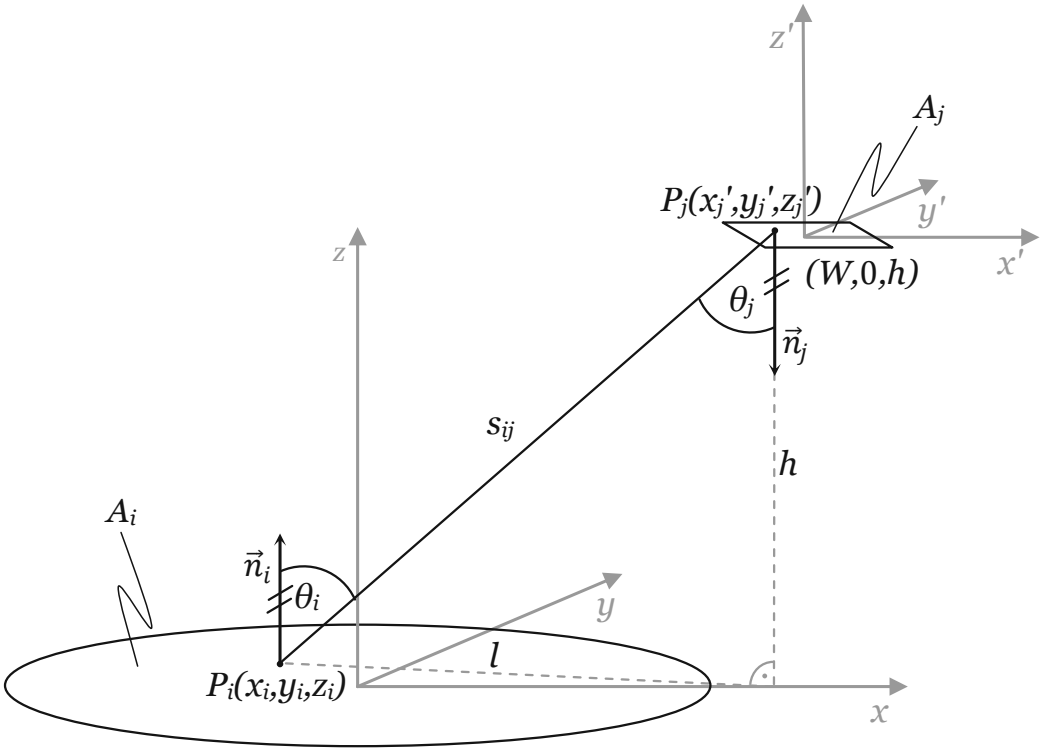

Figure 3.1.3: Parameters of the heat radiation model. The drone's position is represented by $(W, 0, h)$, the drone's surface is assumed to be rectangular. $\overrightarrow{n_i}$ and $\overrightarrow{n_j}$ are parallel and as a result $\theta_i = \theta_j$.

According to the Pythagorean theorem and with (3.1.10), s_{ij}^2 can be determined as

$$\begin{aligned} s_{ij}^2 &= (x_j - x_i)^2 + (y_j - y_i)^2 + (z_j - z_i)^2 = \\ &= \left(x_j' + W - x_i\right)^2 + \left(y_j' - y_i\right)^2 + \left(z_j' + h - z_i\right)^2 = \\ &= \left(x_j' + W - x_i\right)^2 + \left(y_j' - y_i\right)^2 + h^2. \end{aligned} \tag{3.1.11}$$

The step between the second and third row of (3.1.11) can be done, because A_i and A_j are assumed to be flat and therefore z_i and z_j' are always zero. Due to the circular shape of A_i it is obvious to use cylindrical coordinates. The transformation rules are as follows:

$$\begin{aligned} x &= r\cos(\varphi) \\ y &= r\sin(\varphi) \\ z &= z. \end{aligned} \tag{3.1.12}$$

With these relations, s_{ij} results in

$$s_{ij}(x'_j, y'_j, r_i, \varphi_i) = \sqrt{\left(x'_j + W - r_i \cos(\varphi_i)\right)^2 + \left(y'_j - r_i \sin(\varphi_i)\right)^2 + h^2}. \tag{3.1.13}$$

As the distances between P_i and P_j in vertical and horizontal direction are known now (h and l in figure 3.1.3), the angle θ can be determined easily with

$$\begin{aligned}\theta(x'_j, y'_j, r_i, \varphi_i) &= \frac{\pi}{2} - \arctan\left(\frac{h}{l}\right) = \\ &= \frac{\pi}{2} - \arctan\left(\frac{h}{\sqrt{\left(x'_j + W - r_i \cos(\varphi_i)\right)^2 + \left(y'_j - r_i \sin(\varphi_i)\right)^2}}\right)\end{aligned} \tag{3.1.14}$$

With (3.1.13), (3.1.14), R as the EAF's radius and $d1$ and $d2$ as the multicopter's dimensions, (3.1.9) results in

$$V_{ij} = \frac{1}{R^2\pi} \int_0^{2\pi} \int_0^R \int_{-\frac{d1}{2}}^{\frac{d1}{2}} \int_{-\frac{d2}{2}}^{\frac{d2}{2}} r_i \frac{\cos^2\left(\theta(x'_j, y'_j, r_i, \varphi_i)\right)}{\pi s_{ij}^2(x'_j, y'_j, r_i, \varphi_i)} \mathrm{d}x'_j \mathrm{d}y'_j \mathrm{d}r_i \mathrm{d}\varphi_i. \tag{3.1.15}$$

To estimate the radiating power at the drone's position with (3.1.15), it is necessary to know the total radiation emitted from A_i. A generalized expression for the calculation has already been given in (3.1.5). However, as the hot furnaces and vessels are the only significant sources of radiation in steel plants and they are usually placed at distances where they do not influence each other, the impinging radiation G_i can be neglected and the total emission is written as

$$E_i = \varepsilon_i \sigma T_i^4. \tag{3.1.16}$$

Referring to [8], magnesia refractory has an emissivity of $\varepsilon = 0.38$ at a temperature of 1000 - 1300 °C. As steel with an amount of 2 % carbon has a melting point of 1400 °C, a temperature of 1300 °C for the refractory immediately after tapping is realistic. As a result, the area-related power density of the emission is 61.537 kW/m^2.

At first it is interesting to see the amount of radiation at different heights h and different distances W to the EAF's center. It is assumed that the EAF's radius R is 3 m and the drone's surface A_i is $0.5 \times 0.5\,\mathrm{m}^2$. With these input values, (3.1.15) is numerically calculated with MATLAB. The resulting graphs are shown in figure 3.1.4. The value of $W = 3.2$ m seems to be strange, however it is chosen for aesthetic reasons as the resulting function approaches to a step at $h = 0$ m for values of $W \leq 3$ m.

As the view factor is directly proportional to the power density and in further consequence to the temperature at the drone, the following general properties can be derived from the graphs: as it may be expected, the overall temperature declines with growing distance W. Furthermore, the impinging radiation is zero at $h = 0$ m. Usually there will be some radiation directly at the vessel's edge, however the developed model assumes the heat source to be a planar surface and therefore doesn't take into account any lateral radiation at $h \leq 0$ m. The most interesting issue is that the temperature has a significant peak somewhere in the first 5 m above the vessel and quickly declines afterwards. This property is very evident too when considering that the view factor is only dependent on

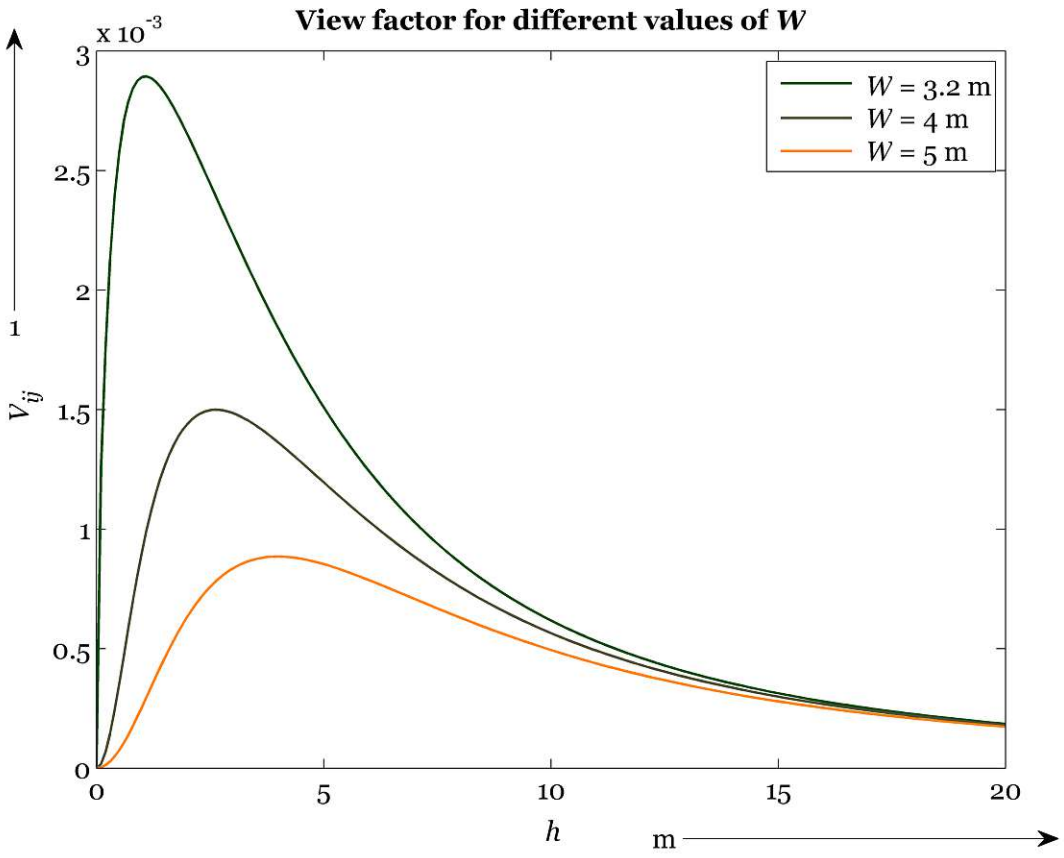

Figure 3.1.4: V_{ij} as a function of the drone's height h for three different distances W to the center of the vessel. For values $W \leq 3\,\mathrm{m}$, the resulting function has a step at $h = 0\,\mathrm{m}$.

the geometrical arrangement (under the assumption of direction-independent emission). For small values of h, the drone "sees" the vessel in a rather flat angle and therefore its surface seems to be small. The higher the drone's position is, the bigger the surface becomes until the UAV exceeds a specific height and the surface appears to shrink again due to the growing distance.

When assuming that the UAV is positioned above the vessel's edge ($W = 3.2\,\mathrm{m}$) at a height of 5 m, the view factor is 0.0016. With $V_{ij}E_i$ as the amount of E_i impinging at A_j and (3.1.16), an area-related power density of $98.46\,\mathrm{W/m^2}$ reaches the drone. With the assumed surface of $0.25\,\mathrm{m^2}$, the resulting power is 24.6 W. It does not make sense to calculate a priori the temperature increase of the drone caused by this value. The energy needed to warm up a certain material by a certain temperature depends on the material's specific heat capacity. However, a drone consists of many different materials and its specific heat capacity could only be determined experimentally and is furthermore different for each drone model. Thus, an alternative consideration is made to figure out whether the calculated power density could be harmful or not. The average extraterrestrial power density of the sun's radiation is $1367\,\mathrm{W/m^2}$ [98]. Extraterrestrial means in this context that the value doesn't take into account attenuation of the radiation in the atmosphere.

The amount of attenuation depends on weather conditions as well as on the season of the year, however it can be said that the power density of radiation on the ground on a summer day with clear sky in Central Europe is approximately 1000 W/m^2, which is about ten times higher than the calculated power density above an EAF. As ordinary commercial drones do not have any restrictions that they can not be used outdoors in summer, it can be assumed that a drone will be resistant to the heat radiation in the regarded position.

It may seem that the situation must be fundamentally different directly above the vessel. For this purpose, V_{ij} is calculated as a function of W for three different heights h (see figure 3.1.5). It can be seen that the resulting function has a peak at the center of the vessel

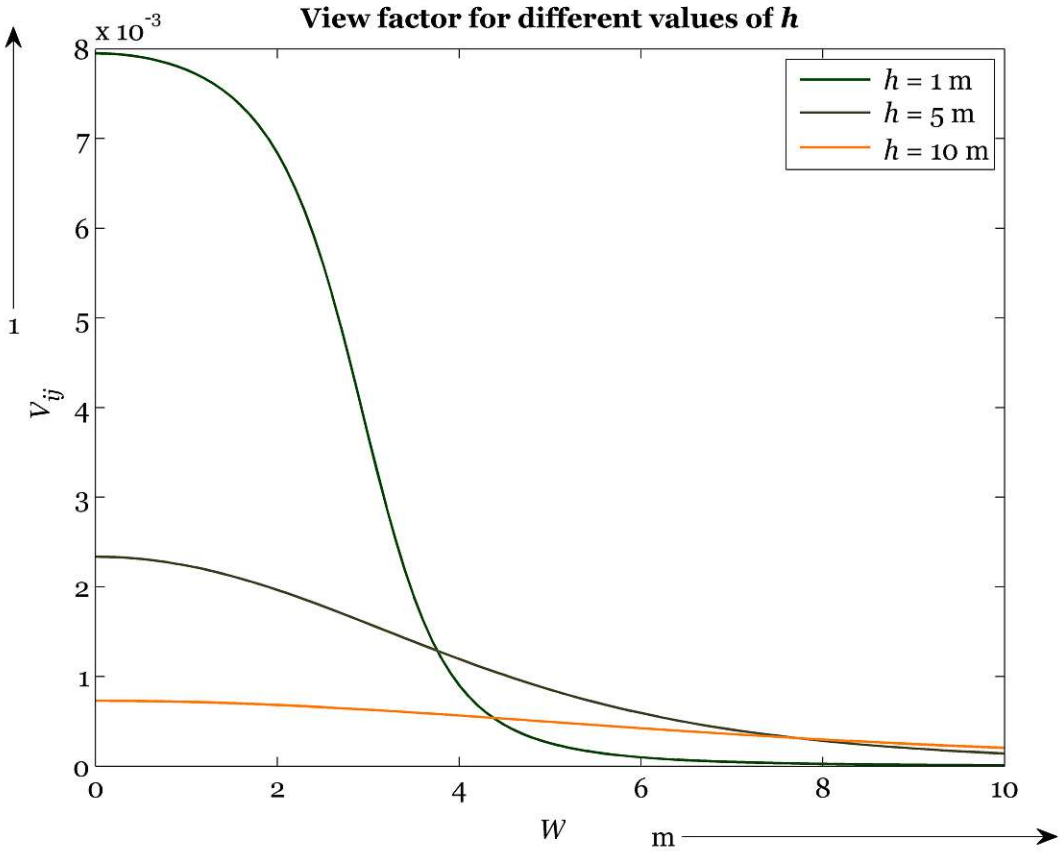

Figure 3.1.5: V_{ij} as a function of W for three different heights h. The vessel has a radius of 3 m and its center is at $W = 0$ m.

($W = 0$ m), however it flattens with increasing height. For $h = 1$ m, V_{ij} decreases quickly around $W = 3$ m, which is the vessel's radius. The absolute values are higher than in figure 3.1.4. E.g., at a height of 5 m, the value of V_{ij} is 0.0023 in the vessel's center. With the same calculation as before, the power density results in 141.54 W/m^2. At a height of 1 m, the view factor is 0.008 in the middle of the vessel and the power density results in 492 W/m^2. Considering the radiation of the sun again, these values seem to be much too low. However, it should not be forgotten that the net radiation method does not take into account any of the two remaining heat transfer mechanisms. Thus, the estimation in this

section can only be used for values of $W \geq 3\,\mathrm{m}$. To estimate temperature directly above a hot vessel it is necessary to take into account heat convection as well.

Heat convection

To determine temperature directly above a ladle, EAF or BOF, convective heat transfer has to be considered as an additional mechanism. In general, it is very sophisticated to describe convective heat transfer analytically as it requires mathematical methods used in continuum mechanics, e.g., energy and momentum balance as well as partial differential equations like the continuity equation. For an exact calculation, constitutive equations would be needed as well to incorporate friction effects in the fluid or gas. However, for the use case in this thesis such calculations appear to be overstated. Thus, this section concentrates on mathematical descriptions that are common in thermodynamics and are based on dimensionless quantities and partly empirical correlations.

To apply these methods, the overall conditions have to be defined first.

- As in section 3.1.1, it is assumed that the heat source is a planar surface with circular shape.
- There is no forced convection around this surface, i.e., the steel plant is windless. With this assumption, only natural convection has to be taken into account which means that the motion of the ambient air is only caused by buoyancies due to temperature differences.
- In reality, refractory cools down slowly after tapping, however here it is assumed that its temperature remains constant.
- The ambient air masses are big enough that they do not warm up significantly over the time period considered.

With these assumptions, the vessel can be modelled as a constantly heated plate which is cooled by the ambient air. Convective heat transfer in such situations can be estimated with Newton's law of cooling [51]:

$$\frac{\mathrm{d}Q}{\mathrm{d}t} = \bar{h} A \Delta T. \tag{3.1.17}$$

Q is the thermal energy, $\bar{h}$ is the so-called heat transfer coefficient which still has to be calculated and is assumed to be temperature independent in this equation, A is the plate's cross sectional area and ΔT is the temperature difference between plate and ambient air. In a general case, $\bar{h}$ would not be temperature independent, however the last two assumptions stated above indicate a steady state.

Vividly speaking, Newton's law of cooling says that the loss of thermal energy of an object is proportional to the temperature difference between the object and its surrounding. This is usually true for heat conducting mechanisms, however for heat convection it can only be seen as an approximation [28].

To determine $\bar{h}$, the Nußelt number, which is a dimensionless quantity, has to be considered. The Nußelt number indicates for which amount heat transfer increases because

of heat convection, compared to heat transfer that is only caused by heat conduction:

$$Nu = \frac{\bar{h}L}{k}. \tag{3.1.18}$$

k is the heat conductivity of the gas or fluid in W/(mK) and L is the characteristic length. Its definition depends on the geometrical characteristics of the object considered. For an arrangement depicted in figure 3.1.6, namely a cooled horizontal plate, [28] defines L as the ratio of the plate's surface area to its diameter, i.e.,

$$L = \frac{R^2\pi}{2\pi R} = \frac{R}{2}. \tag{3.1.19}$$

Additionally, [70] and [28] give a very useful correlation between the Nußelt number and

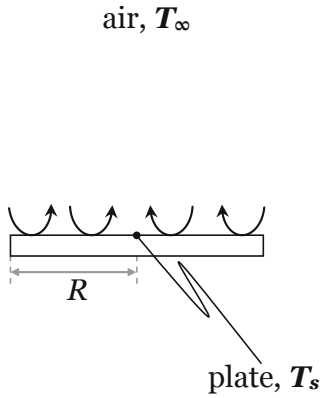

Figure 3.1.6: Sketch for determination of the heat transfer coefficient $\bar{h}$. The plate represents a hot vessel with radius R and temperature T_s, the ambient air temperature is T_∞. The arrows symbolize heat convection. Adapted from [28].

the Rayleigh number Ra for the same arrangement:

$$\begin{aligned} Nu_L &= 0.54 Ra_L^{\frac{1}{4}} \qquad 10^4 \leq Ra_L \leq 10^7 \\ Nu_L &= 0.15 Ra_L^{\frac{1}{3}} \qquad 10^7 \leq Ra_L \leq 10^{11}. \end{aligned} \tag{3.1.20}$$

The Rayleigh number describes the character of heat transfer of a gas or fluid. For the considered values of Ra in (3.1.20), heat transfer is primarily convective and laminar for values of $Ra \leq 10^7$ and convective and turbulent for higher values. When Ra is below a critical value (in this case 10^4), the influence of heat convection is negligible and heat conduction becomes the dominating mechanism. The Rayleigh number depends on a number of material parameters that can be found in literature:

$$Ra = \frac{g\beta(T_s - T_\infty)L^3}{\nu\alpha} \tag{3.1.21}$$

with the earth acceleration g in $\mathrm{m/s^2}$, the thermal expansion coefficient β in $1/\mathrm{K}$, the two temperatures T_s and T_∞ as depicted in figure 3.1.6, the characteristic length L, the kinematic viscosity ν in $\mathrm{m^2/s}$ and the thermal diffusivity α also in $\mathrm{m^2/s}$. The thermal expansion coefficient, the kinematic viscosity and the thermal diffusivity are temperature dependant, which is in further consequence the reason for the temperature dependence of $\bar{h}$. For the steady state regarded here, a specific temperature is needed to look the values up in literature. For this purpose, usually the so-called film temperature T_f is used [28], which is defined as

$$T_f = \frac{T_s + T_\infty}{2}. \tag{3.1.22}$$

Similarly to section 3.1.1 it is assumed that the vessel has a radius of $R = 3\,\mathrm{m}$ and a surface temperature of $T_s = 1300\,^\circ\mathrm{C}$. Additionally, the ambient temperature T_∞ shall be $30\,^\circ\mathrm{C}$. With (3.1.22), the film temperature results in $T_f = 665\,^\circ\mathrm{C} = 938.15\,K$. The values for the other parameters of air at atmospheric pressure at this temperature are looked up in [28]. All numbers needed for the calculation are listed in (3.1.23).

$$\begin{aligned} k &= 64.3 \cdot 10^{-3}\,\mathrm{W/(mK)} \\ \nu &= 112.2 \cdot 10^{-6}\,\mathrm{m^2/s} \\ \alpha &= 155 \cdot 10^{-6}\,\mathrm{m^2/s} \\ \beta &= \frac{1}{T_f} = 1.07 \cdot 10^{-3}\,1/\mathrm{K} \\ g &= 9.81\,\mathrm{m/s^2} \\ L &= 1.5\,\mathrm{m} \end{aligned} \tag{3.1.23}$$

Referring to (3.1.21), the Rayleigh number results in

$$Ra = 2.587 \cdot 10^9. \tag{3.1.24}$$

According to (3.1.20) this means that turbulent convection dominates and the Nußelt number results in

$$Nu = 205.92. \tag{3.1.25}$$

With (3.1.18), $\bar{h}$ can be calculated to

$$\bar{h} = Nu\frac{k}{L} = 8.827\,\mathrm{W/(m^2K)}. \tag{3.1.26}$$

According to Newton's law of cooling (3.1.17), the thermal power emitted from the surface of the vessel results in

$$\frac{\mathrm{d}Q}{\mathrm{d}t} = 316.96\,\mathrm{kW}. \tag{3.1.27}$$

With $R = 3\,\mathrm{m}$, the vessel's surface is $28.27\,\mathrm{m^2}$ which leads to an area-related power density of $11.21\,\mathrm{kW/m^2}$. Making the same considerations like in section 3.1.1, this value is about 11 times higher than the average area-related radiated power density of the sun on earth. Thus, it is very unlikely that a common UAV without any special cooling or heat protection could fly directly above an EAF or a similar vessel.

3.1.2 Temperature resilience

In the previous section, an estimation of temperature in the immediate environment of a vessel in a steel plant was performed with a mathematical model. Based on this model and some empirical considerations, it could be figured out that it is principally possible to position a drone as shown in figure 3.1.1 without destroying it immediately. Nevertheless, to clarify the understanding in this field it is necessary to specify the UAV's temperature resistance more closely.

A multicopter is a system consisting of many different parts out of different materials with different temperature resistance. Hence, it makes sense to look at the different components separately.

Frame

This component usually consists of a light-weight and robust composite material like carbon-fibre reinforced plastic. It is difficult to make a clear statement about the material's temperature resistance as it strongly depends on the exact composition. However, plastics that are temperature resistant up to a few hundred degrees Celsius exist, like for example polytetrafluoroethylene (better known as Teflon). In principal, the frame could also be constructed out of a light metal like aluminium (melting point $\sim 660\,^{\circ}\mathrm{C}$) or titanium (melting point $\sim 1668\,^{\circ}\mathrm{C}$). All in all, the frame will not be a critical component concerning temperature resistance of the multicopter.

Propellers

The same is more or less true for the propellers. They are usually made out of plastics too but could also be made out of metal if necessary. Additionally, propellers are a wearing part and have to be exchanged from time to time anyway. This means that they do not have to resist extreme temperatures for the drone's whole lifetime.

Motors

Usually, permanent magnet synchronous motors (also called brushless motors) with Neodymium Iron Boron (NeFeB) magnets are used for UAVs. The main problem is that the permanent magnets demagnetize with rising temperature, i.e., the intrinsic coercivity and the remanence decrease, which leads to a worse efficiency of the motor. However, as long as a critical temperature is not exceeded, the effect is reversible and the flux density returns to the original value once the temperature is reduced. Typically, brushless motors are designed for operating temperatures up to $150\,^{\circ}\mathrm{C}$ [87].

Hardware

In the following, the controller hardware as well as the sensor system are summarized in the term "hardware". At this time, it is not possible to make a clear statement about the temperature resistance as it strongly depends on the special hardware configuration. The temperature range of processors and microcontrollers is different for every model. As an example, an industrial microcontroller like the Infineon XMC4700/XMC4800 can be operated between $-40\,^{\circ}\mathrm{C}$ and $+125\,^{\circ}\mathrm{C}$ [5] whereas the operating temperature of a small-form-factor personal computer like the Intel NUC lies between $0\,^{\circ}\mathrm{C}$ and $+50\,^{\circ}\mathrm{C}$ [6]. If a

hardware setup contains components like electrolytic capacitors, those will dry out faster at high temperatures and the electrical circuit will not work correctly any more.

As there is a high demand of using computers and electrical components in extreme temperature areas (e.g., automotive industry, aerospace), several companies and institutions work on the development of temperature resistant hardware. Presently, the world-leader in this matter is the NASA Glenn Research Center. The research center develops electronics and sensors that withstand long-term operation in harsh environment with temperatures up to 500 °C [50]. With respect to section 3.1.1, the drone in the steel plant will not be exposed to temperatures of this magnitude. It is most likely that usual hardware for industrial applications can be used. Nevertheless it may be possible that thermal shielding or cooling is necessary to stay within the hardware's recommended temperature range. As already mentioned, temperature in steel plants is not constantly very high but changes a lot. This means that at least for some time during a flight cool air is available in the near environment of the UAV, which would even enable self-cooling. Another possibility would be to install a temperature sensor on the drone and continuously measure its own temperature. If the temperature became too high, the UAV could return to the base station automatically.

Battery

The battery is the most temperature critical component as it is both sensitive to low as well as to high temperatures. To understand the reasons for this behaviour better, the functionality of rechargeable (secondary) batteries is discussed briefly, before going deeper into typical properties of different battery types.

Rechargeable batteries store energy electro-chemically. To be more specific, the underlying principle always is a redox reaction. Battery types mainly differ in the materials used for the electrodes and for the electrolyte. These materials are also responsible for the battery's nominal cell voltage and other properties like energy density and temperature dependence. Not at least due to their high weight-related energy density, lithium-ion batteries currently are the most widely used battery type. They are employed in most battery-operated electrical appliances that are used in everyday life, like mobile phones, notebooks or electrical machine tools. The importance of lithium-ion batteries also grows in electric mobility, e.g., as energy storage for hybrid cars, electric cars and pedelecs (bicycle with electrically supported drive). Furthermore, there are areas of application in energy supply, where lithium-ion batteries are used as stationary mass storage with capacities of up to 5 MWh [61]. Due to their popularity, lithium-ion batteries are taken as an example to explain the functional principle of secondary batteries here.

The general structure of a single lithium-ion battery cell is depicted in figure 3.1.7. The positive electrode consists of lithium metal oxide, whereas various metals such as manganese, nickel or cobalt can be used. The negative electrode is made of graphite or amorphous carbon compounds. The electrodes are immersed into a non-aqueous electrolyte. It has to be non-aqueous because lithium is highly reactive with water. The electrolyte furthermore contains a lithium-conducting salt to facilitate the transport of lithium-ions. As the electrolyte is in general also electrically conducting, the cell is divided into two parts by a separator to avoid a short circuit between cathode and anode. This is an electrically isolating porous membrane which is permeable for lithium ions [61].

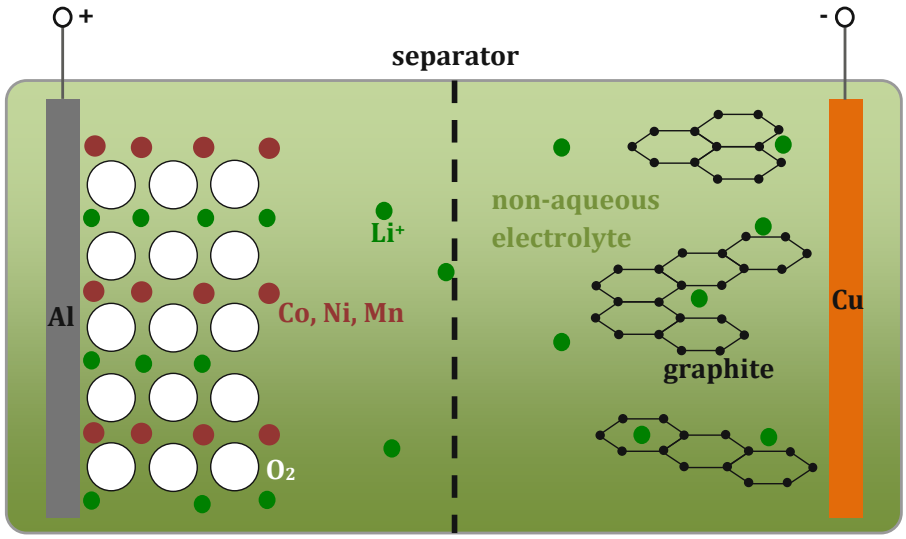

Figure 3.1.7: Structure of a lithium-ion battery cell with a lithium metal oxide anode and a graphite cathode. Adapted from [61].

During the process of charging, an external voltage source transports electrons from the positive electrode to the negative one. In the lithium metal oxide electrode, lithium has the oxidation number +1, oxygen -2 and the metal +3. As a result, the electrode is uncharged (oxygen occurs as diatomic molecule). However, when electrons are removed due to the external voltage during the charging process, the metal is further oxidized to the oxidation state +4. This means that the metal oxide layer would be charged positively. In order to prevent this nonequilibrium, positive lithium ions move through the separator to the negative electrode where they embed into the layered structure of the graphite and recombine with an electron. As soon as all lithium ions have left the positive electrode, the battery is charged. When now a load is connected to the charged battery cell, electrons flow from the graphite electrode through the load to the metal oxide electrode and the reversal process occurs. The lithium atoms in the graphite structure are ionized and go through the separator to the metal oxide electrode where the metal is reduced back to oxidation stage +3 and the ions can be built into the atomic lattice again.

With cobalt in the lithium metal oxide electrode, the chemical equations can be written as follows (the equations don't qualitatively change with another metal) [90].

$$\begin{aligned} &\mathrm{Li}_x^{+I}\mathrm{Co}^{+III}\mathrm{O}_2 \leftrightarrow x\mathrm{Li}^+ + x\mathrm{e}^- + \mathrm{Co}^{+IV}\mathrm{O}_2 && \text{(positive electrode)} \\ &x\mathrm{Li}^+ + x\mathrm{e}^- + \mathrm{C}_6 \leftrightarrow \mathrm{Li}_x^{+I} + \mathrm{C}_6^{-I} && \text{(negative electrode)} \end{aligned} \tag{3.1.28}$$

It should be mentioned here that this depiction is simplified. In reality, there occur much more chemical reactions than those described in (3.1.28). A detailed evaluation of these so-called side reactions is not aim of this thesis, however a lot of additional information in this context can be found in [90].

It is very difficult to find out all the reasons for temperature-affected impacts on lithium

ion batteries. For this issue, all chemical reactions inside a battery would have to be understood completely as well as the rule of temperature in these reactions. Although it is well known how secondary batteries work, not every chemical process is apprehended in detail [90] and therefore some things just have to be taken for granted. Nevertheless, the basic and most influential temperature effects in batteries can be understood when the battery's general structure is known.

Cold temperatures have a negative impact on the ion conductivity of the electrolyte, which means that the battery's internal resistance grows. As a result, less ions can be transported between the electrodes within a specific time. This means that on the one hand the charging process is slower and on the other hand it is more difficult to get energy out of a charged battery. Additionally, low temperatures accelerate the cell's ageing because of the so-called lithium-plating: during charging, pure lithium is deposited on the anode which reduces the cell's capacity. Lithium-plating may also lead to a total destruction of the cell. The cell is destroyed when the deposited lithium forms dendrites which become as long as the distance between anode and cathode. In this case an inner short circuit occurs. A very similar mechanism emerges in lead-acid batteries (with the only difference that the deposited material is lead sulphate). However, as the effect only occurs during charging, it can be avoided by simply not charging the battery at low temperatures.

Another important ageing mechanism which occurs mainly due to high temperatures is cell oxidation. The electrodes oxidise and can absorb less ions which reduces the cell's capacity by the time. Referring to [61], an increase in the operating temperature of 10 K outside the ideal temperature range of 20 °C - 40 °C halves the battery's lifetime, i.e., the time when its maximum capacity is less than 80 % of the original value. Permanent operating temperatures that are significantly higher than the maximum recommended temperature lead to thermal decomposition of the electrolyte. The result is an inflammation of the cell which may lead to an explosion of the battery as a further consequence. The only possibility to avoid such an incident is to cool the battery if necessary, so that the maximum permitted temperature is not exceeded under any environmental condition.

Basically, what was elucidated here for lithium-ion batteries can be transferred to all other established battery types as well, because the underlying processes, especially those causing thermal sensitivity, are very similar for all secondary batteries. More significant differences are the nominal cell voltage, energy density, number of charge cycles (lifetime), self-discharge and cost. Table 3.1.1 gives a basic overview of these parameters for the most common battery types.

The number of charge cycles in table 3.1.1 can be seen as an equivalent for the lifetime, as it is defined as the time until the battery's capacity has decreased below 80 % of its original value.

Lithium ion batteries provide the highest weight-related energy density. At the same time, they have a satisfying number of charge cycles and an average self discharge. Commercially available UAVs usually have a lithium-polymer battery. This battery type is a further development of a lithium ion battery. The difference is the electrolyte, which is not a liquid but a jelly-like or solid polymer-based material. The maximum energy density currently is not as high as that of common lithium ion batteries, however lithium-polymer battery cells can be built more compact, i.e., they are slimmer.

Keeping in mind the influence on the feasibility of the use of an autonomous drone in a steel plant, an ambient temperature of more than 60 °C does not only harm the battery's performance but also raises safety concerns. The inflammation of the electrolyte due to

	NiCd nickel-cadmium	NiMH nickel-metal hydride	Pb-PbO_2 lead-acid	lithium ion	lithium polymer
cell voltage	1.25 V	1.25 V	2 V	3.6 V	3.6 V
energy density	45 - 80 Wh/kg	60 - 120 Wh/kg	30 - 50 Wh/kg	110 - 160 Wh/kg	100 - 130 Wh/kg
charge cycles 80 % capacity	1500	300 - 500	200 - 300	500 - 1000	300 - 500
self discharge per month	20 %	30 %	5 %	10 %	10 %
operating temperature	−40 °C - +60 °C	−20 °C - +60 °C	−20 °C - +60 °C	−20 °C - +60 °C	0 °C - +60 °C
cost per charge cycle	0.04 €	0.12 €	0.10 €	0.14 €	0.29 €

Table 3.1.1: Important properties of most common batteries [27]. Lithium batteries provide the highest weight-related energy density, however they are the most expensive battery type.

excessive temperature and in further consequence an explosion of the accumulator would inevitably cause a crash of the drone. It must be possible to exclude the occurrence of such a situation in advance, which requires a good knowledge of the temperature distribution in the steel plant and, if necessary, a good thermal management of the battery.

3.2 Aerodynamic aspects

In general, a very close evaluation of aerodynamic effects is inevitable when designing and controlling a multicopter. Possible effects causing instability of a drone are rotor blade flapping, effects of drag or velocity-induced thrust [92]. The intensities and impacts of these effects depend on many factors like the drone's shape, weight and dimensions. Since it is not aim of this thesis to develop a controller for a multicopter, this section is not going to concentrate on this kind of aerodynamic aspects. Instead, it is about estimating the resilience of drones to wind.

Wind is relevant for nearly any drone application, which is why there is a lot of research done on this topic. In [37], the behaviour of a quadrocopter in a wind field is compared to its behaviour in windless areas. To be more specific, the position responses of the drone are compared and conclusions on the controller's performance are drawn. The performance is quite weak as the controller needs 20 seconds to stabilize the drone's position at a wind speed of 3 m/s. Other researchers could reach way better results, as for example [79] with approximately 15 seconds to stabilize the position at a wind speed of 10 m/s.

Furthermore, there have been done various experiments with drones in wind channels to determine special properties like drag or lift coefficient. These values are needed to calculate the effective force on the UAV caused by wind. One interesting outcome in [85] is that a quadrocopter does not behave equally for different horizontal wind directions. In other words, it is insufficient to assume the UAV as flat cylinder. A very detailed

evaluation of the aerodynamic behaviour in a wind channel is given in [80]. In this work, five commercially available multicopters were tested. Experiments were done with full airframes (i.e., the whole system including rotors), bare airframes (without rotors) and single rotors. The influence of wind was evaluated for different pitch-angles, whereas the pitch-angle is the angle of the drone to a horizontal line when the drone is accelerating (i.e., leaning forwards or backwards). The experiments showed that wind in horizontal direction strongly influences the copter's drag, which is obvious. However, it also influences its lift, although this effect is way smaller.

The papers mentioned above only concentrate on the influence of side wind, since the main areas of application of UAVs are outdoors, where side wind plays a major role. Although steel plants are not completely closed, no significantly strong side winds appear inside and the environment still has indoor characteristics. However, the problem may be that there is extremely strong upwind. The strongest upwind in combination with strong steam generation appears immediately after a heat in an EAF, i.e., at the time when the EAF's lid is opened. A surface measurement as described in section 3.1 (also see figure 3.1.1) would have to be done immediately after a heat as it is uneconomical to wait for a certain time and let the vessel cool down. This means that the UAV is exposed to this occurring upwind. The goal of this section is to make a rough estimation of the exerted force of upwind on the multicopter.

For the calculation, the defining equation for wind resistance

$$F_w = \zeta_w \frac{\rho}{2} v^2 A \tag{3.2.1}$$

is used [88]. F_w is the force acting on a surface A, caused by a fluid or gas with density ρ and velocity v, which impinges on the surface. The drag coefficient ζ_w is a dimensionless number taking into account the shape of the surface and the properties of the flow. It usually depends on the Reynolds number, a dimensionless quantity describing the relation of a fluid's inertial to viscosity force. Values for ζ_w have to be determined experimentally in a wind channel and can be found in literature. The idea is to estimate the force on a drone by dividing a drone's body into several parts with surfaces of which ζ_w is known and adding the forces on the single parts. As mentioned before, this method is quite inaccurate, however it should be sufficient for an estimation in terms of magnitude.

When neglecting the UAV's rotors, its frame can be approximately described with a plate and some cylinders (figure 3.2.1).

Depending if it is a quad-, hexa- or octocopter, the drone will have 4, 6 or 8 arms to carry the rotors. The arms are assumed to be cylindrical. Furthermore, the frame consists of a plate-shaped body.

Since ζ_w depends on the Reynolds number Re, this quantity has to be determined first. It can be calculated with

$$Re = \frac{vd}{\nu} \tag{3.2.2}$$

with the velocity v of the fluid, the characteristic length d and the kinematic viscosity ν which has already been mentioned in section 3.1.1. Referring to [28], ν is $15.89 \cdot 10^{-6}\,\mathrm{m^2/s}$ for air at a temperature of 300 K. It was shown in section 3.1.2 that the optimum operation temperature of a UAV is room temperature, so the choice of 300 K as a basic temperature

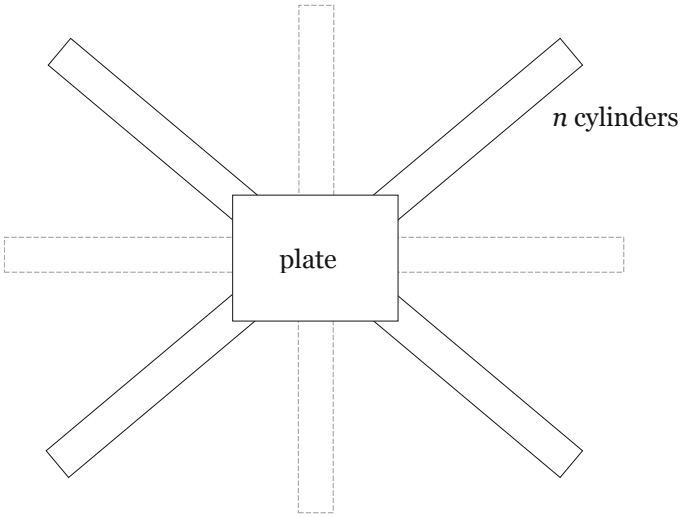

Figure 3.2.1: Drone model to calculate wind resistance. The multicopter approximately consists of a plate-shaped body and n cylindrical arms to mount the rotors, whereas $n = 4, 6, 8$ for a quad-, hexa- or octocopter.

of the calculation is legitimate. The characteristic length d of a cylindrical object simply is its diameter, which is assumed to be 3 cm. The length of a single cylinder is assumed to be 30 cm. Re is calculated with (3.2.2) for 7 different values of v and the corresponding $\zeta_{w,arm}$ is looked up in figure 3.2.2. The resulting sampling points are listed in table 3.2.1.

v in m/s	Re	$\zeta_{w,arm}$
1	$1.89 \cdot 10^3$	0.95
5	$9.44 \cdot 10^3$	1.1
10	$18.87 \cdot 10^3$	1.2
20	$37.76 \cdot 10^3$	1.2
30	$56.64 \cdot 10^3$	1.2
40	$75.52 \cdot 10^3$	1.2
50	$94.4 \cdot 10^3$	1.2

Table 3.2.1: Sampling points for estimation of wind force on the UAV. The values for $\zeta_{w,arm}$ are looked up in [49] (see figure 3.2.2).

The UAV's body is assumed to have dimensions of $15 \times 20\,\text{cm}^2$, which results in a height to span ratio of 0.75. In [49], a constant drag coefficient $\zeta_{w,body}$ of 1.18 is given for such a surface and $Re > 1000$, which means that there is no further dependence on v. With known cross-sectional areas of the body (A_{body}) and the arms (A_{arm}), the exerted force results in

$$F_w = \frac{\rho}{2} v^2 \left(\zeta_{w,body} A_{body} + n \zeta_{w,arm} A_{arm}\right). \tag{3.2.3}$$

Assuming the density of air with $1.1614\,\text{kg/m}^3$ at 300 K [28] and taking the values for $\zeta_{w,arm}$ and $\zeta_{w,body}$ as stated above, (3.2.3) is evaluated for seven different wind speeds. The results are quadratically interpolated in MATLAB and depicted in figure 3.2.3. The

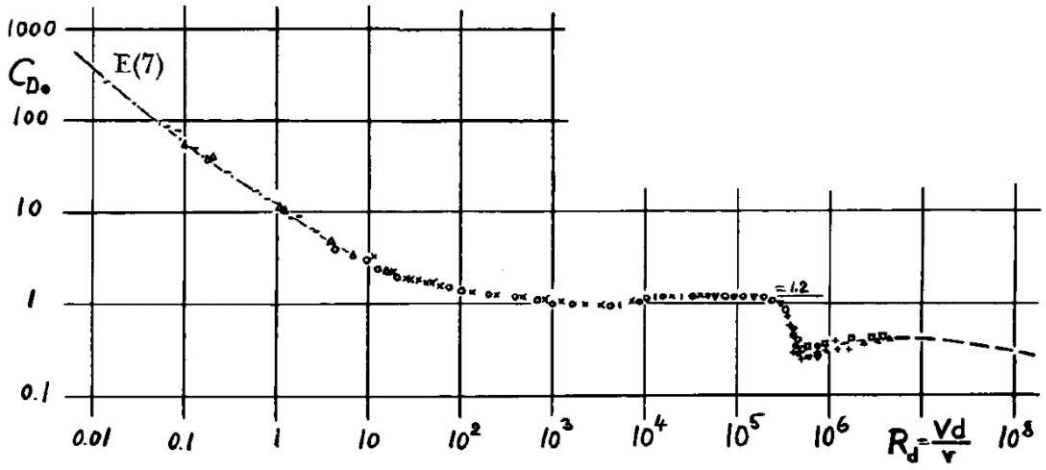

Figure 3.2.2: Drag coefficient for cylindrically shaped objects as a function of the Reynolds number with flow normal to the axis. The drop of the drag coefficient at $R_d \approx 3.5 \cdot 10^5$ is because flow changes from laminar to turbulent [49].

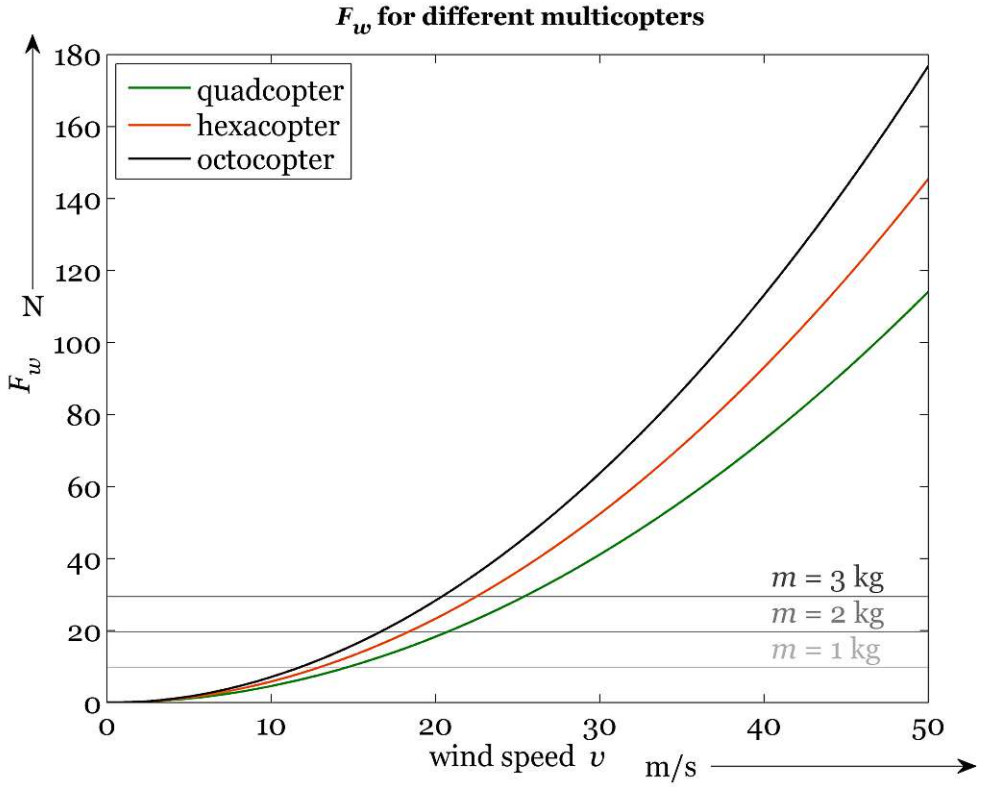

Figure 3.2.3: F_w over wind speed, depending on the number of rotors ($n = 4$ for a quadcopter, $n = 6$ for a hexacopter and $n = 8$ for an octocopter). The grey lines show the resulting weight force for 1, 2 and 3 kg with $g = 9.81\,\mathrm{m/s^2}$.

three grey horizontal lines in figure 3.2.3 represent the resulting weight force on the drone caused by earth gravity for weights of 1, 2 and 3 kg. The main problem with upwind is that it cannot be controlled like side wind, because it is not possible to invert the direction of rotation of the drone's propellers. Thus, there is no way to directly countervail upwind. However, the drone's weight and the resulting weight force can be used up to a certain point simply by slowing down the propellers' rotational speed. In other words, the heavier a drone is the better will its resilience to upwind be. According to the model presented, a quadcopter with a take-off weight of 1 kg could withstand upwind speed of about 15 m/s and a quadcopter with 3 kg could withstand about twice as much. Nevertheless, it should be taken into account that in reality it is not possible to completely switch off the UAV's rotors as the multicopter would become unstable immediately. As a result, the true wind resilience is lower as there is always some remaining uplift caused by the rotating propellers.

To get a better and more accurate view on the resilience of a multicopter to upwind than through the very rough and simplified mathematical description developed in this section, it is inevitable to do some wind channel experiments. A further necessary step would be to measure the actual strength of wind above a hot vessel after tapping.

3.3 Test flight in industrial environment

In the previous sections, thermal and aerodynamic influences on a UAV during a measurement flight were discussed. The observations made are based on mathematical models and are therefore very theoretical. To expand the view on the drone's behaviour under harsh conditions, a test flight with a multicopter is done in an industrial environment. For organisational reasons it is not possible to carry out the flight in a steel plant, which would obviously be the best case to determine the occurring problems. However, it can be enabled to do the test flight in the RHI-factory in Veitsch, Styria, where refractory is produced. The factory provides environmental conditions like strong dust exposure, relatively high temperatures (due to a tunnel kiln with 1800 °C where refractory material is fired) and wind. These are also the three main aspects that are observed during the flight.

3.3.1 Equipment

Temperature logger

To get information about the temperature in the UAV's immediate surrounding, the drone has to carry a temperature logger. The special requirements for this device are a wide measuring range up to high temperatures, low weight and portability. These requirements are met with a device consisting of the following main components:

- Raspberry Pi Zero W
- PT1000 temperature sensor Heraeus M1020
- analogue-to-digital converter MCP3008
- signal LED

- push button to start or stop the measurement

Although microcontrollers are generally better suited for simple sensor controlling, the single-board computer Raspberry Pi is chosen here because it enables direct on-board storage of the measured data. Thus, no further data transmission is necessary. A PT1000 element is a platinum resistance with a standardized, widely linear temperature dependence and a resistance of 1000 Ω at 0 °C. Compared to the more commonly used PT100 (platinum resistance with 100 Ω at 0 °C), the use of a PT1000 reduces the relative measuring error caused by the line resistance of the measure circuit. Furthermore, the current through the resistance is 10 times lower than the current through a PT100 element, which has the advantage of lower energy consumption. The voltage drop at the PT1000 element is converted into a digital signal with an ADC and used to calculate the resistance and in further consequence the resulting temperature on the Raspberry Pi. The measure circuit furthermore contains a LED signalling an active measurement and a push button to start a new measurement cycle or to stop the measurement. The wiring of the LED and the push button is shown in figure 3.3.1. The push button is used to give a digital

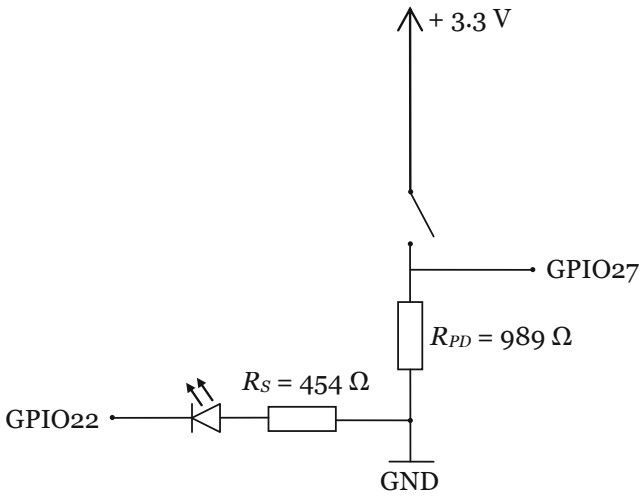

Figure 3.3.1: Wiring of the LED and the push button. R_{PD} is a pull-down resistance to guarantee a stable high- or low-signal at the Raspberry Pi's GPIO27. The diode can be switched on and off with GPIO port 22. R_s is the diode's series resistance.

input signal to pin 13 of the Raspberry Pi, which is GPIO27. To guarantee a clearly distinguishable high- or low-signal (i.e., 3.3 V or 0 V), a so-called pull-down resistance is needed. If the switch is open, the given voltage at GPIO27 will be 0 V as no current flows through R_{PD}. As soon as the switch is closed, 3.3 V drop at R_{PD} and apply to the pin. In general it does not matter a lot how big the resistance R_{PD} is, however the circuit should be insensitive to coupled electrical interference and therefore R_{PD} should not be

too small. A value of around 1 kΩ is suitable.

GPIO22 is an output port, i.e., it is set either high or low by the program running on the Raspberry Pi. When it is set high (3.3 V), current flows through the LED and its series resistance R_S and the LED is on. R_S is needed to limit the current through the LED so that the component is not destroyed. Furthermore, the LED's brightness can be adjusted with the choice of R_S. In the case of $R_S = 454\,\Omega$, the measured voltage drop at the LED is 1.9 V and with Ohm's law the current through the LED can be calculated to

$$I = \frac{3.3\,\mathrm{V} - 1.9\,\mathrm{V}}{R_s} = 3.08\,\mathrm{mA}.$$

The wiring of the MCP3008 and the PT1000 element is depicted in figure 3.3.2. The

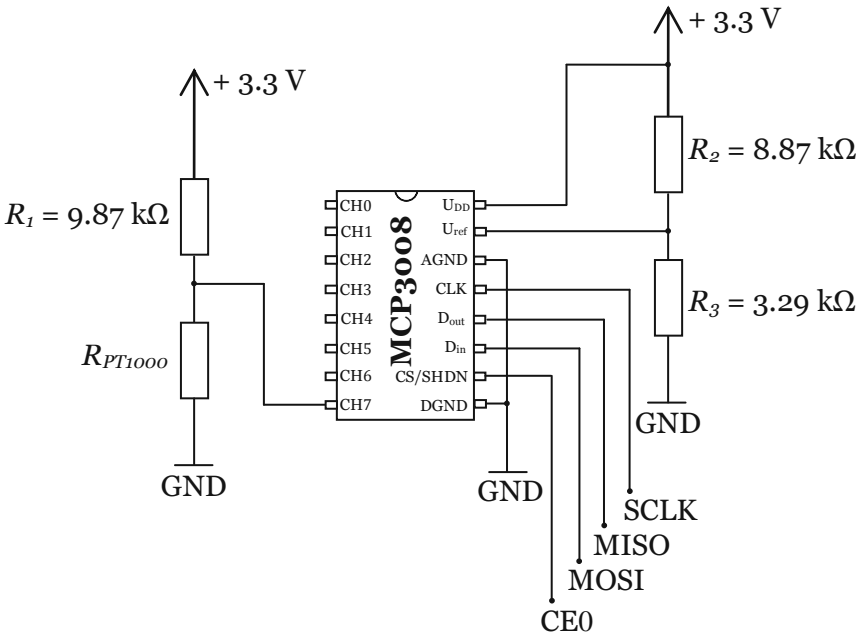

Figure 3.3.2: Wiring of the ADC MCP3008 and the PT1000 element. The value of R_{PT1000} is calculated out of the voltage drop at the resistance which is placed in a voltage divider. The ADC is controlled via SPI.

MCP3008 is controlled via SPI (serial peripheral interface), which is a synchronous data bus system enabling communication according to the master-slave principle. The Raspberry Pi provides four GPIO pins especially for SPI. These are SCLK (serial clock), which has to be connected with the ADC's CLK-pin, MISO (master input, slave output), which has to be connected with the D_{out}-port that shifts out the results of the A/D-conversion, MOSI (master output, slave input), which has to be connected with D_{in} to load channel configuration data into the device, and CE0 (chip enable 0), which is connected with the ADC's chip-select-port to initiate communication [2]. Both analog and digital ground (AGND, DGND) are connected to the Raspberry Pi's ground and a voltage of 3.3 V is

connected to U_{DD}. Since the MCP3008 is a 10-bit-ADC, its resolution is $\frac{U_{ref}}{1024}$. Hence, it makes sense to choose U_{ref} similar to the highest expected voltage on the input channel (in this case channel 7) to achieve the best temperature resolution. Referring to [3], the PT1000 element can be operated up to temperatures of 500 °C which corresponds to a resistance of 2809.78 Ω with respect to the specification in the norm DIN EN 60751 [13]. With this value, the maximum voltage at CH7 can be assumed to be

$$U_{max} = \frac{R_{PT1000}}{R_1 + R_{PT1000}} 3.3\,\mathrm{V} = 939\,\mathrm{mV}.$$

With the voltage divider of R_2 and R_3, the reference voltage results in

$$U_{ref} = \frac{R_2}{R_2 + R_3} 3.3\,\mathrm{V} = 892\,\mathrm{mV},$$

which is a sufficient adjustment.

The sensor controlling software is written in the programming language Python. Python provides a library called `spidev` for interfacing a Raspberry Pi with SPI-controllable devices and a special class for the MCP3008 which makes its use very easy. The main functionality of the software is to calculate the temperature out of the value delivered by the ADC. The voltage U_{meas} at the input channel is calculated by multiplying the digital output value of the ADC with its resolution. In a second step, R_{PT1000} is calculated as follows:

$$\begin{aligned} \frac{R_1 + R_{PT1000}}{R_{PT1000}} &= \frac{U_{DD}}{U_{meas}} \\ (R_1 + R_{PT1000})\, U_{meas} &= R_{PT1000} U_{DD} \\ R_1 U_{meas} &= R_{PT1000}\,(U_{DD} - U_{meas}) \\ R_{PT1000} &= R_1 \frac{U_{meas}}{U_{DD} - U_{meas}} \end{aligned} \tag{3.3.1}$$

According to DIN EN 60751 [13], the following relation between a platinum resistance and its temperature is given for a temperature range between 0 °C and +850 °C:

$$R(T) = R_0 \left(1 + AT + BT^2\right) \tag{3.3.2}$$

with the temperature T, the coefficients $A = 3.9083{\cdot}10^{-3}\,°\mathrm{C}^{-1}$ and $B = -5.775{\cdot}10^{-7}\,°\mathrm{C}^{-2}$ and the resistance R_0 at 0 °C. As a result, the temperature can be calculated with

$$T = \frac{-A + \sqrt{A^2 - 4B\left(1 - \frac{R}{R_0}\right)}}{2B}. \tag{3.3.3}$$

These calculations are implemented in the software as shown in listing 3.3.1.

```
1 #defining instance of MCP3008-class
2 adc = MCP3008()
3
4 #measuring program start time
5 t0 = time.time()
```

```
6  res1 = 9870
7  udd = 3.3
8  uref = 0.892
9  resol = uref/1024
10 pt = 1000
11 coeffa = 0.0039083
12 coeffb = -0.0000005775
13
14 ...
15
16 #reading ADC value and calculating voltage
17 value = adc.read(channel = 7)
18 umeas = resol*value
19
20 #calculating resistance of PT1000 element
21 respt = res1*umeas/(vdd-umeas)
22
23 #calculating resulting temperature
24 temp = (-coeffa + math.sqrt(coeffa*coeffa - 4*
     coeffb*(1 - (respt/pt))))/(2*coeffb)
25
26 #writing time stamp and temperature value into
27 #text file
28 data.write(str(int(time.time() - t0)) + ' ' + 
     str.format("{0:.2f}", temp)+ '\n')
```

Listing 3.3.1: Temperature calculation out of ADC value. The values are written into a text file together with a time stamp.

Every second, a measured temperature value is written into a text file together with a time stamp. To be able to differ different sections of a long measurement cycle, the push button can be used to set a marker in the file. The marker includes an enumeration of different measurement sections. Furthermore, the push button can be used to terminate the program by pressing it for more than 1 second. Listing 3.3.2 depicts the implementation of these functionalities. The python library `RPi.GPIO` provides many functions to handle the Raspberry Pi's GPIO ports. The function `add_event_detect()`, which is defined in this library and used below, facilitates interrupt-like behaviour for GPIO ports. As the operating system running on the Raspberry Pi is not real-time capable, the response time to a signal on the interrupt-pin is way longer than when using a microcontroller. Hence, it may be exaggerated to call the functionality "interrupt" in a proper sense. Nevertheless, the performance is definitely sufficient for a push button.

```
1 #Enabling interrupts for GPIO pin 27
2 GPIO.add_event_detect(27, GPIO.RISING, callback=
    measure, bouncetime=300)
3
4 #Callback function (called whenever the push
5 #button is pressed)
6 def measure(channel):
```

```
7
8           #turning LED off
9           GPIO.output(22, False)
10          #incrementing counter with an additional
11          #function
12          counter = mycounter()
13          #waiting for 1 second
14          time.sleep(1)
15          #closing script when button is still
16          #pressed
17          if GPIO.input(27) == True:
18                  GPIO.cleanup()
19                  data.flush()
20                  os.fsync(data)
21                  data.close()
22                  sys.exit()
23          #writing marker into the text file
24          data.write('--measurement' + str(counter
              ) + '--\n')
25          #turning LED on again
26          GPIO.output(22, True)
```

Listing 3.3.2: Push button functionalities. The push button can be used either to set a marker in the text file or to terminate the script.

The temperature logger is shown in figure 3.3.3. The PT1000 element is soldered on a heat-resistant cable. The idea is to mount the Raspberry Pi and the circuit directly on the UAV's body and fix the temperature resistance on one of the multicopter's arms that carry the rotors to avoid measuring errors due to heat generation of the UAV itself.

The maximum temperature of the platinum resistance is 500 °C [3], however in reality the temperature is limited by the melting point of the solder, which is lower. As shown in section 3.1 temperatures of more than 60 °C will destroy the UAV's battery, which is why the test flight will not be performed in regions with higher temperatures anyway. The logger's resolution is approximately 1 K, which is enough for the application here. A better resolution could be reached by better alignment of the maximum voltage at the PT1000 element and U_{ref}, e.g., by using potentiometers or driving the temperature resistance with an adjustable constant current source instead of a voltage divider.

UAV

The drone used for the test flight is a DJI Mavic Pro. It is a relatively small quadcopter with a diagonal size of 33.5 cm and a rather long maximum flight time of 27 minutes. The drone has a 4K-camera on board, which is mounted on a 3-axis gimbal. The UAV's weight including battery, gimbal and camera is 743 g. A special feature of the drone is its optical stabilisation for indoor flights, which is why this drone was chosen for the test flight. The drone with the mounted temperature logger is shown in figure 3.3.4.

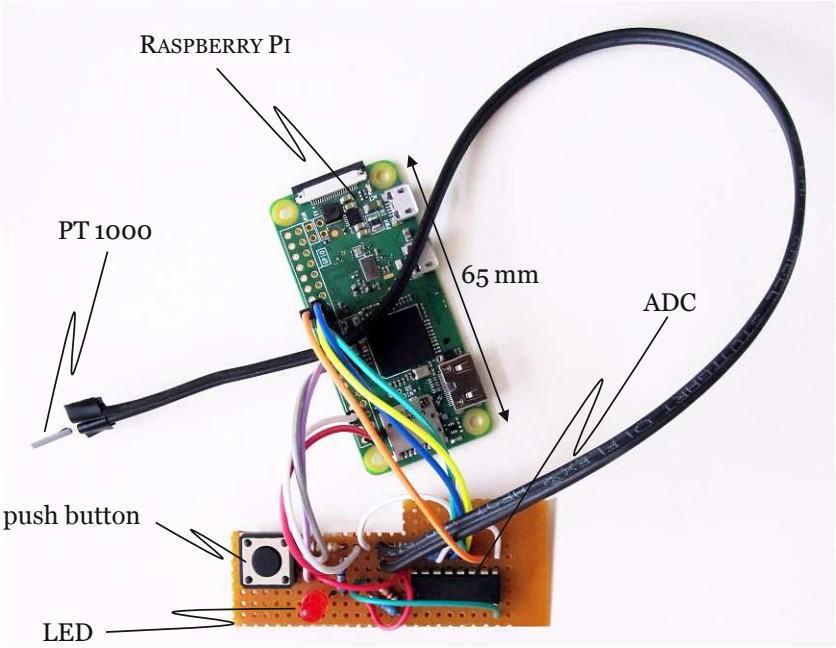

Figure 3.3.3: Portable temperature logger consisting of a RASPBERRY PI, an ADC, a signal LED, a push button and a PT1000 element which is soldered on a cable.

3.3.2 Observations

The focus of the observations during the test flight was on the impact of the three environmental conditions temperature, dust and wind. The presumptions were that temperature may cause instabilities of the drone due to density differences of the air and dust may deposit on the drone so that the camera lens becomes dirty. Furthermore it should be observed how good the device actually copes with wind.

Temperature

The area which was chosen to test the UAV's behaviour at temperatures above room temperature is shown in figure 3.3.5. On the left side of the image, the side wall of a tunnel kiln can be seen. It is made of bricks and hedged with iron girders. Inside the tunnel kiln, refractory material is burned with 1800 °C. The burning zone is on one side of the kiln and the refractory is slowly moved through the burning zone and the tunnel, so that it cools down slowly. The maximum temperature is measured directly besides the burning zone (about 35 °C) and the minimum temperature of 20 °C is measured at the end of the tunnel kiln. In between, temperature behaves widely linearly.

During the flight along the tunnel kiln, no instabilities of the drone can be observed. Although of course small changes of air density occur between 20 and 35 °C, the drone can control and balance them automatically.

An interesting aspect which could not be tested in the RHI factory would be how the drone behaves at bigger temperature changes, as they occur in steel plants. It is not

Figure 3.3.4: DJI Mavic Pro with mounted temperature logger. For the Raspberry Pi's power supply, the UAV's battery pins are used (red and black wire on top of the drone).

ensured that immediate temperature changes over a few decades may be controlled in such a satisfying way too.

Dust

It can be imagined that dust is omnipresent in every stage of a refractory production line. The drone creates wind and therefore whirls up a lot of dust during a flight.

After every flight the device is checked on dust deposit, however no dust can be found on the UAV. The camera lens stays clean as well. Dust apparently only occurs in the drone's surrounding but does not deposit on the UAV itself. However, it has to be mentioned that the situation may be different when a UAV is operated in a dusty environment for a longer time, e.g., several months.

Wind

To test the influence of wind, a flight is performed in front of some blowers at the end of the tunnel kiln which are used to accelerate the cooling process of the refractory bricks. The blowers are the tunnels with pentagonal cross-section that can be seen in figure 3.3.6. It can be observed that the relatively strong wind in this area does not harm the UAV at all. The drone is not as smooth as in completely windless areas as it obviously has to balance wind force. However, the movements are very small (the device jiggles a little bit but does not change its position) and they cannot be recognised in the video taken with the on-board camera, as the gimbal stabilises the camera position very well.

These results comply with section 3.2 where it was shown that side wind usually does not affect stability of a drone.

Figure 3.3.5: Area where the influence of temperature changes on the drone's flight behaviour was tested. On the left side, the side wall of a tunnel kiln can be seen (brick wall). Temperature increases in the course of the corridor from 20 °C up to 35 °C.

Other

Although the environmental aspects described above do not cause serious problems during the test flight, some other problems occur that have not been considered beforehand.

Firstly, the calibration of the UAV is problematic. Before every flight, the drone's sensors have to be calibrated (e.g., the drone is put on the ground and its barometer is reset – this allows to measure the drone's flying height afterwards). Especially the calibration of the magnetic sensor, which acts as a compass, is difficult because of magnetic interference. There are many iron girders and electrical machines inside the RHI factory which attenuate and disturb the earth's magnetic field. In the end, calibration has to be done outdoors and it cannot be done before every flight in a different area, which is usually recommended.

The second problem is caused by the rather weak illumination in some areas inside the factory. The DJI Mavic Pro has several optical sensors for indoor stabilisation. Whenever illumination is insufficient, these sensors do not work any more and the UAV becomes very unstable (i.e., it can not hold its current position and starts to move around arbitrarily). These situations are critical as it is extremely difficult to control the drone manually when self-stabilisation does not work. However, as it could always be moved back into better illuminated areas, the malfunction only lasted for a few seconds and the drone did not crash.

Summing up, the result of the test flight is basically positive. Even though no GPS

Figure 3.3.6: Area at the end of the tunnel kiln. The pentagonal tunnels in the background are blowers to cool down refractory.

signals were available and the magnetic sensor couldn't detect the earth's magnetic field with sufficient strength, the UAV's flight was very smooth and stable. This suggests that stabilisation alone is not a big challenge when using UAVs indoors.

4 Obstacle Detection

The two major technical challenges when using autonomous drones in indoor environment are the detection of obstacles on the one hand and navigation on the other hand. Currently, a lot of research is done in this area. In many papers, as for example in [29] or [91], systems using one and the same technology to solve both problems at once are developed and described. However, in principal there are many entirely different requirements on the two systems. To give an example, autonomous obstacle detection has to be highly reliable to failures whereas accuracy plays a bigger role in navigation. A crash of the UAV may be caused when the obstacle detection system fails even only for a very short time (when considering obstacles that are moving with high velocity), however the distance between multicopter and obstacle does not necessarily have to be known centimetre-precisely. On the other hand, precise laser measurements require knowledge about the exact relative position of the measurement device to the measured object. This precision has to be provided by the navigation system. At the same time it would not be a serious problem if there were no navigation data available during a flight for a short time.

Thus, this thesis treats obstacle detection systems and navigation systems separately and does not aim at finding one system that may be suitable for both issues.

This section concentrates on obstacle detection. At first, different possibilities and technologies are described and discussed briefly. Afterwards a conclusion is drawn where the most important advantages and disadvantages of promising technologies are pointed out.

4.1 Available systems

4.1.1 Single camera systems

In general it is possible to use a single camera for obstacle detection. However, the problem is that a single camera doesn't directly allow depth perception. This means that there is no information about the distance of an object to the camera in an image. To gain this information, additional methods are needed to detect shapes in an image and guess their distance to the camera.

Optical Flow

One popular approach to extract depth information out of a sequence of pictures is the use of optical flow (OF). Generally speaking, the optical flow of a sequence of pictures is a vectorfield representing the velocities of the movement of visible points projected onto the image plane. This also implies that the optical flow does not necessarily provide information about the real motion of an object, but only about the "visual" motion.

A popular example for this contradiction is the so-called "Barber's pole illusion", which is a rotating pole with diagonal stripes on it. Because of the rotation it looks as if the

stripes were moving vertically [99]. In this case, the resulting optical flow vectors point in vertical directions although the pole rotates horizontally (see figure 4.1.1).

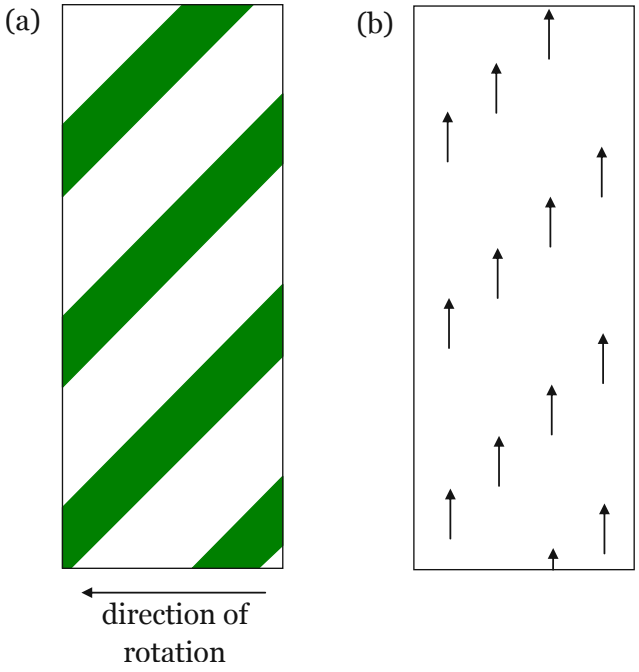

Figure 4.1.1: Diagonally striped rotating pole (a) and resulting optical flow vectors (b).

Furthermore, there is no way to distinguish between movements of the camera and movements of an object on the basis of optical flow. With respect to an obstacle detection system for a UAV, this issue is rather unproblematic as it does not make a difference whether an object comes too close to the non-moving drone (e.g., a crane in a steel plant) or whether the moving drone comes too close to an object. Howsoever, the interesting question is how to read depth information out of optical flow vectors. Therefore it is necessary to take a closer look at the behaviour of the vectorfield. Objects being far away from the camera objective appear to move more slowly than objects near the camera objective. Thus, the optical flow vectors of far away objects are shorter than those of near objects. Nevertheless, this only works for objects passing the camera sideways. For objects moving towards the camera, the effect is used that nearing objects seem to become bigger. As a result, the OF vectors of such an object are arranged radially and point towards the picture's edge.

One big difficulty with optical flow algorithms for obstacle detection is to get both accurate results and a short calculation time to guarantee real-time capability [89]. One possibility to avoid this problem is the combination of different methods, as proposed in [82]. In this case, a fast but weak optical flow algorithm is used to support another reliable but slow obstacle detection technology.

Structure from Motion (SfM)

Another possibility to extract depth information out of a sequence of images is the Structure from Motion (SfM) approach. The principle is quite similar to the optical flow estimation, however SfM doesn't create a vector field but performs feature tracking. With a suitable feature detecting algorithm like the scale-invariant feature transform method (SIFT), specific objects can be detected in an image. Hence, the trajectories of different features and objects over multiple images can be created. The SfM method uses these trajectories to reconstruct camera motion as well as the motion of objects in 3D-space.

Especially the correct feature matching is a very difficult part in the whole algorithm and not every feature is always matched correctly (this issue also strongly depends on the pictures' content). This results in outliers in the trajectories. Thus, a further algorithm has to be used to filter the trajectories and remove these outliers.

There is currently a lot of research done on SfM algorithms. In some papers (e.g., [72] and [40]), even real-time capable algorithms are developed. One important practical application of SfM methods is the construction of three-dimensional landscape models [101] as an alternative to laser scanning which is way more expensive.

Other approaches

There are several further approaches to perform obstacle detection with single cameras. Many of them are based on the assumption that there is a flat area, which is the floor, and that there are objects rising from the flat area. The challenge then is to find out wheter a point in the image belongs to the floor or to an object. Simple algorighms are based on colours, i.e., the ground floor has a different colour than the objects. Other works describe more complex algorithms based on homographical transformations and feature detection [38].

All in all, single camera systems have some potential to become usable for practical obstacle detection applications. However, still a lot of research has to be done to reach this goal.

4.1.2 Stereo camera systems

In contrast to one single image, two images can contain depth information. For this purpose, the images have to be taken from a slightly different position. The principle is very similar to the human visual system: human stereoscopic vision is based on two eyes that are arranged at a distance of a few centimetres.

The method to calculate the distance of a point in the image to a stereo camera is called triangulation. Figure 4.1.2 shows the typical parameters of a stereo camera system. C_1 and C_2 are the centers of projection of the two cameras. The line between the cameras is called baseline and has the length B. The so-called epipolar plane is stretched by C_1, C_2 and M. The cutting lines between the epipolar plane and the two image planes I_1 and I_2 are called epipolar lines and marked with l_1 and l_2. An epipolar line is in so far relevant as for every point in an image, e.g., m_1, the corresponding point m_2 can only lie on the epipolar line l_2 in the other image. The normal distance Z of the baseline to a point M

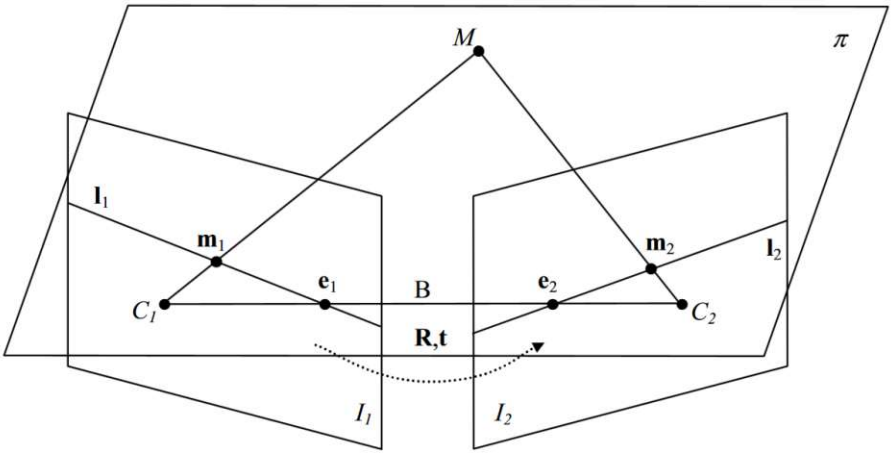

Figure 4.1.2: Typical arrangement of a stereo camera system. The important parameters are the camera positions C_1 and C_2, the projections m_1 and m_2 of point M onto the image planes and the baseline with length B. The distance of M to the baseline can be calculated out of these variables and the inner camera parameters [86].

in 3D-space can be calculated with the following formula:

$$|Z| = \frac{fB}{|x_1 - x_2|}. \tag{4.1.1}$$

The variable f is the focal length of the camera which is usually known as long as the camera has been calibrated. x_1 and x_2 are the pixel positions in x-direction of the pixels m_1 and m_2. The absolute difference $|x_1 - x_2|$ is called disparity. The exact derivation of (4.1.1) can be found in [86].

It can be seen that the overall principle of extracting depth information out of two images is rather simple. However, the challenge is to find the exact pixel positions of corresponding points in the images. This issue is called correspondence problem. As described above, the area in which a corresponding point lies can be restricted to the epipolar line. However, in a general case as depicted in figure 4.1.2, the epipolar lines in the images are neither known nor parallel and the correspondence problem is two-dimensional, which means that a corresponding point could lie anywhere in the other image. Nevertheless, there are some possibilities to reduce the correspondence problem to a one-dimensional problem.

The simplest method is to adjust the cameras in so-called standard stereo-geometry. This means that the camera axes are parallel and the baseline is parallel to the horizontal edges of the images. It is important to adjust the cameras very accurately, because otherwise unpredictable measuring errors occur. Another disadvantage, which is much more significant, is that measurement accuracy is better the bigger the relation of baselinelength B to normal distance Z is [42]. This means that from that side of view big values for B are desirable. Nevertheless, a longer baseline leads to a smaller shared projected scene of the cameras. In other words, the area that is recorded from both cameras becomes smaller when the cameras are positioned further apart from each other. The solution to overcome these problems is called image rectification. An image rectification algorithm geometrically transforms two camera images that are not in standard stereo-geometry in

a way that the images have the same properties as if they would have been taken with cameras in standard stereo-geometry.

With an image pair with either rectified images or images taken with cameras in standard stereo-geometry, the epipolar lines in two images of a stereo camera pair are equal and furthermore parallel to the horizontal image edge. Hence, the search for a corresponding point is reduced to a one-dimensional problem.

An algorithm to detect obstacles with a stereo camera could work as outlined here: in the first step the images are, if necessary, rectified. Then, the disparities are calculated by solving the correspondence problem. A disparity map is generated, i.e., a grey-valued image where each grey-value of a pixel stands for a specific disparity. Afterwards, a depth-map can be calculated out of the disparity map with equation 4.1.1. There are several methods to identify obstacles in a depth-map. One possibility would be to look at every single pixel and react on pixels that are too near. In [46], the map is split up into a larger-meshed grid which reduces resolution but of course also the required computation power.

One big problem of both single and stereo camera systems is that depth measurement and obstacle detection does not work in regions with poor or no texture. E.g., a single-coloured wall drawing closer to the camera cannot be detected. The reason is that in such a case the correspondence problem cannot be solved unambiguously as there are too many pixels with the same colour. Another drawback is that the functionality of camera systems strongly depends on the lighting conditions of the scene. The system does not work properly in gloomy or dark environments.

There are many things that can still be improved in stereo vision technology and a lot of research is currently done. However, the principle is already used in loads of mobile robot applications to detect obstacles, as for example in [74]. Another area of application is autonomous driving [25].

There are systems on the market which are fit for use, like the Pointgrey Bumblebee. Concerning the use for autonomous drones, one problem to consider is the high computation power needed to execute the image processing algorithms.

4.1.3 Structured light

The structured light method describes the principle of projecting a regular pattern onto a surface and measuring the distortions of the pattern which occur due to unevenness of the surface (figure 4.1.3). The most popular example for a structured light sensor is the Microsoft Kinect. This is a sensor system to recover three-dimensional scenes, which was developed by Microsoft in 2010. It consists of an infrared projector, an infrared camera, an RGB-camera and some hardware on which a depth map is calculated out of the reflected infrared pattern. The RGB-camera is mounted on the device mainly because it was originally designed as a hardware device to control the gaming console XBox 360. The camera was thought to be used for face recognition.

Although the Microsoft Kinect is a gaming device, it is often used for research purposes in the field of computer vision, for example to develop obstacle detection systems [78]. Equal to stereo cameras, the device delivers a depth-map, which is why a system for obstacle detection could be realised as proposed in section 4.1.2. The advantage of a structured light system as the Microsoft Kinect compared to a stereo camera system

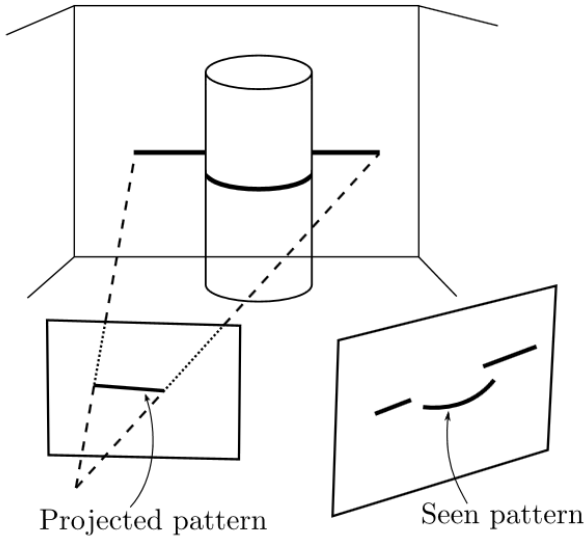

Figure 4.1.3: Principle of structured-light. The shape of the surface can be reconstructed out of the distortion of the projected pattern [36].

is that it works in textureless regions as well. However, the system's performance becomes quite weak on poorly light-reflecting surfaces.

4.1.4 Laser

Lasers provide various possibilities for distance measurements and can also be used for obstacle detection. There are mainly three different methods to use lasers for this purpose, which will be described below.

Time of Flight (ToF)

The simplest method to measure distances with lasers is a ToF-measurement. A laser source emits a beam which is reflected by an object. The reflected laser beam is detected and the time interval between sending and receiving the beam is measured. With this information and the known velocity of light, the distance can be calculated easily with elementary physics. In vacuum or air with a refraction index of approximately 1, the distance d can be calculated with

$$d = \frac{c_0 \Delta t}{2} \tag{4.1.2}$$

with the speed of light c_0 and the time difference Δt. The factor of two in the denominator takes into account that the laser beam travels the distance to measure twice. Due to the low reaction time, high distances up to tens of kilometres can be measured. On the other hand, a very accurate time measurement is necessary to guarantee high accuracy. E.g., for an accuracy of 1 mm, time has to be measured with an accuracy of 6.7 ps [24]. However, for the application of obstacle detection, an accuracy of a few centimetres would be sufficient. As an example, the laser scanner SICK S300 MINI, which uses the ToF-principle,

measures with resolutions of 30 mm to 70 mm, depending on the absolute measure distance. Furthermore, the device covers an arc of 270 °, thus an omnidirectional view could be realized with 2 devices. The power consumption of 12 W excluding the output load is higher than that of a camera, but still does not inhibit from battery-powered mobile use. A problem might be the weight of 0.8 kg without connecting cables [21].

Phase-shift range finder

The phase-shift principle uses a laser with constantly modulated optical power. This means that, e.g., the laser emits a sine-shaped signal with frequency f. As with ToF, the beam is reflected and the reflected beam is collected by a photo diode. In this case, not the time difference but the phase shift is measured. It is given by

$$\Delta\varphi = 2\pi f \Delta t, \tag{4.1.3}$$

and can be used to calculate the distance with (4.1.2):

$$d = \frac{1}{2} c \frac{\Delta\varphi}{2\pi f}. \tag{4.1.4}$$

Compared with ToF, a phase-shift range finder provides results with higher accuracy even though the metrological effort is lower as no exact time measurement is needed. However, there are some drawbacks too.

Firstly, the measurement distance is not that high, especially for mobile devices. This is because the laser emits a signal continuously and therefore the signal power has to be lower to keep the overall consumed power comparable to that of a ToF-device. Secondly, the laser beam is constantly modulated. Thus, the measured phase shifts are the same for distances equal to multiples of half the wavelength. To guarantee an unambiguous measurement, one possibility would be to keep the measurement distance less or equal than half of the wavelength, i.e., $d \leq \frac{c}{2f}$ [24]. In limited space, as for example in a steel plant, it would be possible to estimate the biggest possible distance, e.g. 100 m, which is half the wavelength of a modulated laser beam with 1.5 MHz.

An example for a commercially available phase-shift laser range finder is the SICK LMS400.

Frequency Modulated Continuous Wave (FMCW) Optical Radar

The use of FMCW-radar is a better solution to overcome the problem of unambiguous measurements than just limiting the range. In this technology, a laser beam with continuously changing frequency is sent out. The beam is reflected by an object and reaches a detector. Of course, the frequency of the sent signal did not change on its way to the object and back, however the frequency of the signal in the signal generator did change during this time. As the speed of frequency change is known, the distance to the object can be calculated out of the frequency shift between the received and the currently generated signal.

Triangulation

The principle of triangulation as described in section 4.1.2 can also be applied for laser measurement system. Here, the reflected laser beam is detected by a camera or by a

photodiode with position resolution. If the distance of the object to the camera and the laser changes, the position of the laser point on the camera image will change as well. The principle is shown in figure 4.1.4. In the figure, f is the distance between image plane and

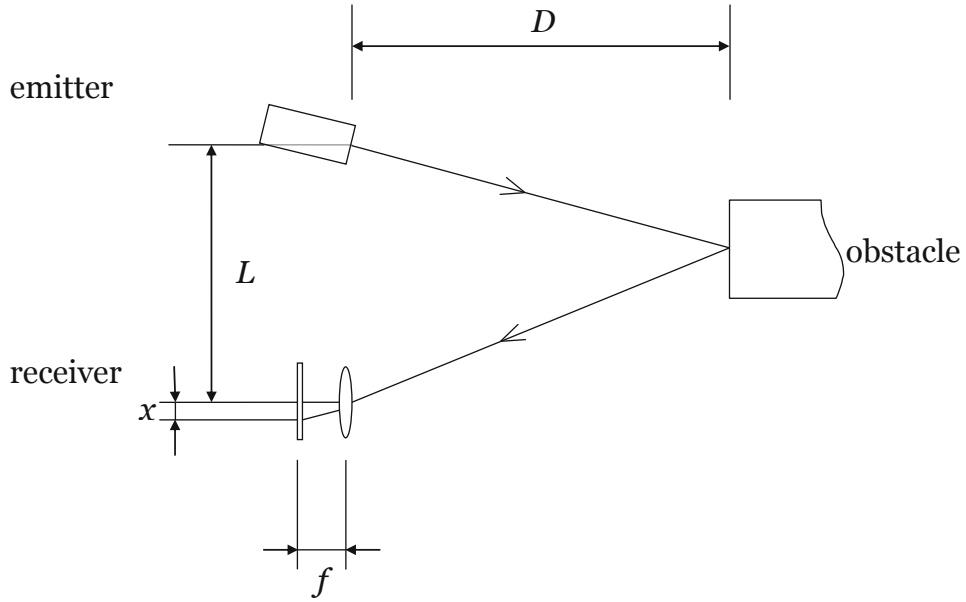

Figure 4.1.4: Principle of laser triangulation. If the distance between emitter and receiver L, the focal length f and the deviation of the laser point from the center of the image plane x are known, the distance D to the obstacle can be calculated. Adapted from [76].

lens. Similar to (4.1.1), the distance D can be calculated out of the position of the laser point in the camera image:

$$D = f\frac{L}{x}. \tag{4.1.5}$$

Generally speaking, laser measurement devices provide extremely good accuracy. Depending on the technology, they can be used for very far-range (km) measurements (ToF, FMCW) as well as for low-range (m, cm, mm) measurements (phase-shift, triangulation). One problem with commercial laser scanners is that they cannot measure a whole area with one shot (as for example a camera). This is because a laser beam does not have a noticeable opening angle. Using one laser for each point would be inefficient. Hence, the measurement has to be done sequentially by moving the laser scanner steadily.

4.1.5 Infrared

Infrared distance sensors work with the same principles as lasers. However, in contrast to laser based sensors they have a way lower range. Infrared distance measuring units with the longest measuring ranges available on the market are the Sharp GP2Y0A710K0F

with 100 - 550 cm [12] or the TeraRanger One with a range up to 14 m [7].

4.1.6 Sonar

Sonar ("sound detection and ranging") is a very widespread and popular technology for many applications as for example distance measurements, obstacle detection or even material testing [94]. The measurement technique is based on the ToF-principle as described in section 4.1.4. However, the signal used is not light but ultrasound. Ultrasound is defined as an acoustic wave with a frequency of more than 20 kHz. As 20 kHz is the upper limit of a human ear's bandwidth (it should be mentioned that this limit strongly depends on the human's age: usually it is significantly reduced for older people), ultrasound is inaudible. Some reasons for the technology's popularity may be that it is rather simple to build measurement setups, there is a big range of cheap sensors with different properties (e.g., digital or analogue triggering, directional characteristics) and the accuracy of the measurement is satisfying for many applications. With ultrasonic sensors, all materials can be detected as long as they do not absorb sound (e.g., textile material or soft rubber). The measurement is independent of the lighting conditions and the light reflection properties of a material. Furthermore, ultrasonic sensors have a high level of intrinsic safety. This means that the sensors can be used in dangerous industrial environments (for example environments with highly flammable gases), because the sensors are constructed in a way that they cannot cause an accident (e.g., by an electric spark and a resulting inflammation of the gas). Another advantage is the robustness towards dust or dirt. The sensors even work in foggy regions with no line of sight to the detecting surface or object.

A well-known and well-established application of sonar is ultrasound tomography, for example in prenatal diagnostics. There is still a lot of research done in this area to further improve the technology itself as well as the imaging process [83] [39].

Despite the great opportunities of the technology, there are also some drawbacks. To receive a good echo, the reflecting surface should be normal to the sensor signal and the surface must have a certain minimum size, depending on the distance to the sensor. This is because the measurement area has the shape of a cone and thus, its diameter grows with the distance.

In general, ultrasonic sensors aren't sensitive to loud noise in their environment. However, when there is noise in ultrasound range, e.g., from emergent air out of an overpressure valve, problems may occur.

As the velocity of sound is way lower than that of light, the measuring frequency of ultrasonic sensors is not as high as of laser-based systems [11]. This does not necessarily have to be a disadvantage, because the required frequency strongly depends on the application and its demands.

A further disadvantage is that the velocity of sound strongly depends on temperature, wind, pressure and humidity. A possibility to solve this problem is to measure these parameters as good as possible and develop a model to calculate their influence on the velocity of sound as in [45]. Under consideration of this model, the correct signal speed and in further consequence the correct distance can be measured.

4.2 Summary

In this section, an overview about the previously discussed technologies is given and a concluding comparison is done. In general, the methods described before can be classified into four groups:

- **Vision-based systems:** These are single camera systems as well as stereo cameras. Especially stereo cameras have a high potential and give powerful opportunities for obstacle detection. However, the main drawback is that good illumination is highly influential on the correct functionality.

- **Light-based systems:** Light based systems are laser- and infrared-based systems. These systems provide great accuracy (mm-range) as well as a huge measurement range (from a few centimetres up to a few kilometres). On the other hand, poorly reflecting surfaces cannot be detected and the systems do not work in dusty environments due to scattering effects.

  Another disadvantage of light-based as well as vision-based systems is that their optics become filthy in dirty environments over time. To guarantee a maintenance-free drone system, for example an automatic cleaning device would be required in the base station.

- **Acoustic systems:** The properties of sonar systems are quite complementary to those of light-based ones. Their functionality is independent on dust, dirt, fog and the lighting conditions in the measurement area on the one hand. On the other hand, these systems only have a moderate range and the sensors have to point normally to the object surface to guarantee optimal performance. Nevertheless, the sensors as well as their integration in a system are rather inexpensive, which is why ultrasound technology is used to construct a test system in chapter 5.

- **Others:** The structured-light method is, as well as its pros and cons, a mixture out of a vision- and light-based system. On the one hand, the system is, as well as light-based systems, independent of illumination. On the other hand, accuracy is not as good as that of laser- and infrared-systems. The technology also strongly depends on the reflectivity of the detectable object.

Table 4.2.1 gives an overview about the different systems and their relevant characteristics. System properties like accuracy and measurement range are not considered as all systems in the list have acceptable properties. Characteristics indicating the usage in a steel plant are written in green and characteristics speaking against it are written in red. The column "complexity" refers to the complexity of the general measurement setup as well as to the required computational power. The very right column refers to both acoustic and light reflection. Other approaches with single camera systems than OF and SfM are not listed in the table, as the state of development is still extremely low and these approaches currently are not useful in industrial environment.

It can be seen that sonar seems to be the most suitable technology for a reliable and cheap obstacle detection system. The main problem of all other methods is their sensitivity to dust. Nevertheless, laser systems seem to be appropriate as well even though they would be way more expensive, which is not considered in table 4.2.1. Cameras are in general

	complexity	constant lighting required	sensitivity to dirt/dust	realization of 360°-view	state of development	dependence on obstacle reflectance
single camera: OF	very high	yes	very high	difficult	research	no
single camera: SfM	very high	yes	very high	difficult	research	no
stereo camera	high	yes	very high	difficult	well-engineered	no
structured light	high	no	high	difficult	well-engineered	yes
laser: ToF	low	no	high	easy	well-engineered	yes
laser: phase-shift	low	no	high	easy	well-engineered	yes
laser: FMCW	high	no	high	difficult	research	yes
laser: triangulation	high	no	high	easy	well-engineered	yes
infrared	low	no	high	easy	well-engineered	yes
sonar	very low	no	very low	easy	well-engineered	yes

Table 4.2.1: Comparison of different obstacle detection systems. Green marked entries indicate the usage in steel plants, red marked entries speak against it.

very powerful and flexible sensors, however it seems as if there were easier methods for obstacle detection.

As there is no technology available which is perfectly suitable in every respect, a combination of different methods seems to be the best solution. This would allow to use the advantages of one technology for the compensation of another technology's disadvantages.

5 Setup and Evaluation of a Sonar Obstacle Detection System

In chapter 4, useful technologies for the development of an obstacle detection system were discussed from a rather theoretical point of view. In this chapter, an obstacle detection system is developed and its performance is evaluated. The aim is to see the whole issue out of a more practical perspective and to find out the occurring challenges and problems that may not be obvious beforehand.

In sections 5.1 and 5.2, the hardware setup and the sensor controlling software are developed. Sections 5.3 and 5.4 concentrate on the evaluation of measured data.

5.1 Measurement setup

HC-SR04. The ultrasonic ranging module HC-SR04 is used for the measurements. It consists of both a transmitter and receiver and needs a supply voltage of 5 V. With a theoretical ranging distance of 2 - 500 cm and an accuracy of 3 mm, the module exhibits amazingly good values for a low-cost ultrasonic distance sensor [55]. As it can be seen in figure 5.1.1 (b), the module has the four pins "Gnd", "Echo", "Trig" and "Vcc". The measurement is started by setting the trigger-pin high for 10 µs. As soon as the module sends out an ultrasonic pulse, the echo-pin is set high and as soon as an echo pulse is received, the echo-pin goes back to low again.

An important property to be considered during measurement is the field of view of the ranging module. Referring to [55], it has an opening angle of about 30°. In section 5.3 it will be seen that this is a good reference value. However it is not really possible to define an absolute opening angle as the detectability of an object depends on many issues (e.g., size).

Genuino UNO. To control the sensors, a Genuino UNO is used. This is a microcontroller board based on an Atmel Atmega 328. The board is better known under the name Arduino UNO and in fact there is no difference between these two and the reason for the different names is a litigation. The board has 14 digital pins and 6 analog pins and some other peripheral components. It can be connected to a computer and programmed via USB [1].

The opening angle of the ranging module is relevant for the setup. It is obvious that several sensors are needed to guarantee obstacle detection all around a drone. However, when placing the modules side by side it is possible that two neighboured sensors influence each other, which means that one sensor receives an echo of a signal sent from the other sensor and vice versa. One special case in which this phenomena called crosstalk may occur is depicted in figure 5.1.2 (a). In this arrangement, an object is in the field of view of both sensor modules. This means that if one module, e.g., module 1, transmits a signal (T) at time 0, the echo (E) will be received by module 2 as well. The propagation delay

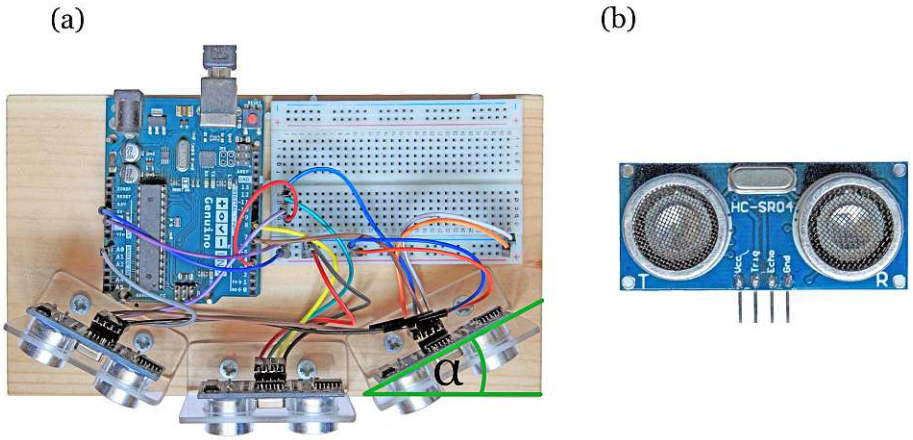

Figure 5.1.1: Measurement setup (a) and HC-SR04 ultrasonic ranging module (b). The sensors are arranged in an angle of $\alpha = 30°$ and controlled by a GENUINO UNO. The ranging module consists of a transmitter (left side) and a receiver (right side). A measurement is triggered with a high-signal on the "Trig"-pin, the signal runtime is received at the "Echo"-pin.

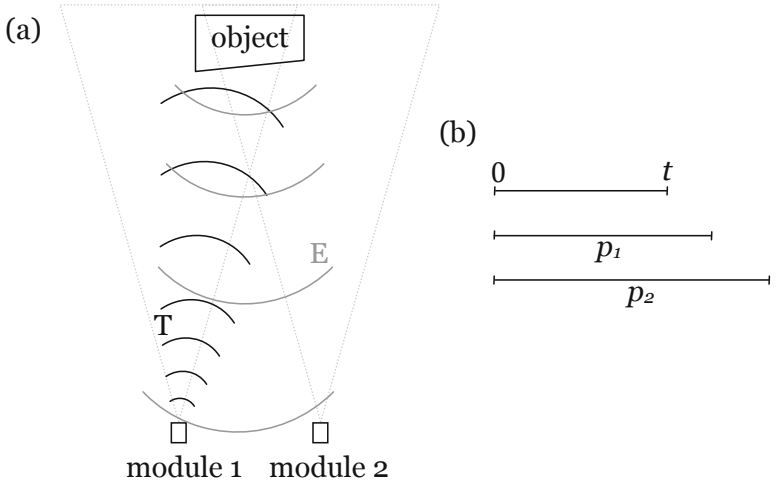

Figure 5.1.2: Crosstalk of two ultrasonic modules with an object in the area of range of both sensors (a) and propagation delay of different signals (b). p_1 is the propagation delay of the signal received by module 1, p_2 is the propagation delay of the signal received by module 2 (b).

of the signal received by module 1 is p_1, the propagation delay of the signal received by module 2 is p_2 (figure 5.1.2 (b)). However, p_1 and p_2 will not differ much, because the two modules are placed side by side with a maximum distance of a few cm. A problem occurs when module 1 sends at time 0, module 2 sends at time t and both receivers detect the reflected signal of module 1. In this case, module 2 would measure the propagation delay of $p_2 - t$ which is way lower than the real propagation delay for module 2 which would be somewhere between p_1 and p_2. The problem can be solved by triggering all modules in the measurement setup simultaneously. The error of the measured propagation delay is reduced to the difference between p_1 and p_2.

Simultaneous triggering will not help if module 2 shall measure the distance to a second object which lies right behind the depicted object in figure 5.1.2 (a). Even if the front object was not within the field of view of module 2, it would be possible that due to its shape some part of the signal from module 1 is received by module 2. Thus, module 2 will not be able to measure the distance to the rear object. The influence of this effect is discussed in section 5.4.

One possible solution to problems like crosstalk is the use of different sonar frequencies for each sensor. However, in this thesis the system is kept as simple as possible, to see whether such a simple system would already provide satisfying performance. The evaluation of a system with multi-frequency sensors would be a good continuation of this issue in the case that the approach of the autonomous UAV is further pursued beyond this work.

In [59] it was shown, that an overlap of the measurement area could improve the resolution, however for testing purposes it is enough to simply maximise the field of view and guarantee that there are no blind angles. In order to ensure that and referring to the opening angle stated above, the ranging modules are arranged in an angle of 30° to each other (figure 5.1.1 (a)). With this setup, an area of 90° is covered, which is sufficient for the dynamic measurements done in section 5.4. However, for the detection of obstacles in a 360°-angle in at least one plane it would be necessary to use 12 HC-SR04 modules.

5.2 Software

To measure distances with the ultrasonic sensors, the sensors are triggered and the distances are calculated out of the signal runtime with a Genuino UNO. The measured data is transmitted to a computer and written into a file for later analysis with Matlab.

Every time a new program is loaded on the Genuino, its control registers have to be set as required. This is done in a special function which is called only once at program start. It sets the pin which triggers the three sensors as an output-pin and three pins which receive the echoes as input-pins. Furthermore, interrupts are enabled for the echo pins. This means that an interrupt service routine (ISR) is executed every time the logical level of a specific input pin changes, independently of the actual program state. Three ISRs are needed for three sensors, however they all look the same (see listing 5.2.1).

```
1 ISR(PCINT2_vect){
2   static unsigned long pulsestart1;
3
4   //if there is a rising edge at echo-pin 1
5   if (digitalRead(echo1)){
```

```
6       pulsestart1 = micros();
7     }
8     else {
9       difference1 = micros() - pulsestart1;
10    }
11  }
```

Listing 5.2.1: Interrupt service routine. The duration of the rectangular pulse at an echo-pin is measured and written into a global variable.

The static variable `pulsestart1` is defined in the ISR. It is defined as static, because its value must not change between two function calls. As stated above, the ISR is called whenever the logical level of the interrupt pin changes. At every rising edge of the pin, the current program runtime in microseconds is stored in `pulsestart1` by calling `micros()`. At a falling edge, the runtime is measured again and `pulsestart1` is subtracted. The result is the length of the echo signal which is stored in the global variable `difference1`.

Every common GENUINO-sketch contains a function called `loop()`. It is called repeatedly and in this case it is used to simultaneously trigger the sensors every 50 ms. Additionally, the distances are calculated out of the time difference measurements done in the ISRs by implementing equation 4.1.2 (listing 5.2.2).

```
1  void loop()
2  {
3    //ensure that trigger pin is low before
4    //trigger event is started
5    digitalWrite(trigger, LOW);
6    delayMicroseconds(3);
7
8    //start trigger event
9    digitalWrite(trigger, HIGH);
10   delayMicroseconds(10);
11   digitalWrite(trigger, LOW);
12
13   //calculate distances out of signal
14   //runtime (in us)
15   differencecm1 = float(difference1)/10000;
16   distance1 = 171.5*differencecm1;
17
18   ...
19
20   delay(50);
21 }
```

Listing 5.2.2: Starting measurement by initiating trigger event and distance calculation by implementing equation 4.1.2. The function is executed every 50 ms.

The measurement result is stored in the global variable `distance1` and should be in the unit of cm. As the time measurement is given in microseconds and the sound velocity in m/s, the divisor of 10000 is required. In the original source code these calculations are

of course performed three times, however to keep the code as clearly as possible they are only listed once here.

The measured distances are sent to a computer via USB. To avoid misinterpretations on the receiving end, they are sent in triples. At first, the distance values of the datatype float are converted to integers. Afterwards, they are packed into the form "**A***distance***B***distance***C***distance***D**" as strings.

```
1  String logData(float distance1, float distance2,
       float distance3)
2  {
3    //cast distances to integers
4    int distanceround1 = int(distance1);
5          ...
6
7    //pack the distances to a triple
8    String package = 'A' + String(distanceround1)
       + 'B' + String(distanceround2) + 'C' +
       String(distanceround3) + 'D';
9
10   return package;
11 }
```

Listing 5.2.3: The measured distances are converted to integers and afterwards packed into a string.

5.3 Static measurement

The aim of the static measurement is to determine the properties of the HC-SR04 more closely. To be more specific, it is examined how well objects of different size can be detected from different distances. Only the middle sensor module of the setup depicted in figure 5.1.1 (a) is used, the other two are disconnected. To be able to do a meaningful measurement, it is necessary to specify the position of an object in the room as good as possible before the measurement. It can be imagined that it is pretty easy to determine the horizontal distance between sensor and object reproducibly. However, determining the relative vertical position is a more challenging task. For this purpose, a net is hung inside a room (figure 5.3.1). The size of the net is $1 \times 1\,\mathrm{m}^2$ with 100 meshes of $10 \times 10\,\mathrm{cm}^2$.

The process of measuring is done as follows: the sensor module is placed exactly in the midpoint of the net at a specific distance m (figure 5.3.1 (a)). The distance n between net and wall is 1.5 m. Afterwards, three measurement cycles are done for each distance. In each run, an object with a certain size made of paper is placed in every possible position (with respect to the mesh size) of the net. It is evaluated whether the object can be detected by the sensor module. The net itself cannot be detected by the ultrasonic sensors as it is non-reflecting for the signals. It can be seen in figure 5.3.1 (b) that the lowest row of meshes doesn't contain a weft. This is intentional, because no weft is needed here to fix an object in the net.

Figure 5.3.2 shows the results of the measurement with an object of the size $50 \times 30\,\mathrm{cm}^2$. The matrices represent the net out of the ultrasonic sensor's view. Thus, each matrix

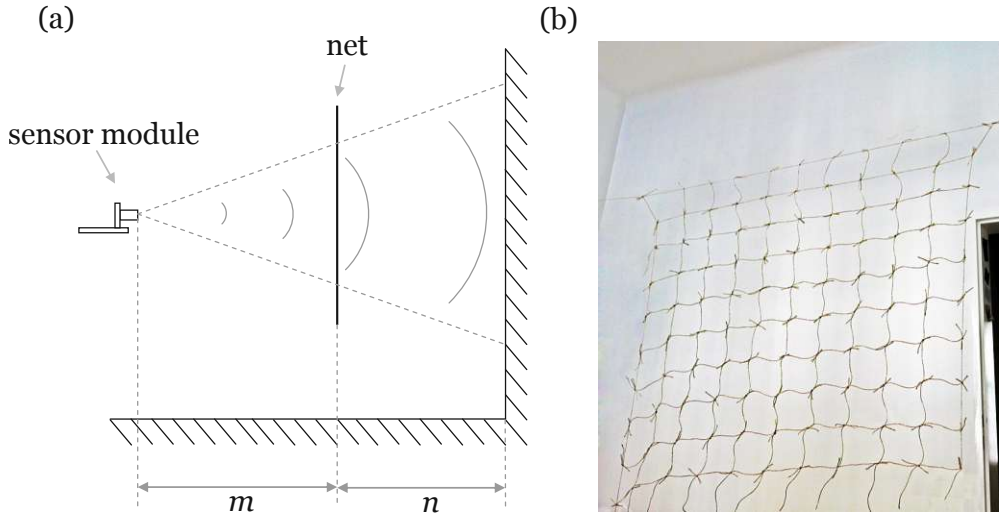

Figure 5.3.1: Arrangement of static measurement (a) and picture of the net (b). The measurements are done with different values for m. The distance n remains constant at 1.5 m. The sensor's field of view is intimated with two dotted lines. The net is non-reflecting for ultrasonic signals.

element in the figure stands for a mesh in the net which means that the object covers an area of 5×3 elements. The six matrices depict the measurement results for different distances m.

The object can be detected by the sensor when it is placed anywhere in the black area. It can be seen that the object can in general be detected better the lower the distance m is. However, this is not a surprising result. More interesting is the fact that the areas of detectability are strongly asymmetric in horizontal direction. For an explanation, another look should be taken at figure 5.1.1 (b). As the sensor is constructed with a separate transmitter and receiver, it doesn't behave symmetrically. The signal is sent out by the transmitter on the right side and therefore it propagates slightly more rightwards. On the other hand, the field of view of the receiver lies a little further leftwards. This property shifts the field of view of the whole sensor module to the left side.

A second issue that may seem strange is that the object cannot even be detected in every possible position in the net at a very short distance of 0.5 m. On the basis of the observations just made it can be concluded that the sensor's field of view is not a cone. However, it must have a certain opening angle as depicted in figure 5.3.1 (a). Considering the measurement arrangement, this means that only a certain part in the middle of the net lies inside the field of view when m is small. When the object is placed in the very upper left corner of the net (where it obviously cannot be detected), its lower right corner lies in the mesh with the x-value 5 and the y-value 3. As a result, this mesh must be at the boundary of the sensor's field of view.

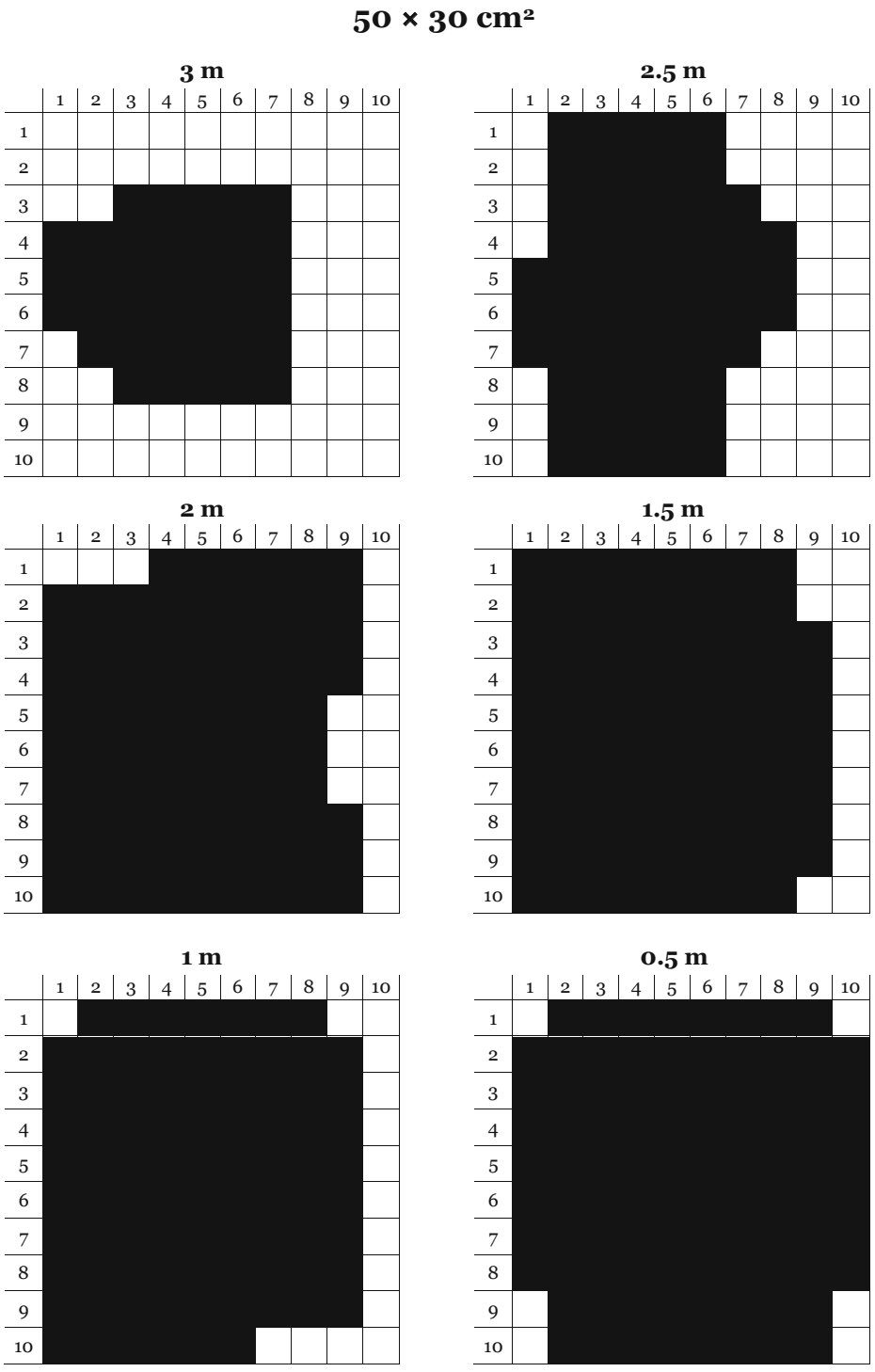

Figure 5.3.2: Measurement results with an object of the size $50 \times 30\,\mathrm{cm}^2$ at different distances m. The object can be detected when it is placed inside the black area.

Figure 5.3.3 shows the measurement results with an object of the size $20 \times 20\,\text{cm}^2$. The object is not detectable from a distance of 3 m. As with the bigger object in the previously described measuring cycle, the asymmetry of the field of view can be seen here as well. The influence of the distance can also be observed very well. At a distance of 2.5 m the detectable area is $30 \times 30\,\text{cm}^2$. At 0.5 m it is only slightly larger and the maximum area occurs at 2 m. Again, this can be explained with the sensor's field of view. It seems as if the net was covered best at a distance m of approximately 2 m. For bigger values of m, the sensor module "sees" an area which is bigger than the net and therefore it is more difficult to detect small objects. The reason is that the relation between field of view at distance m and object area grows with the distance (as the field of view grows with the distance). For smaller values of m, the sensor module can only "see" a certain area of the net and objects outside this area cannot be detected. Together with some additional features of this measuring cycle, this observation can be used to verify the specification of the sensor module's opening angle given in [55].

It is most likely that the detectable areas at distances of 0.5 m respectively 1 m correspond to the field of view at these two distances. The reason why the black areas in the other three matrices cannot be directly associated with the module's field of view again is the growing relation between field of view and object. E.g., in a field of view with a diameter of 1 m, a $0.04\,\text{m}^2$-object only covers 4 % of the total area. As a result, it cannot be detected in every possible position in the field of view any more. On the other hand, if the field of view is for example only twice as big as the object's area, the object is comparatively big and will be detected everywhere in the sensor's field of view. Thus, the detectable area directly corresponds to the field of view. The opening angle is estimated with the following three observations:

- Due to the maximum detectable area it can be assumed that the area of the net matches best with the sensor's field of view at a distance of 2 m. Assuming a right triangle with an adjacent side of 2 m and an opposite side of 0.5 m (for better understanding also see figure 5.3.1 (a)), both the horizontal and vertical opening angles result in $2 \cdot \arctan(\frac{0.5}{2}) = 28.07°$.
- At a distance of 1 m to the net, the field of view covers an area of approximately $40 \times 50\,\text{cm}^2$. This implies an opening angle of $2 \cdot \arctan(\frac{0.2}{1}) = 22.62°$ in horizontal and $2 \cdot \arctan(\frac{0.25}{1}) = 28.07°$ in vertical direction.
- At a distance of 0.5 m, the covered area is $30 \times 40\,\text{cm}^2$. The same calculation leads to a horizontal angle of 33.4° and a vertical angle of 43.6°.

The big vertical opening angle at 0.5 m can be derived from the measurement resolution. Even if the field of view was only $30 \times 30\,\text{cm}^2$ with its upper left corner at the x- and y-positions (4/4), the lower half of an object placed in the very upper left corner of the black area would be inside the field of view and could be detected. In other words, the black area corresponds to the field of view with an inaccuracy of ± 1 mesh. However, all in all the specification of an opening angle of 30° in [55] is a quite satisfying approximation.

The third measurement cycle is carried out with an obstacle of the size $10 \times 10\,\text{cm}^2$. The obstacle could not be detected from a distance of more than 2 m, which is why only four different distances are depicted in figure 5.3.4. In contrast to the two previous measuring cycles, this one doesn't show a significant asymmetry. The edges to the left and right side

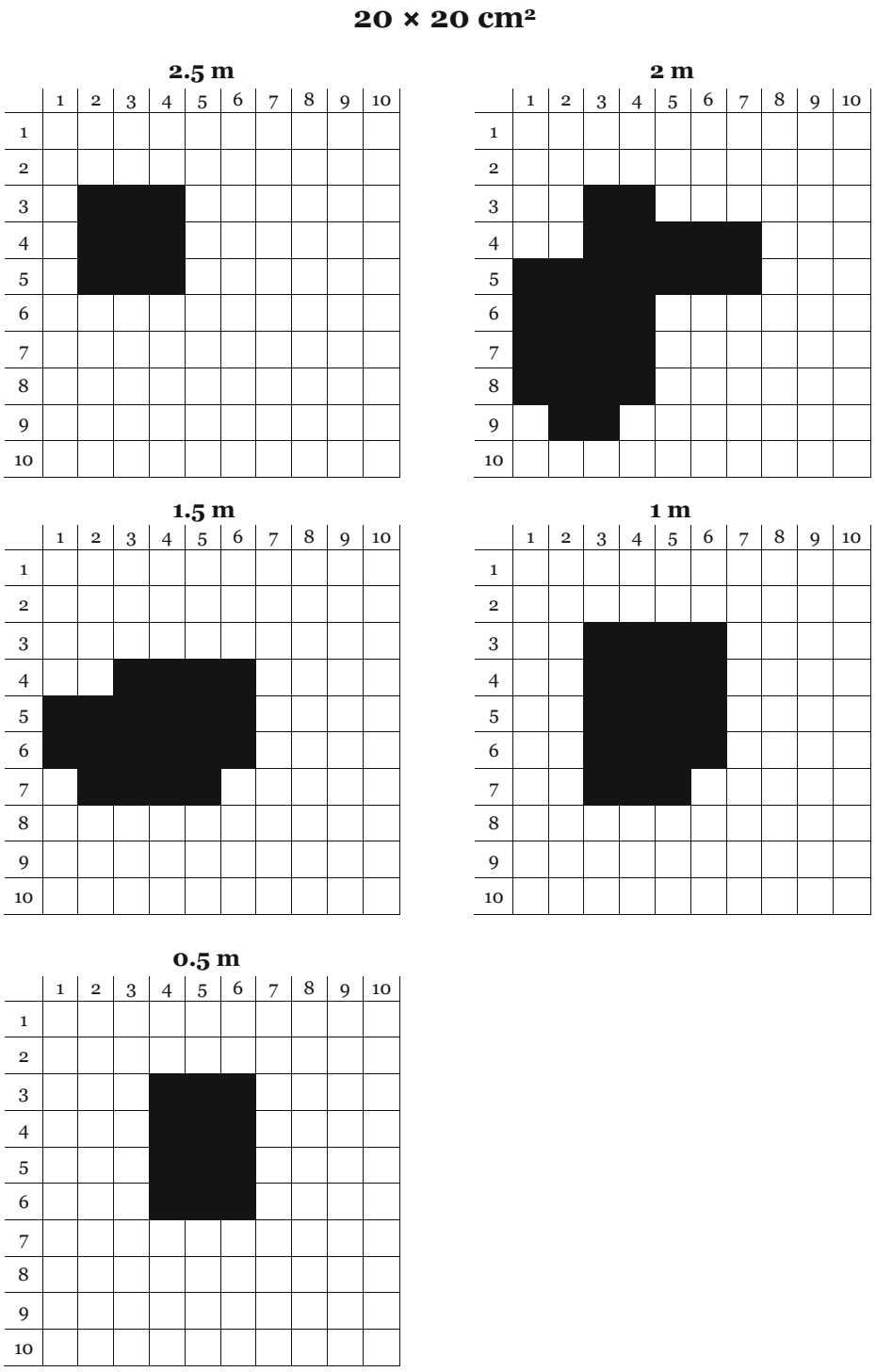

Figure 5.3.3: Measurement results with an object of the size $20 \times 20\,\mathrm{cm}^2$ at different distances. The object can be detected when it is placed inside the black area.

of the black areas are of the same width. The reason most likely is that there are not enough positions where the object was detected to determine this issue.

In general it can be seen that such small objects cannot be detected sufficiently. The best result is reached at a distance of 1.5 m where the object can be detected at 6 out of 100 possible positions.

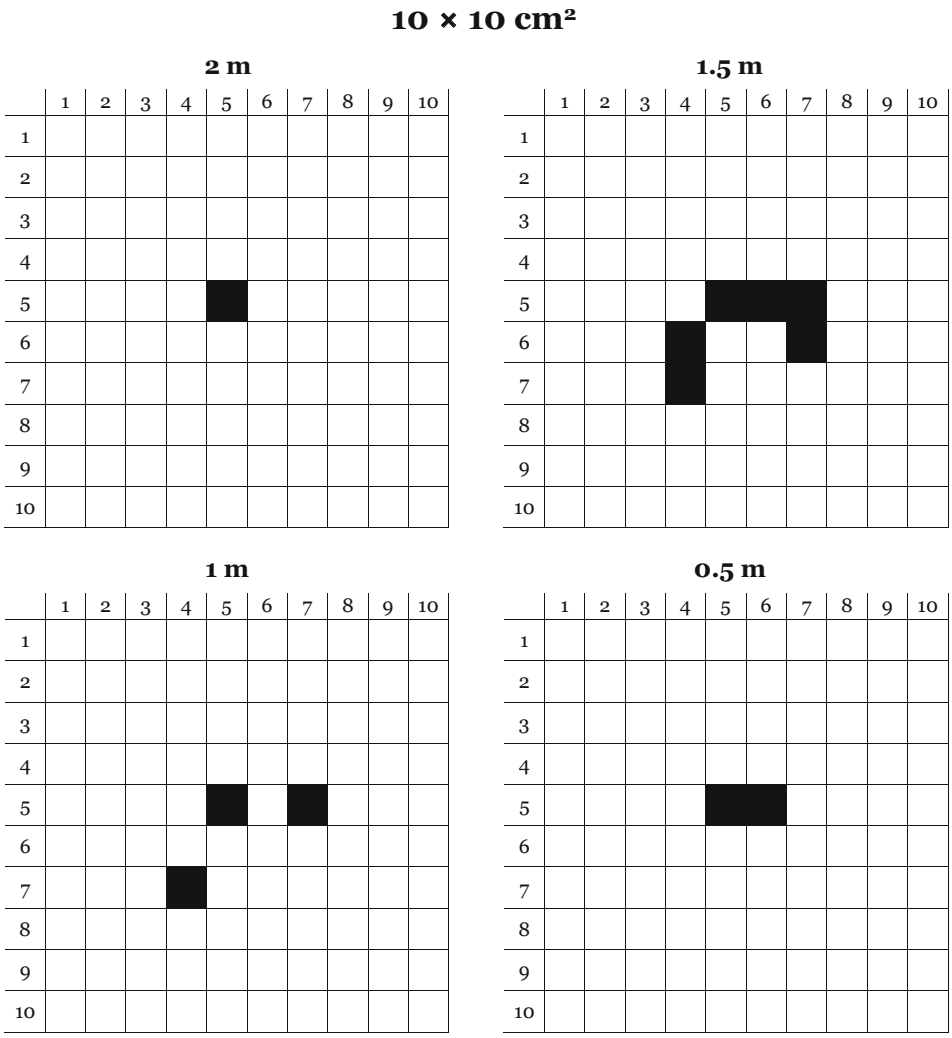

Figure 5.3.4: Measurement results with an object of the size $10 \times 10\,\mathrm{cm}^2$ at different distances. The object can be detected when it is placed inside the black area.

Summing up, it can be said that the equipment used here is definitely not suitable to construct an obstacle detection system for a UAV which should be conform to industrial safety standards. Especially the detection of relatively small objects is not satisfying as there are too many holes in the area in which the object can be detected. Nevertheless it should be considered that this is not the result of ultrasonic technology in general but

the result of a test with one specific low-cost sensor. There are many different ultrasonic distance sensors promising way better performance, better directivity etc. available on the market. Thus, for an implementation of the system on a drone, it is advisable to use industrial-suited ultrasonic sensors.

5.4 Dynamic measurement

5.4.1 Lateral movement

To evaluate the performance of the measurement setup with respect to obstacle detection during the UAV's flight, the three sensor modules are moved parallel to a wall with differently shaped obstacles in front of it. With a well-performing system, the surface of the wall and the obstacles should be identifiable in the resulting signal curve. The measurements are done with two different scenarios:

- **Scenario 1** consists of 6 obstacles distributed in front of a wall with a width of 3.66 m. The obstacles are enumerated as depicted in figures 5.4.1 and 5.4.2. Some obstacles are difficult to detect because of their shape (slim, sloping surface towards the sensor). The measurements are done with the three sensors as depicted in figure 5.1.1 (a) as well as with one single sensor. One aim is to determine the influence of crosstalk discussed in section 5.1.

- **Scenario 2** is simpler as it consists of only three obstacles distributed in front of the same wall. The sensor modules are moved in an oblique angle of 30° to the wall (imitating an oblique position of the multicopter) to determine whether such a measurement will deliver useful results (figure 5.4.3).

Figure 5.4.4 depicts the measurement results of scenario 1 with three sensor modules M1, M2 and M3. The three diagrams show the measured distances between sensor module and obstacle or wall. The bottom diagram shows the arrangement of the 6 obstacles out of a worm's eye view with the wall represented by the ordinate value of zero. The abscissas of all three diagrams are equal and represent the positions of the sensors respectively the obstacles along the wall. Sensor module M3 is the first one in direction of movement, M2 is the middle sensor and M1 is the rearmost sensor in direction of movement. This can also be seen in the diagrams as M3 always is the first sensor to detect the presence or absence of an obstacle. In general a decline in the signal indicates the presence of an obstacle. Due to the opening angle of the measurement area of each sensor, the decline in the signal is always broader than the obstacle itself (the obstacle is already detected before the sensor is straight in front of it). Several further remarkable characteristics can be discovered in the figure. First, it is obviously difficult to detect obstacles 4 and 6 which are rather slim (approx. 5 cm) as well as obstacle 3 which has a surface that is not normal to the ultrasonic signal. Neither of the three sensors is able to detect them in a satisfying way. Interestingly, obstacle 2 can be identified in all three signal curves (the corresponding decrease is marked with the blue circles in figure 5.4.4). If the signal of one sensor, e.g. M2, was used to detect an obstacle simply by setting a specific signal threshold and without any other post-processing, at least obstacles 1, 2 and 5 could have been detected, as shown with the red line in figure 5.4.4.

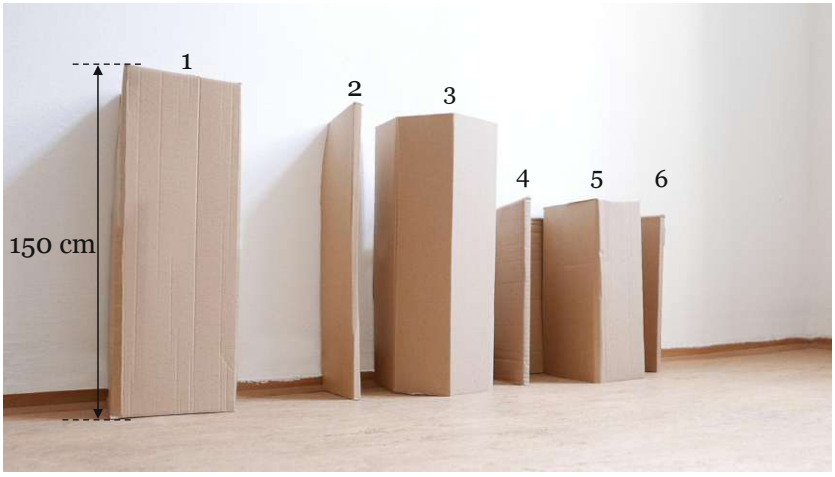

Figure 5.4.1: Cardboard boxes are fixed along a wall as obstacles for the sonar measurement (this figure shows scenario 1). There is some space left between the boxes and the side wall of the room to avoid undesired reflections.

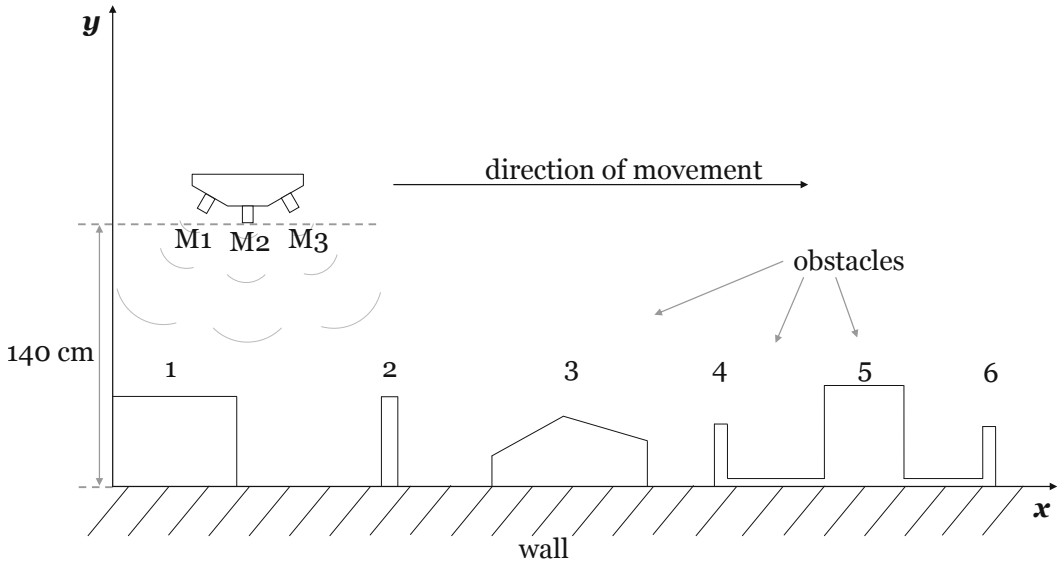

Figure 5.4.2: Scenario 1. The arrangement of the obstacles is depicted along the x-axis. The sensor modules are denoted with M1, M2 and M3 and moved in x-direction.

Figure 5.4.5 shows the measurement of scenario 1 with a single sensor module. The meaning of the axes is the same as in the previous figure. It can be clearly seen that the result with one sensor is way better than with three sensors. All 6 obstacles can be recovered in the signal. Furthermore, accuracy is astonishingly good. This can be seen

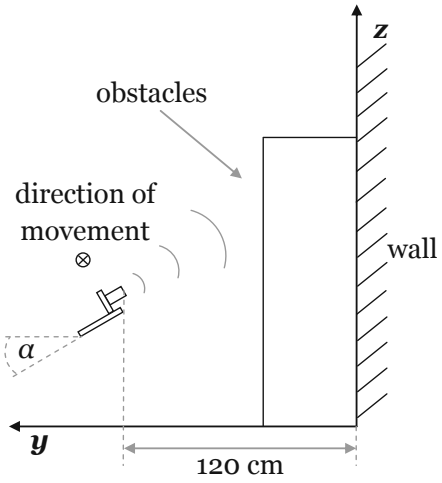

Figure 5.4.3: Side view of scenario 2. The sensor modules are again moved in x-direction, however they are tilted by $\alpha = 30°$. For the sake of simplicity, only one module is depicted in this figure.

especially with obstacles 2, 3 and 4. Obstacle 2 protrudes from the wall about 6 cm more than the tip of obstacle 3 and the tip of obstacle 3 protrudes about 7 cm more from the wall than obstacle 4. These properties can be clearly seen in the declines of the signal, although obstacles 2 to 4 are the most difficult ones to detect. The only weakness of this measurement system is that obstacle 3 is not detected at its complete width. As mentioned above, usually the signal decline is broader than the width of the obstacle because of the sensor module's opening angle. However, the decline due to obstacle 3 is narrower than the obstacle itself.

In the third measurement it should be determined how the sensors behave when they are in an oblique angle to the wall (figure 5.4.3). This situation occurs whenever a drone accelerates and thus is not aligned horizontally. The distance between sensors and wall is less than in scenario 1. This is to obtain the distance of about 140 cm to the wall in the main direction of the signal ($\frac{120\,\text{cm}}{\cos(30°)} \approx 140\,\text{cm}$). A different scenario with "easier" obstacles is used here so that the disturbances due to difficultly detectable obstacles described above are minimised. This enables to completely focus on the influence of the sensor orientation. In the case of an oblique sensor only a small part of the ultrasonic signal is reflected back to the sensor, as the main part goes anywhere else. The sensor might not be able to detect the reflected signal and delivers an invalid value. In case of the HC-SR04 this is a value out of the sensor's range. As a result, the measured signal has a significant amount of outliers. However, they can be filtered out easily in a post-processing step in MATLAB. The filtered result can be seen in figure 5.4.6. One interesting aspect is the irregularity of the signal of M3 and M1 between 0 and 50 cm. It occurs because the transmitted signal is not reflected by the obstacle but by the ceiling (for a better understanding see figure 5.4.3). The resulting distance lies between 170 and 200 cm. The second remarkable signal property are the variations in the signal of M2 and M1 between 60 and 150 cm. As it is not possible to give an explanation of this issue a priori, further experiments are performed in section 5.4.2. Regardless of all variations, especially the signal of module M2 matches

astonishingly well with the arrangement of the obstacles.

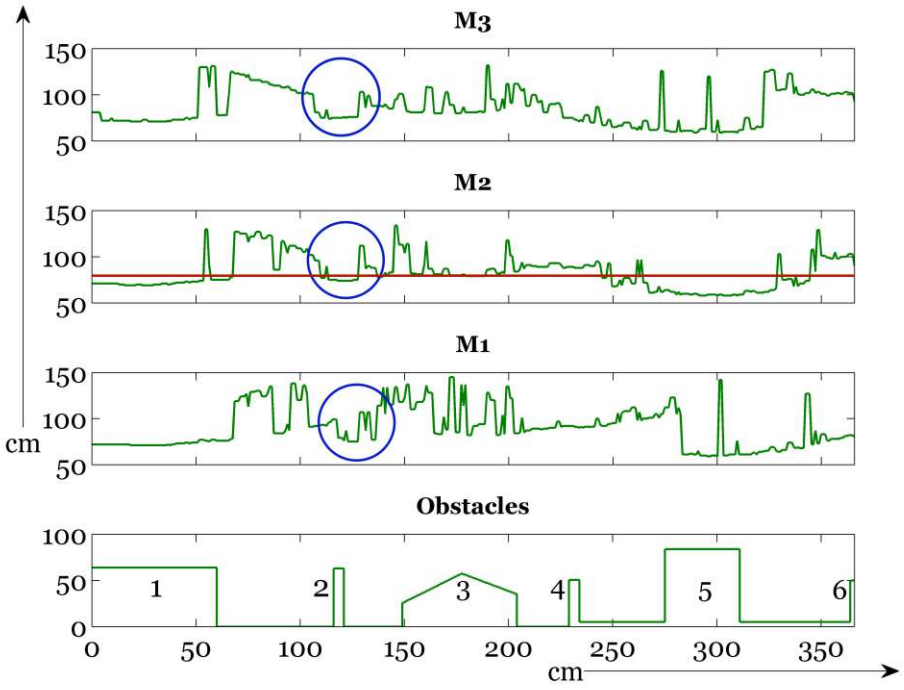

Figure 5.4.4: Sonar measurement of scenario 1 with 3 modules. The bottom diagram shows the obstacles out of a worm's eye view; M1, M2 and M3 are the measured signals.

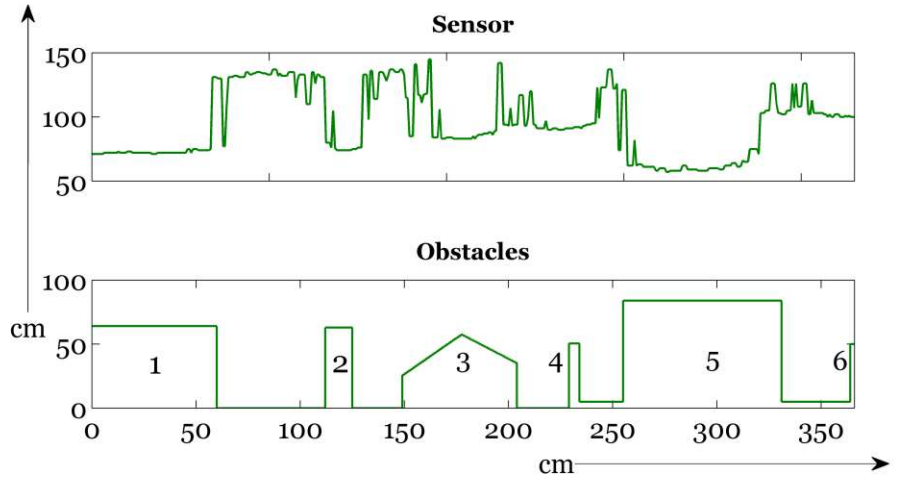

Figure 5.4.5: Sonar measurement of scenario 1 with module M2 only. The bottom diagram shows the obstacles out of a worm's eye view; the upper diagram shows the measured signal.

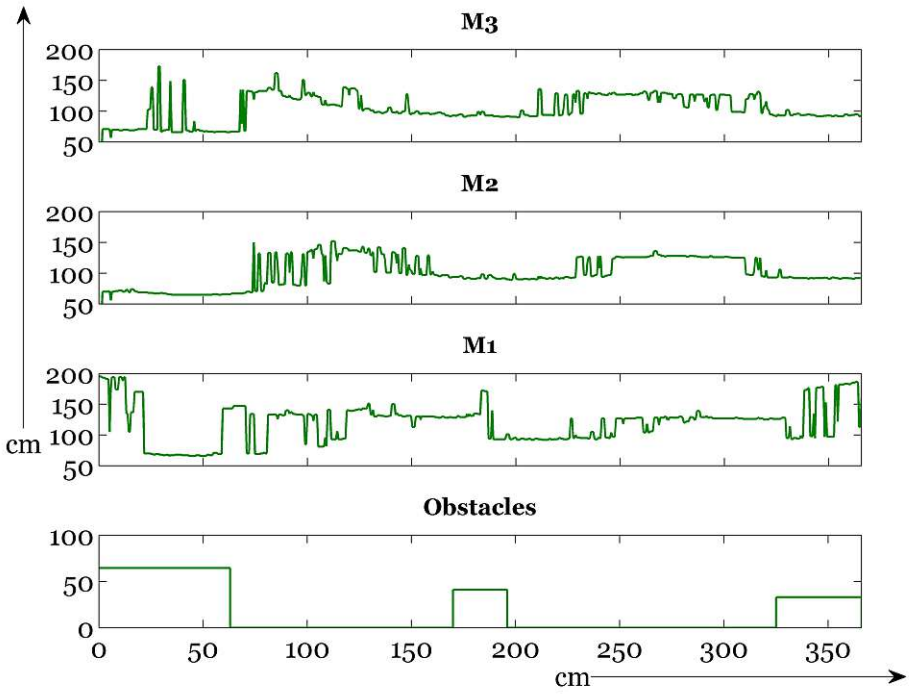

Figure 5.4.6: Sonar measurement of scenario 2 with 3 modules at an angle of 40° to the wall. The bottom diagram shows the obstacles out of a worm's eye view; M1, M2 and M3 are the measured signals.

5.4.2 Rotational movement

To find out the reason for the signal variations occurring in the measurement of scenario 2 in section 5.4.1, the angular dependence of the measurement setup is examined in this section. The arrangement is shown in figure 5.4.7. All three sensor modules (see figure 5.1.1) are used for this measurement. They are positioned inside a room as shown in figure 5.4.7. In its starting position, the modules point towards the wall ($\alpha = 0°$) and during the measurement they are rotated by 90° until they point normally towards the ceiling.

Similar to the measurement of scenario 2 in section 5.4.1, there are many outliers in the originally measured signal. As they would make any analysis impossible, they are removed during the signal post-processing phase in MATLAB. The resulting signals are shown in 5.4.8.

The distance of the sensor modules M1 and M3 to the side wall are 2.5 respectively 2 m. Thus, the two modules show a different behaviour than M2, which delivers the relevant signal for the analysis, because they receive echoes from the side walls. It can be seen that the modules measure primarily three different distances. The first distance is measured between 0 and 40° and represents the distance of the sensor towards the wall (120 cm). At about 40°, variations occur in the signal until it jumps to approximately 220 cm which is the distance of the sensor to the corner between wall and ceiling. At 65° the variations occur again and in the end the signal settles down at 180 cm which is the distance to the ceiling. When assuming a vertical opening angle of 30°, the sensor's field of view reaches

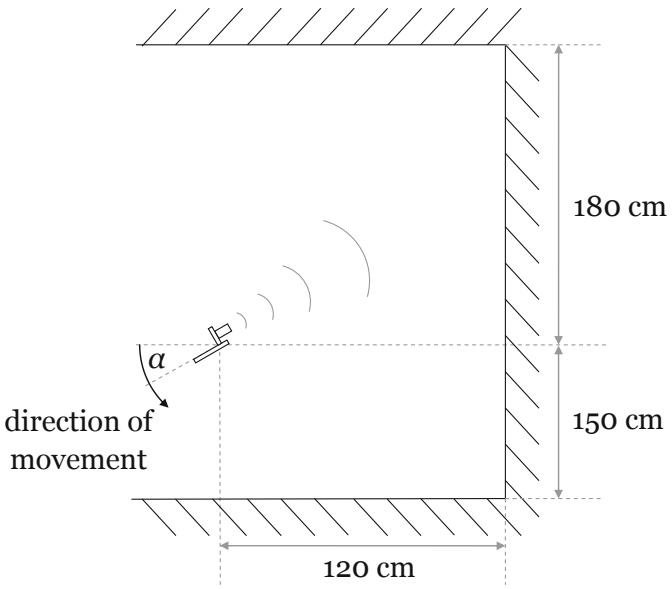

Figure 5.4.7: Arrangement to measure angular dependence. The sensor modules point towards the wall ($\alpha = 0$) at the beginning and are rotated by 90°.

the corner between wall and ceiling at an angle of

$$\alpha = \arctan\left(\frac{180}{120}\right) - 15° = 41.3°.$$

At the same angle, the measured signal starts to vary strongly for a few degrees of rotation. Hence, it is most likely that the corner between ceiling and wall is the reason for the occurring signal variations. The field of view leaves the corner area at an angle of $\alpha = 71.3°$, however the signal variations occur until an angle of about 77°. This is not necessarily a contradiction to the assumption just made as it was shown before that the opening angle of 30° is only an approximation.

As mentioned before, the side wall of the room is in the field of view of M1 and M3. Thus, also the corners between the front wall and the side walls are in their field of view. This explains why the variations occur at different angles in the corresponding signals compared to M2.

Another signal property which cannot be interpreted intuitively is the drop in all three signals at 47°. It may not be precluded that the reason is a strong reflection caused by some constructive signal interference. However, as the signal occurs absolutely simultaneously in all three signals it is more likely that it is caused by a short voltage drop in the power supply voltage of the ARDUINO.

It is especially noticeable that the shape of the signals is widely rectangular. It can be assumed that this is not related to any reflection characteristics of ultrasonic signals but to characteristics of the sensor itself, especially the sensor's internal signal processing. As the HC-SR04 is a low-cost sensor which is not intended to be used for industrial applications, no detailed data sheet is available. As a result, it would be very difficult to make further inquiries in this concern.

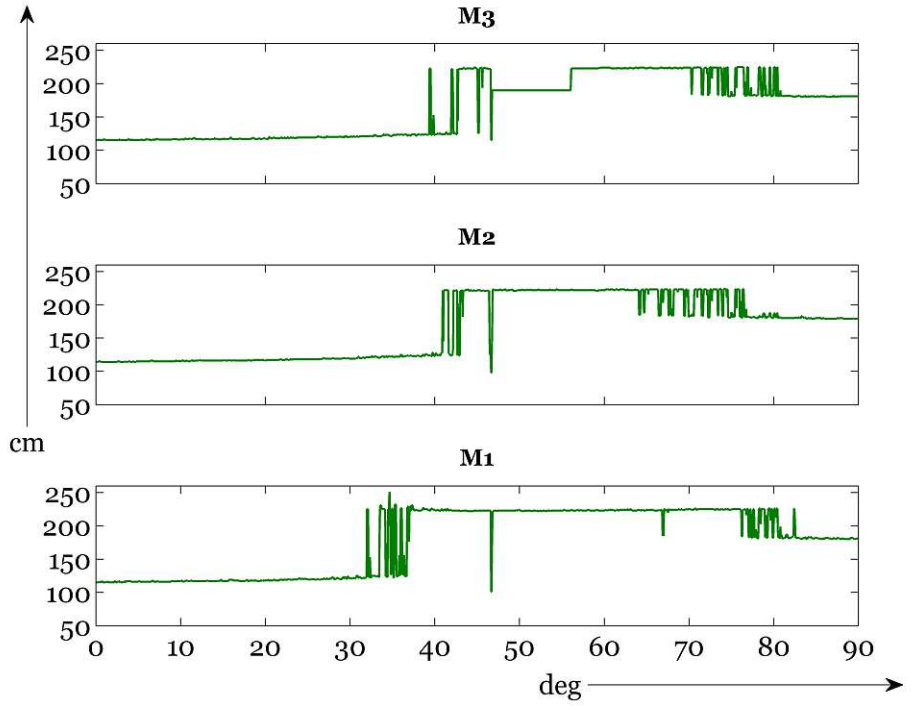

Figure 5.4.8: Measurement results for rotational movement of the ultrasonic sensor setup. The designation of the signal curves is equal to section 5.4.1.

6 Positioning and Navigation

The second big technical challenge in the automation of a drone in a steel plant is navigation. Widely used and established navigation systems are GNSS (global navigation satellite systems) with the best known GPS (global positioning system). These systems are based on the reception of signals from satellites which allow to determine the current position. However, GNSS do not work indoors. The reason is that GNSS signals are attenuated from roofs and walls by 20 - 30 dB (factor of 100 - 1000) [68]. As a result, it is necessary to look for alternatives here.

In general, indoor positioning systems (IPS) are much more difficult to implement than GNSS. This has several reasons. Firstly, higher precision is required. GNSS typically have a nominal accuracy of 15 meters. This is enough for many outdoor applications but it is clear that higher accuracy is needed indoors. Secondly, indoor environments and especially steel plants are rather complex. There are different objects, walls and people which may reflect or scatter the signal used. Furthermore, obstacles in a room lead to the fact that there is no line of sight between the emitter and receiver of a signal, which makes the matter more complex than GNSS too. Thirdly, indoor environment changes more quickly than outdoor environment. Moving people and objects might be a problem when reference points are used for navigation, because these points could either change their position or become invisible for a certain time which would inevitably lead to malfunction of the system.

However, there are some advantages of IPS compared to GNSS as well. Objects generally move slowlier indoors than outdoors. Furthermore, many characteristics of an indoor environment do not change (e.g., doors, corridors) and could be used for navigation [104] [23].

The following section looks at different IPS and their advantages and disadvantages for the usage in a steel plant. At the end of the section, an overview is given similar to section 4.2.

6.1 Available systems

6.1.1 Dead reckoning

Dead reckoning is a navigation technology which takes the latest known position of an object and calculates the actual position out of several additional information like speed and direction of movement. The main principle is depicted in figure 6.1.1. P_0 to P_N are the positions at time t_0 to t_N. The x- and y-value of an arbitrary position P_n can be calculated with the following equation (assuming that P_{n-1} is the latest known position):

$$\begin{pmatrix} x_n \\ y_n \end{pmatrix} = \begin{pmatrix} x_{n-1} + S_n \cdot \sin(\varphi_n) \\ y_{n-1} + S_n \cdot \cos(\varphi_n) \end{pmatrix} \tag{6.1.1}$$

The main problem with dead reckoning is that there is an unavoidable cumulative error, i.e., the errors of each step are added.

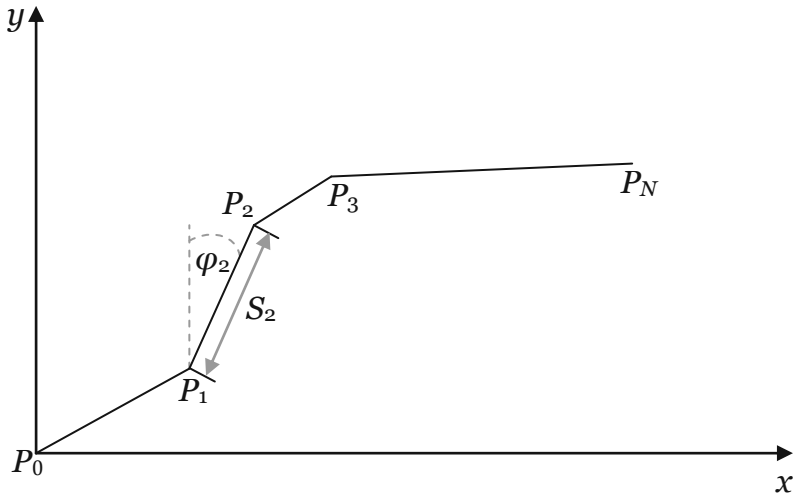

Figure 6.1.1: Principle of dead reckoning. The position P_N of an object can be calculated out of P_{N-1} and additional information like speed and direction of movement. Adapted from [103].

When using dead reckoning, a way must be found to gain information about speed and direction. So-called inertial measurement units (IMU) are the most widely applied technology for this purpose. An IMU consists of accelerometers to measure acceleration in all three dimensions. Furthermore it contains one or more gyroscopes to measure the accelerometers' orientation along the x-, y- and z-axis of a Cartesian coordinate system. This is necessary to be able to subtract gravity of the measured accelerations. To gain the position out of acceleration, it is integrated twice. Hence, the measurement errors are integrated twice as well and therefore quadratically grow with time. An example for the impact of this issue on accuracy is given later. Beforehand, the most important measuring errors must be known and understood.

- **Noise.** As for every sensor, noise is present in the measured signals of gyroscopes and accelerometers. There are many reasons for the occurrence of noise which will not be discussed in detail here. However, noise (often also called random walk) is not a specific problem and a lot of (mainly statistical) techniques exist to reduce this influence and improve signal quality.

- **Timing error.** The measured acceleration is integrated twice over time to get the position. When a complete IMU including a processing unit to perform the integration is considered, it is necessary that the time measured by the system is equal to the global time. Otherwise, the integration would deliver a wrong value. To minimise this error, it is required to measure time with high accuracy.

- **Temperature error.** The precondition to measure the accelerometers' orienta-

tion with the gyroscopes is the knowledge of the relative position between them. However, temperature changes lead to deformation and this precondition may not necessarily be fulfilled any more. Temperature errors are a big issue in MEMS (micro electro-mechanical systems) IMUs. Nevertheless, even for highly accurate light-based gyroscopes like ring laser gyroscopes, the optical length changes when the device is physically deformed and therefore accuracy decreases.

- **Bias error.** Bias errors may be the most affecting errors occurring in IMUs. The reason for bias errors is a mixture of the errors described above together with calibration errors or weak alignment of the sensors. For a gyroscope, the bias error or bias instability is represented in °/hour. It has a range from about 1000 °/h for low cost MEMS gyroscopes for consumer electronics down to about 0.0001 °/h for expensive ring laser gyroscopes [4]. There is a strong connection between the bias error of a gyroscope and an accelerometer [102] [16]. If the exact orientation of an accelerometer was known, it would be easy to get rid of the influence of gravity on the measurement. It could simply be achieved by subtracting the particular amount of the acceleration of gravity ($9.81\,\mathrm{m/s^2}$) from the measured accelerations in each direction. However, when the gyroscope measures with an error of, e.g., 0.1°, this leads to an error of $9.81\,\mathrm{m/s^2} \cdot \sin(0.1°) = 0.017\,\mathrm{m/s^2}$ [9].

To find out the consequences of these errors with respect to a navigation system of an autonomous drone, typical drifts of the measured position of dead reckoning systems caused by a low cost MEMS gyroscope on the one hand and a high-end ring laser gyroscope on the other hand are compared in table 6.1.1. The point in time considered is 15 minutes after the last calibration of the gyroscopes. The acceleration of gravity is considered to be constant over time and therefore the integration can be performed by a simple multiplication with squared time.

	bias error 15 min	acceleration error	drift after 1 s	drift after 60 s	drift after 10 min
low-cost	250°	$9.22\,\mathrm{m/s^2}$	9.22 m	33186.2 m	3318 km
high-end	0.000025°	$0.0000042\,\mathrm{m/s^2}$	4.2 µm	1.54 cm	1.54 m

Table 6.1.1: Drifts of a low-cost and high-end dead reckoning system. The error is growing quadratically with time.

It should be considered that this assessment doesn't take into account the measurement error of the accelerometers, which as well grows quadratically with integration time.

It is definitely not possible to solely use dead reckoning as an IPS. Even advanced mathematical algorithms applying Kalman filters and quaternions do not lead to satisfying results [81]. However, dead reckoning is often used in combination with other technologies which work with low frequencies of only a few Hz. In this case, dead reckoning can be used to bridge the time where no positioning information is available. Every time the main navigation system delivers a new position, the IMU can be re-calibrated based on this information and measures the position for a short time before it is re-calibrated again. In [33] an UWB-system was combined with a low-cost IMU to construct a navigation system with a resolution of about 15 cm.

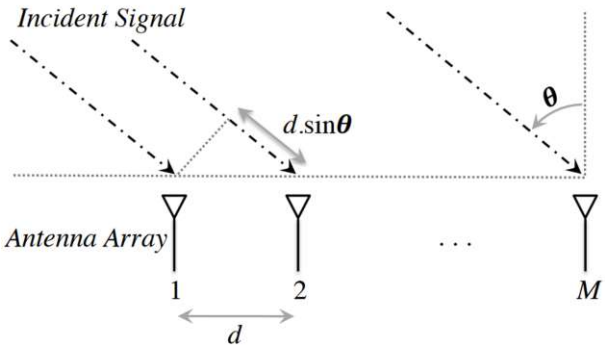

Figure 6.1.2: Principle of the MUSIC algorithm. When the distance d between the antennas in the array is known, the angle of incidence of a received signal can be calculated out of different arrival times of the signal at the single antennas [62].

6.1.2 UWB

Positioning and navigation based on UWB (ultra wide band) signals is one of the most promising technologies. Per definition, the bandwidth of an UWB wave exceeds 500 MHz. The European Communications Committee (ECC) restricted the frequency of UWB to a band between 6.0 GHz to 8.5 GHz. In America, the allowed frequency band lies between 3.1 GHz and 10.6 GHz. This should prevent that UWB signals can interfere with other wireless technologies as WLAN (2.4 GHz). Furthermore, the maximum equivalent isotropically radiated power density is restricted to -41.3 dBm/Hz in America and -53.3 dBm/Hz in Europe. This should primarily minimise the signal's harmfulness to human bodies and also reduce interference. For communication purposes, this issue not a disadvantage as a large amount of data can be transmitted due to the high bandwidth and not due to power. On the other hand, UWB waves can thereby be used for positioning in a maximum range of only about 100 m, which is sufficient for many indoor applications. A big advantage of UWB compared to light- or sound-based systems is that LoS (line of sight) is in general not required. Especially the lower frequency parts of the signal can penetrate wood, but even concrete and glass [69]. The following passage will concentrate on the different ways how UWB waves can be used for indoor positioning. The methods described are not only applicable to UWB waves but also to other technologies which will be discussed in sections 6.1.3 to 6.1.7.

Angle of Arrival (AoA)

In an AoA arrangement, the receiver antennas can detect the angle of the incoming wave. When considering for example two receiver antennas (minimum number required for 2D positioning), the position of a transmitter can be found easily by drawing a virtual angle line for each antenna and intersecting these two lines. This seems to be quite simple, however the more difficult issue is to get the angle of incidence of the UWB signal. An often used method is the so-called MUSIC (Multiple Signal Classification) algorithm in combination with an antenna array. The principle is depicted in figure 6.1.2. Each receiver antenna actually is an array of antennas with known distances. The angle of arrival can be calculated out of the different arrival times of the signal at the different antennas.

In general, the functionality of AoA methods depends on many factors. The antennas in the array have to be perfectly aligned. This is related to a temperature dependency, as the distance between the antennas may change due to thermal expansion. Furthermore, exact time measurement is required which also increases the overall complexity of the system. Another disadvantages is that expensive antenna arrays with large dimensions are required [23].

Time of Arrival (ToA)

Similarly to AoA, a transmitter sends out a signal which is received by at least three receiver stations (for a 2D application). The receivers have to be synchronized with the transmitter. Due to different distances, the receivers measure different runtimes of the signal. These runtimes are used to specify the correct position of the transmitter. The situation can be imagined by drawing circles around the receiver stations with the circles' radii representing the runtime. The intersection of all three circles encloses the area where the transmitter is located. In an ideal case, the circles intersect in a single point. This method is more robust than AoA, however the challenge is the synchronization of all units in the system [97].

Time Difference of Arrival (TDoA)

ToA and TDoA are quite similar methods, nevertheless there is a significant difference and therefore they should not be mixed up. The basic setup is the same: a transmitter transmits a signal which is received by three or more receivers. In contrast to ToA, TDoA doesn't use the runtime but the time difference of the incoming signals at the receiver stations. This has the big advantage that only the receivers have to be synchronized, which is in so far easier as they are stationary [97]. However, the overall accuracy is in general lower than that of a ToA system with the same geometry [23].

Received Signal Strength (RSS)

This method does not require any time measurements as the distances of the transmitter to the receivers is calculated out of the received signal power. One drawback is that it is very difficult to measure with satisfying resolution, as the the RSS strongly depends on multipath interference. Furthermore, the attenuation of radio signals is material-dependent. This means that obstacles and walls have negative effects on the resolution as well [23].

Usually, UWB-based positioning systems combine different methods described above to calculate distance information, which allows to use the advantages of each single method. Despite of the methods to calculate distance information, the general setup of the positioning system can be varied as well. Until now, only so-called direct ranging was considered. This means that a mobile transmitter sends radio signals to stationary receivers. Another approach is passive localisation or UWB-radar. In this case, both transmitter and receiver are stationary and the object to be tracked is reflecting. A further interesting approach is UWB fingerprinting. Here, the space where positioning should be done is divided into a two- or three-dimensional grid. A fingerprint, i.e., a specific signal runtime or signal strength is attached to each mesh of the grid in an offline training phase. The position can be determined by simply matching a fingerprint to the properties of the currently received

signal [69]. Both resolution of the system and effort of the training phase grow with smaller mesh size. For this reason, the approach is not very useful for big areas. Furthermore it cannot be used in a steel plant where the environment is changing constantly.

As it is a promising technology, currently a lot of research is done on UWB positioning systems. However, there are already some marked-ready products available. The most popular one is the Ubisense RTLS which promises an accuracy of 15 cm, although it depends on the environmental characteristics [17]. In [71], the system was tested in an underground tunnel and it was found that under these adverse geometrical site conditions the accuracy decreases to about 1 m. Another commercially available system is the Decawave DWM 1000. An accuracy of even 10 cm for indoor use is promised [15].

6.1.3 Further RF-technologies

Radio Frequency Identification (RFID)

RFID systems consist of two main components: readers and tags. RFID tags emit radio signals which carry a code to identify the specific tag. A tag includes a microchip to store the identification code and an antenna. A reader consists at least of a processor to decode the received signal and of course an antenna. Usually, RFID systems can be classified into two types.

- **Passive RFID.** In passive RFID systems, the tags do not have an own power supply. They can use the radio waves of a nearby RFID reader as an energy source. This energy is sufficient to send their identification code. A big advantage of passive RFID systems is that the tags are very robust and do not need maintenance. Thus, they could also be integrated in areas where they are not reachable, as for example in the concrete of walls. However, the main drawback of passive RFID is the low range because of the small amount of available energy. To be more specific, typical ranges lie between 1 and 2 meters [69].

- **Active RFID.** In active RFID systems, tags are active transmitters with an internal battery. This leads to higher investment cost for tags as well as necessary maintenance because the battery has to be changed from time to time. On the other hand, ranges of up to 100 m can be achieved [69].

Due to the low range, passive RFID is not useful for IPS.

The most commonly used method in positioning systems based on active RFID is RSS (see section 6.1.2). In general, the accuracy of an RFID-based IPS strongly depends on the number of tags and readers used. In [52], the position of one tag a cuboid room with the dimensions $5.13\,\text{m} \times 4.5\,\text{m} \times 2\,\text{m}$ could be measured with an accuracy of 5 cm. For this experiment, 8 RFID readers were used.

WLAN

Currently, a lot of research is done to find a way to enable the use of WLAN signals for indoor positioning and navigation. Even companies like Apple and Google are working on this issue and already provide systems of this kind like Skyhook and Indoor Maps. The reason for this huge interest is simple: WLAN signals are available in nearly all relevant areas where indoor positioning is needed (e.g., museums, car parks, office

buildings etc.). Thus, no additional infrastructure is needed to offer an IPS. WLAN signals penetrate trough walls and have a rather good range of up to 50 m. With more or less effort, many methods like ToA, TDoA, AoA and RSS can be used to estimate the position. Another approach which is often used is called CoO (cell of origin). It is primarily based on RSS and uses the signal with the highest strength at a mobile device to assign the device to a specific wireless access point. Afterwards, the device position is assumed to have the same coordinates as the access point. This is a very simple method, however it is only useful for applications with low requirements on accuracy.

Low accuracy is the main disadvantage of WLAN based IPS anyhow. The best accuracies that can be achieved currently lie between one and two meters [69].

Bluetooth

Bluetooth is an IEEE-standard for wireless personal area networks (WPANs). Compared to WLAN, Bluetooth requires lower power and thus Bluetooth devices are of smaller size. The range of Bluetooth signals is limited to about 10 m [23]. The most commonly used method to determine positions is RSS as well as CoO.

ZigBee

ZigBee is a WPAN-standard as well. The main advantages compared to Bluteooth are the even lower power consumption on the one hand and the higher range of 100 m outdoors and 20-30 m indoors on the other hand [23]. However, the ZigBee data rate is smaller than that of Bluetooth. Concerning possible position determination methods there is no significant difference to Bluetooth. Referring to [69], ZigBee based IPS systems have an accuracy of approximately 3 m whereas the accuracy of Bluetooth is limited to detect the room in a building where the mobile device is located.

6.1.4 Optical systems

Laser

In certain aspects, laser-based systems for navigation purposes are comparable to laser-based systems for obstacle detection. On the one hand, the systems are extremely accurate and precise, on the other hand they are very expensive and sensitive to dust and dirt. In section 4.1.4, laser scanners and optical radar have already been discussed in the context of obstacle detection. In principle these methods could also be used for positioning and navigation, however currently only for 2D-applications [93] or without real-time capability [57]. Therefore, this section will not discuss these methods again, but consider two other interesting approaches which seem to be very useful as positioning systems.

Laser tracker. A laser tracker system is a device which is able to measure a distance and two angles. The system consists of a tracker which sends out a laser beam and a reflector. Usually a so-called spherically mounted retro-reflector (SMR) is used. This is a corner-cube mirror which is positioned within a metal sphere. The vertex of the mirror lies in the center of the sphere and the sphere has an aperture to allow the laser beam being reflected by the mirror [30]. The laser source on the tracker is rotatable and can

follow the SMR automatically. The emitted laser beam is reflected by the SMR and reenters the tracker after a certain amount of time. The runtime of the beam is measured either with an interferometer or a so-called absolute distance meter. Two angle encoders measure the orientation of the laser source and therefore the orientation of the laser beam is known as well. This information allows to calculate the exact 3D position of the SMR. To achieve the issue of dynamic tracking (i.e., that the laser source follows the moving SMR automatically), usually a position sensitive device (PSD) is used. This is an optical sensor capable of measuring the position of a light point on its surface [35].

Indoor GPS (iGPS). This is an industrial measurement system which was developed by Nikon. The term iGPS is strictly speaking incorrect, because the principle doesn't have to do anything with GPS at all. iGPS consists of at least three components, namely two transmitters and a receiver which includes a sensor, an amplifier and the position calculation engine. The principle behind iGPS is a sophisticated combination of laser and infrared signals sent out by several transmitters. The system is able to determine the horizontal (azimuth) and vertical angle (elevation) between transmitters and receiver. To determine the elevation, two rotating laser beam planes with an angle of 90° to each other and an opening angle of 30° are emitted (figure 6.1.3). The time difference between the

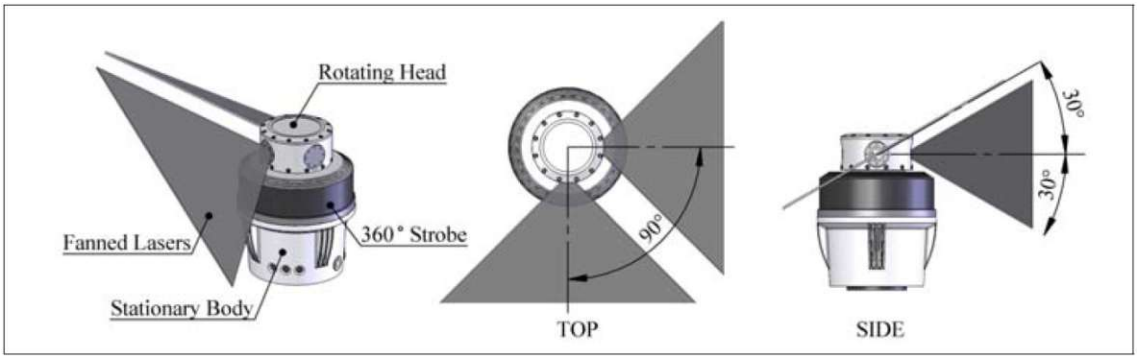

Figure 6.1.3: Arrangement of the laser fans of iGPS. The head is rotating with a frequency of 40 - 50 Hz. The horizontal distance between the planes is different for each vertical angle [73].

two planes reaching the receiver represents its vertical position as it is different for each vertical angle. To determine the azimuth, an omnidirectional infrared pulse is fired every other rotation of the laser beam planes (figure 6.1.4). The horizontal position of the target can be calculated out of the time between the fired infrared pulse and the midpoint of the two laser signals' arrival times.

As the distance between transmitter and receiver is not measured and the position is calculated out of the different angles, at least two line-of-sight transmitters are necessary to gain enough information. Different transmitters can be identified by the receiver due to different rotation frequencies which lie between 40 and 50 Hz. The relatively high rotating frequency makes it easily possible to track moving objects as well. In [43], iGPS was verified to be able to track the position of objects with a speed of 3 m/s with an accuracy of more than 0.3 mm.

As mentioned before, laser based navigation systems are very expensive. To be more

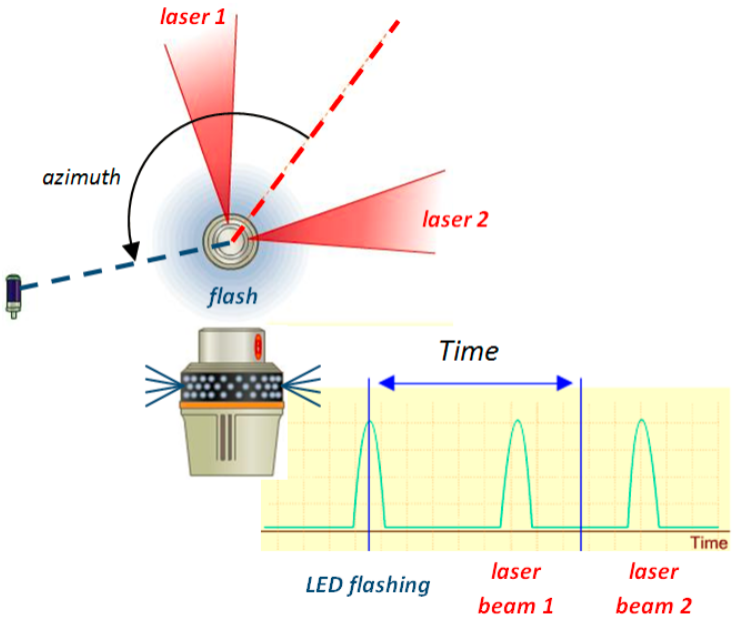

Figure 6.1.4: Determining the azimuth. Every other rotation of the laser fans an infrared pulse is fired. The receiver uses the time difference between the pulse and the midpoint of the two laser signals' arrival times to determine the angle [14].

specific, prices of laser trackers typically start at 100 000 € and an iGPS costs at least 60 000 €, depending on how many components (transmitters or receivers) are used. Another disadvantage is that in contrast to some RF-based systems line-of-sight between transmitter and receiver is always required.

Infrared

For the sake of completeness, infrared-based systems for indoor positioning are introduced in this section although it is rather unlikely that they may be used in steel plants. The principles of infrared-based systems are similar to laser systems with the only difference that they provide lower range and worse accuracy. It is useful to distinguish between two approaches.

Active IR. Active IR uses the transmitter-receiver principle which has been extensively discussed in the previous sections. Infrared receivers are placed in the area where the IPS should operate. A mobile device carries an infrared emitter (a so-called active beacon) and can be located using algorithms based on CoO, AoA or RSS. A popular example is the "Active Badge"-approach presented in [100]. This system can localise people carrying IR emitting badges which are fixed on their clothes. However, the presented system is based on CoO and its accuracy is in the range of about 6 m.

Passive IR. This approach uses the natural emission of radiation of every object with a temperature higher than the absolute zero (also see section 3.1). In other words, no transmitters are required as the objects to localise act as "transmitters" themselves. There

are several sensors that can be used to measure IR radiation, like for example Golay cells, microbolometers (used in thermal cameras), pyroelectric sensors or thermopiles. Except microbolometers, these sensors are very cheap, however not all of them provide stable and reliable results. Golay cells use the expansion of a gas under specific thermal conditions and are extremely sensitive to vibrations. Despite the relatively high cost of more than 1000 € for a microbolometer with a resolution of 160×120 pixels, these sensors also need temperature stabilization. Pyroelectric sensors are only able to detect a flux of radiation rather than an absolute temperature. Thermopiles are serially connected thermocouples and are the most robust sensors presented here.

Passive IR faces several problems which it is difficult to get rid of. Firstly, there is background radiation in every measurement area, i.e., radiation of anything but the object to be detected. Secondly, reflections are a big problem. Especially the radiated IR light of metal surfaces is primarily caused by reflections of background radiation. Changes in the ambient temperature make it even more difficult to compensate these effects. Like in vision-based systems, occlusions may occur and negatively affect the correct functionality of the system too [56].

A market-ready system is called IR.Loc and was developed by Ambiplex. Referring to [69], it provides an accuracy of 20-30 cm with a range of 10 m. However, in [56] three IR.Loc sensors were used to localise people in a room with a size of 5 m × 4.5 m and an accuracy of 80 cm was reached.

6.1.5 Ultrasound systems

Section 4.1.6 described how ultrasound can be used for obstacle detection. In principle it is also possible to use ultrasound for indoor navigation. One problem that may occur in ultrasound-based IPS is the limited range of ultrasound waves of about 10 m. To overcome this challenge, a lot of infrastructure is necessary, i.e., a lot of transmitters or receivers have to be installed, depending on which of the three methods described below is used.

Active US. Active ultrasound systems work with the same principle as active IR. Several receivers are mounted in the environment of a mobile object. The object carries an ultrasound transmitter. Systems like Sonitor IPS, Marvelmind Indoor GPS or Hexamite HX7 provide an accuracy in the range of a few centimeters. However, as with all other systems based on the transmitter-receiver principle, this of course depends on the amount of receivers used and the surrounding conditions [69].

Passive US. The principle of passive ultrasound systems cannot be compared to the one of passive infrared systems. In passive US, permanently installed transmitters broadcast a signal to a mobile receiving (passive) device. In most cases TDoA is used to determine the current position. In 2005, the MIT developed an US-based IPS called Cricket. The performance of this system was evaluated in [84]. It came out that the error is about 5 % for a real distance of 1 m and linearly grows up to 9 % for a real distance of 5 m.

Echolocation. This principle is similar to biosonar which is used by bats. An ultrasound transceiver transmits a signal and builds a picture of its environment due to the received echo. The method is still in research phase, however it could be shown that the method in principle has potential in the future. In [54], echolocation was used to identify

individual rooms with an accuracy of 97.8 %.

6.1.6 Cameras

On the one hand, cameras are a very cheap and promising technology to perform indoor positioning and navigation. On the other hand, camera vision is an extremely challenging research field and still suffers from many difficulties. However, currently there are many vision based navigation approaches available and it is likely that the number will further increase within the next years.

In general, camera systems can be divided into those which need to know the structure of the environment beforehand, i.e., which need a three dimensional model of their environment and those which do not need a global representation of their environment [34]. The paragraphs below give a brief overview about the properties of these two approaches.

Map-based navigation systems

These systems can further be divided into metric map-using systems, metric map-building systems and topological map-based systems.

Metric map-using systems need the input of a map before the start of the principal navigation task. The map can either be constructed by hand with the help of available software tools or based on images that were taken with a single or stereo camera either by the robot that should be navigated or manually by a person. The map is divided into cells and includes information about the exact position of every single cell in a predefined coordinate system. Hence, distances and angles between cells are known as well.

Metric map-building systems are able to create maps online in a training phase before the navigation task. Similar systems, which fall in the same category, are able to build a map and self-localise simultaneously. The so-called SLAM-algorithm (simultaneous localisation and mapping) may be the most popular approach for this issue. Another modification of such a system is presented in [58], where a robot is manually navigated along a specific path and simultaneously builds a map. Afterwards it is able to follow the same path autonomously.

Topological map-based systems are more abstract and require a map that represents the environment based on a graph, not on a 3D-structure. Characteristic features or areas in the environment are represented by nodes. The nodes are connected via lines representing either distances or times between nodes. The advantage of topological map-based systems is that they need much less computation power and thus, the navigation process can be accelerated. An adverse property is that they cannot be used for additional tasks such as obstacle detection as the map does not deliver explicit information about free space.

As soon as the map has been successfully created, the navigation process itself can be started. In most cases the first step is to determine the starting point of the mobile device. The simplest but less flexible way is to always start from the same point with known coordinates. This method would be applicable for a drone which has to perform a measurement flight and returns to a base station afterwards. Another possibility is to search the best match of the camera image in the map which can be time consuming, especially in big areas. In the second step, corresponding points and areas in the camera image and map are searched. In the third step, the necessary information, e.g., the absolute position of a specific cell, is extracted out of the map. Eventually, the position and orientation of the camera is determined by using this information and the relative

position of the camera to the corresponding cell in the map, which has to be calculated out of the camera image as well [65]. Obviously, this last step as well as the quality of the map are crucial for good accuracy.

Typically, the accuracy of map-based camera systems is in the area of decimeters [69].

Map-less navigation systems

Map-less solutions use different visual references in a camera image to determine the camera's position. Generally speaking, these systems are more robust with respect to weak illumination as well as changes of illumination. However, to guarantee the functionality of the system, line-of-sight to a few reference points is required.

The different systems primarily can be distinguished from the used reference. One possibility is to project patterns on objects in the camera's environment. The advantage is that the targets do not have to be physically deployed and they cannot become unrecognisable because of dust or other environmental impacts. Furthermore it is possible to project the pattern on a big area that it is ever-present in the view of the camera. One disadvantage is of course that one or more projectors are necessary which are in general more expensive and less robust than physically deployed targets. In [60], accuracies of a few cm could be reached with this technology.

A second method is the use of coded targets. These can be QR-codes or other special patterns which are placed in the mobile device's area of operation. Each target can be identified unambiguously and the exact position of each target is known. If there is line-of-sight to at least three targets, the distances to each target can be calculated and afterwards positioning can be done with multilateration. In the case that there is line-of-sight to only one target, positioning can be determined by calculating the relative position (including distance and angles) between camera and target. However, this task is much more complex than a position calculation with three or more visible targets.

Thirdly, a model-based approach is possible. This means that models of special objects in the operating area are built beforehand and later on identified in the camera image. The positioning process itself works in the same way as with coded targets. However, both methods suffer of the problem that there will not be any positional information available if there is no target in the camera's field of view. This makes target-based systems less accurate and reliable than projection-based ones [60].

6.1.7 Pseudolites

The term pseudolite is a portmanteau out of the words pseudo and satellite. A pseudolite is a terrestrial sender emitting signals that are similar to those of satellites. These signals can be used for navigation purposes in the same way GPS signals from satellites are used. The position of a so-called rover (receiver) can be determined by the arrival times of several pseudolite signals (TDoA). Typically, pseudolites are used to improve accuracy of GNSS, but also for applications where GNSS cannot be used.

In general, there are two approaches for pseudolite navigation systems. The easiest way is to use GNSS frequencies for pseudolite signals. This allows an easy improvement of accuracy of existing GNSS, because from the point of view of a rover, a pseudolite looks exactly like an additional satellite with better signal quality than usual. However, for juridical reasons it is in many cases difficult to use GNSS frequencies for pseudolite signals. Thus, a second approach is to utilise frequencies in the ISM band for pseudolite signals.

The advantage is the ability of these signals to penetrate through walls. Nevertheless, the main drawback is that special rovers are required.

The most popular market-ready pseudolite navigation system was developed by Locata. It uses frequencies in the ISM band and provides special rovers which can receive both GNSS and pseudolite signals. In [31], the system was used in a steel plant to track a crane inside a metal warehouse. Four pseudolites were used to localise the crane in a working area of about $23 \times 33\,\mathrm{m}^2$. A remarkable accuracy in cm-level could be reached.

In [32], the strength of Locata in non-line-of-sight applications was evaluated. Five pseudolites mounted in the environment of a building were used for positioning of a rover inside the building, which means that the signals had to pass through the whole structure of the building, i.e., several walls and the tin roof. To determine accuracy, both a static and kinematic test were done. In the static test, the rover stayed in his position for a certain amount of time and accuracies of sub-cm level could be reached. To determine kinematic accuracy, a floor plan of the building was used. It could be seen that the system is precise enough to correctly identify the corridor or room where the rover was.

Pseudolites are a powerful technology for positioning and navigation which provide both high range and accuracy. Disadvantages are the sensitivity to multipath interference, the necessary exact time synchronization and the high cost which of course grows with the number of transmitters used.

6.2 Summary

This chapter concentrated on possible systems that could be used to navigate a UAV autonomously through a steel plant. RF-based technologies like UWB and RFID seem to be promising, however they are partly still in a deep research phase. The solely use of dead reckoning is impossible because of the unavoidable drift, but it could be extremely useful in combination with another technology. Like for obstacle detection, optical systems are very accurate, the problem is that they require line-of-sight and furthermore are extremely expensive. Ultrasonic systems suffer of low range and strong sensitivity to multipath interference. Camera-based systems may be the most flexible solutions, however they are complex and still in a research phase. Table 6.2.1 compares the different technologies. Methods which have already been considered to be useless in the particular section above (passive RFID, WLAN etc.) are not mentioned in the table. The column **cost** only refers to hardware cost, software that has to be developed (e.g., for camera systems) is not taken into account. Furthermore, this information should be seen as an minimum value as the real price depends on the specific system (e.g., how many receivers/transmitters are used). The **range**- and **LoS**-columns are relevant for each technology consisting of at least two interdependent components. The **range** as well as the **accuracy** of a system can be seen as an approximation, as they also depend on the specific configuration to a certain extent.

Table 6.2.1 shows that there is no system providing outraging advantages to the others in all aspects. E.g., UWB is pretty cheap, accurate and robust, however it is not yet a well-engineered method. Systems with pseudolites or lasers are market-ready, however they are expensive. Eventually, the decision about which technology fits best can be made as soon as requirements like cost, time-to-market etc. have been defined.

	cost	range	accuracy	LoS required	state of development	note
dead reckoning	10 € - 1 M€	-	-	-	well-engineered	unavoidable drift
UWB	< 10 k€	150 m	< 30 cm	no	research	lower accuracy with NLoS
active RFID	< 10 k€	100 m	meter-level	no	well-engineered	
lasertracker	> 100 k€	300 - 400 m	µm	yes	well-engineered	
iGPS	> 60 k€	30 - 40 m	< 1 mm	yes	well-engineered	
camera: map-based	< 10 k€	-	cm-dm	-	research	high software cost
camera: map-less	< 10 k€	visibility	cm-dm	yes	research	high software cost
pseudolites	> 10 k€	50 km	2 cm	no	well-engineered	lower accuracy with NLoS

Table 6.2.1: Comparison of different indoor positioning technologies. Green marked entries indicate the use for the drone application in a steel plant, red marked entries speak against it.

7 Conclusion and Future Outlook

The aim of this thesis was to evaluate the feasibility of the use of autonomous UAVs in steel plants. In chapter 2, the most important requirements were defined using a specialised layer model for Industry 4.0 applications. In the further chapters, it was investigated whether these requirements, which are a sufficient resilience to the harsh environmental conditions in steel plants, an automatic obstacle detection and autonomous navigation which is not based on GPS, could be fulfilled. The investigation was done with exhaustive literature research about the current state of the art, practical experiments as well as mathematical modelling. As a final statement it can be said that there were not found any physical or technical barriers making the use and realization of UAVs in steel plants infeasible. However, the practical implementation of such an innovative product of course implies many interesting challenges and unknown factors. Hence, besides technical knowledge and creativity, a lot of of temporal and financial expenditure will be necessary. Especially the two latter issues were only considered sporadically in this thesis, nevertheless they are of great interest for the promoter of a project in which the UAV is realised. For that reason, this chapter gives several possible configurations of the UAV together with an estimation of time and cost in table 7.0.1.

It should be mentioned that the **cost**-column in table 7.0.1 refers to hardware cost only. Expenses for additionally required research, development and construction are implicitly given by the estimated time.

The aim of table 7.0.1 is not to give a detailed cost and time schedule for a project in which the autonomous UAV is realised. Especially the required time cannot really be estimated meaningfully as there always occur additional problems and challenges that cannot be considered beforehand. However, the table should rather convey an idea of how time, cost and quality of the result may correlate [26].

One possibility is to use expensive and well-engineered equipment with good performance, like laser-trackers. It seems to be rather easy to realize an indoor positioning system with such powerful devices and also the required time would be comparatively low. However, it is most likely that the high price of the laser-trackers would make the UAV-system unsaleable.

The usage of camera-based equipment would reduce the hardware cost but extend the required development time. For configuration 3 in table 7.0.1 both cost and time are quite low, however the system would perform worse (e.g., regarding accuracy of the obstacle detection system) than with configuration 1 and it would be less flexible than with configuration 2.

In the case of a further pursuit of the innovative approach of using an autonomous UAV in steel plants to measure remaining lining thickness, an important step in subsequent feasibility checks would be to gain relevant data about the environmental conditions in steel plants. This includes measurements of temperature at possible UAV positions during a flight as well as measurements of wind forces. It would also be helpful to perform test

element	specification	cost	estimated implementation time
UAV without intelligence	remote-controlled UAV, constructed of commercially available components	$\sim$ 10 000 €	2 - 3 months
configuration 1: laser-based			
obstacle detection system	e.g., SICK S300 MINI; 2 devices are necessary due to the coverage area	$\sim$ 20 000 €	4 - 5 months
navigation system	laser-tracker	$>$ 100 000 €	2 - 3 months
configuration 2: camera-based			
obstacle detection system	stereo camera, e.g., POINTGREY BUMBLEBEE XB3; more than 1 camera required for 360°-view	$\sim$ 7000 €	1.5 - 2 years
navigation system	same camera as for obstacle detection can be used	-	2 - 3 years
configuration 3: various technologies			
obstacle detection system	sonar combined with infrared (e.g., some TERARANGER ONE and ultrasonic sensor modules	$\sim$ 1500 €	5 - 6 months
navigation system	UWB (e.g., DECAWAVE TREK 1000	$\sim$ 3000 €	5 - 6 months

Table 7.0.1: Possible configurations of the UAV. Cost and time effort for a UAV without intelligence (i.e., a remote-controlled UAV that can be extended with the required sensors and other hardware) have to be considered independently of the specific configuration.

flights similar to the one in section 3.3 in a steel plant, as this would answer more questions concerning the behaviour of the drone during its operation. Furthermore, the system which was developed and tested in chapter 5 could be improved. Different sound frequencies could be used for each sensor to avoid crosstalk. A practical test would show if this could raise any other challenges that are not considered beforehand due to hypothetical assumptions. Additionally, a practical test of some indoor positioning technologies presented in this thesis is advisable, especially for systems that are already commercially available but still

not very well established, like for example UWB.

List of Abbreviations

AC	alternating current
ADC	analogue-to-digital converter
AoA	angle of arrival
APO	Automatic Process Optimisation
BOF	basic oxygen converter
CoO	cell of origin
DC	direct current
DRI	direct-reduced iron
EAF	electric arc furnace
ECC	European Communications Committee
FMCW	frequency modulated continuous wave
FTP	File Transfer Protocol
GNSS	global navigation satellite systems
GPIO	general-purpose input/output
GPS	global positioning system
IEEE	Institute of Electrical and Electronics Engineers
iGPS	indoor global positioning system
IIC	Industrial Internet Consortium
IIRA	Industrial Internet Reference Architecture
IIT	Institute for Innovation and Technology
IMU	inertial measurement unit
IPM	inverse perspective method
IPS	indoor positioning system
IR	infrared
ISR	interrupt service routine
LD	Linz-Donawitz
LED	light emitting diode
LoS	line of sight
MEMS	micro electro-mechanical systems
MIT	Massachusetts Institute of Technology
MUSIC	multiple signal classification

NLoS	non line of sight
OF	optical flow
OSI	Open Systems Interconnection
PSD	position sensitive device
QR	quick response
RAMI 4.0	Reference Architecture Model Industry 4.0
RFID	radio frequency identification
RGB	red-green-blue
RSS	received signal strength
SfM	structure from motion
SIFT	scale-invariant feature transform
SLAM	simultaneous localisation and mapping
SMR	spherically mounted retro-reflector
SPI	serial peripheral interface
TCP/IP	Transmission Control Protocol/Internet Protocol
TDoA	time difference of arrival
ToA	time of arrival
ToF	time of flight
UAV	unmanned aerial vehicle
US	ultrasound
USB	Universal Serial Bus
UWB	ultra-wideband
WLAN	wireless local area network
WPAN	wireless personal area network
ZVEI	Zentralverband Elektrotechnik- und Elektronikindustrie

List of Tables

3.1.1 Important properties of most common battery types 33
3.2.1 Sampling points for calculation of wind resistance 35

4.2.1 Comparison of different obstacle detection systems 57

6.1.1 Drifts of low-cost and high-end dead reckoning systems 79
6.2.1 Comparison of different indoor positioning technologies 90

7.0.1 Possible configurations of the UAV 92

List of Figures

1.1.1 Lined vessels: BOF, EAF, ladle 2
1.1.2 Manual gunning maintenance 3
1.3.1 Input- and output-parameters of APO 4

2.2.1 Visual roadmap for Pervasive Computing 8
2.5.1 RAMI 4.0 12
2.6.1 RAMI 4.0 applied to the UAV 14

3.1.1 Measuring position of the UAV 18
3.1.2 Heat exchange between two surfaces 20
3.1.3 Parameters of heat radiation model 22
3.1.4 View factor as a function of h 24
3.1.5 View factor as a function of W 25
3.1.6 Determination of the heat transfer coefficient 27
3.1.7 Structure of a lithium-ion battery cell 31
3.2.1 Drone model to calculate wind resistance 35
3.2.2 Drag coefficient as a function of the Reynolds number 36
3.2.3 F_w depending on wind speed and drone configuration 36
3.3.1 Wiring of the diode and the push button 38
3.3.2 Wiring of the MCP3008 and the PT1000 element 39
3.3.3 Temperature logger 43
3.3.4 DJI Mavic Pro with mounted temperature logger 44
3.3.5 Test flight: temperature 45
3.3.6 Test flight: wind 46

4.1.1 Barber's pole illusion 48
4.1.2 Typical parameters of a stereo camera 50
4.1.3 Principle of structured-light 52
4.1.4 Principle of laser triangulation 54

5.1.1 Ultrasonic measurement setup 60
5.1.2 Crosstalk of neighboured ultrasonic sensors 60
5.3.1 Sensor arrangement: static measurement 64
5.3.2 Static measurement results with a $50 \times 30\,\mathrm{cm}^2$ object 65
5.3.3 Static measurement results with a $20 \times 20\,\mathrm{cm}^2$ object 67
5.3.4 Static measurement results with a $10 \times 10\,\mathrm{cm}^2$ object 68
5.4.1 Arrangement of obstacles for scenario 1 70
5.4.2 Dynamic measurement of scenario 1 70
5.4.3 Dynamic measurement of scenario 2: side view 71
5.4.4 Measurement results of scenario 1 with 3 modules 72
5.4.5 Measurement results of scenario 1 with 1 module 72

5.4.6 Measurement results of scenario 2 73
5.4.7 Arrangement to measure angular dependence 74
5.4.8 Measurement results for rotational movement 75

6.1.1 Principle of dead reckoning 78
6.1.2 Principle of the MUSIC algorithm 80
6.1.3 Determining the elevation with iGPS 84
6.1.4 Determining the azimuth with iGPS 85

Bibliography

[1] Datasheet: Arduino UNO. Available at: http://digital.csic.es/bitstream/10261/127788/7/D-c-%20Arduino%20uno.pdf. Accessed 29-March-2017.

[2] Datasheet: MCP3004/3008. Available at: https://cdn-shop.adafruit.com/datasheets/MCP3008.pdf. Accessed 27-June-2017.

[3] Datasheet: Platinum Resistance Temperature Detector M1020. Available at: https://www.heraeus.com/media/media/group/doc_group/products_1/hst/m_sensors/us_3/M1020_HST-USA.pdf. Accessed 28-June-2017.

[4] Guide to comparing gyro and IMU technologies – micro electro-mechanical systems and fiber optic gyros. Available at: http://www.kvh.com/ViewAttachment.aspx?guidID={A4A8B05C-D372-41EA-B9C6-D7BCC4F40769}. Published by: KVH Industries Inc. Accessed 04-April-2017.

[5] Preliminary datasheet: XMC4700/XMC4800 microcontroller series. Available at: http://www.infineon.com/dgdl/Infineon-XMC4700_XMC4800_DATA_SHEET-ATI-v00_06-EN.pdf?fileId=5546d4624d6fc3d5014da01e39e361c6. Accessed 07-June-2017.

[6] Product brief: D54250WYK Intel NUC Kit. Available at: http://resources.mini-box.com/online/SYS-NUC-D54250WYK1/SYS-NUC-D54250WYK1-specs.pdf. Accessed 07-June-2017.

[7] Specification sheet: TeraRanger One. Available at: http://www.teraranger.com/wp-content/uploads/2016/01/TeraRanger-One-Specification-Sheet1.pdf. Accessed 12-July-2017.

[8] SU Emissionsgrad Tabelle. Available at: http://www.bossert-weissinger.de/pdf/kataloge_fluke_su-emmissiongrad.pdf. Published by: Frank Bossert Industrievertretungen. Accessed 29-May-2017.

[9] Using accelerometers to estimate position and velocity. Available at: http://www.chrobotics.com/library/accel-position-velocity. Published by: CH Robotics, Payson, UT. Accessed 04-April-2017.

[10] Visual Roadmap basierter Foresight Workshop. Available at: http://www.camara-alemana.org.pe/downloads/151124-Broschure-Visual-Roadmap.pdf. Published by: iit - Institute of Innovation and Technology. Accessed 10-March-2017 .

[11] Ultraschall Näherungssensoren. In *Grundbegriffe der Sensorik*, chapter 6. Rockwell Automation, February 2001.

[12] Datasheet: distance measuring sensor unit GP2Y0A710K0F. Available at: https://acroname.com/sites/default/files/assets/sharp_gp2y0a710yk0f_datasheet.pdf, December 2006. Accessed 12-July-2017.

[13] DIN EN 60751:2009-05. Industrielle Platin-Widerstandsthermometer und Platin-Temperatursensoren. 2009.

[14] Infoletter: The iGPS system. Available at: http://www.amrikart.com/infoletter-details/article/2013-02-11/The-iGPS-system/The-iGPS-system, February 2013. Published by: Amrikart Ultraprecision. Accessed 06-April-2017.

[15] Product information: Decawave DWM 1000. Available at: http://www.decawave.com/sites/default/files/product-pdf/dwm1000-product-brief.pdf, 2013. Accessed 05-April-2017.

[16] IMU errors and their effects. Published by: Novatel Wireless Inc., February 2014. APN-064, Rev A.

[17] Ubisense research package fact sheet. Available at: http://www.rfidstore.it/it/sistemi-rtls/32-academic-research-kit.html, 2014. Accessed 05-April-2017.

[18] Industrial Internet Reference Architecture. June 2015.

[19] *Refractory competence for the steel industry*. Number 05/2015-250-D/E. RHI AG, Wienerbergstrasse 9, 1100 Vienna, Austria, 2015.

[20] Steel industry by-products. *Fact sheet world steel association*, June 2016. Published by: World Steel Association.

[21] Datasheet: S32B-2011BA—S300 mini standard. Available at: https://www.sick.com/media/pdf/0/40/140/dataSheet_S32B-2011BA_1050932_en.pdf, March 2017. Accessed 12-April-2017.

[22] P. Adolphs, H. Bedenbender, D. Dirzus, H. Huhle, and M. Ehlich. Referenzarchitekturmodell Industrie 4.0 (RAMI 4.0). *Statusreport VDI und ZVEI*, April 2015.

[23] A. Alarifi, A. Al-Salman, M. Alsaleh, A. Alnafessah, S. Al-Hadhrami, M. A. Al-Ammar, and H. S. Al-Khalifa. Ultra wideband indoor positioning technologies: Analysis and recent advances. *Sensors*, 16(5):707, 2016.

[24] M.-C. Amann, T. Bosch, M. Lescure, R. Myllyla, and M. Rioux. Laser ranging: a critical review of usual techniques for distance measurement. *Optical engineering*, 40(1):10–19, 2001.

[25] N. Appiah and N. Bandaru. Obstacle detection using stereo vision for self-driving cars. Stanford University, Department of Mechanical Engineering, 2011.

[26] R. Atkinson. Project management: cost, time and quality, two best guesses and a phenomenon, its time to accept other success criteria. *International journal of project management*, 17(6):337–342, 1999.

[27] G. Babiel. *Elektrische Antriebe in der Fahrzeugtechnik*. Springer, 2009.

[28] H. D. Baehr and K. Stephan. *Heat and mass transfer*. Springer-Verlag Berlin Heidelberg, second edition, 2006.

[29] D. Ball, B. Upcroft, G. Wyeth, P. Corke, A. English, P. Ross, T. Patten, R. Fitch, S. Sukkarieh, and A. Bate. Vision-based obstacle detection and navigation for an agricultural robot. *Journal of Field Robotics*, 2016.

[30] M. Bame. Spherically mounted retroreflector edge adapter, Oct. 9 2001. US Patent 6,299,122.

[31] J. Barnes, C. Rizos, M. Kanli, D. Small, G. Voigt, N. Gambale, J. Lamance, T. Nunan, and C. Reid. Indoor industrial machine guidance using locata: A pilot study at bluescope steel. In *60th Annual Meeting of the US Inst. of Navigation*, pages 533–540, 2004.

[32] J. Barnes, C. Rizos, J. Wang, D. Small, G. Voigt, and N. Gambale. Locatanet: Intelligent time-synchronised pseudolite transceivers for cm-level stand-alone positioning. Satellite Navigation and Positioning (SNAP) Group, School of Surveying and Spatial Information Systems, The University of New South Wales (UNSW), Australia, 2003.

[33] A. Benini, A. Mancini, A. Marinelli, and S. Longhi. A biased extended Kalman filter for indoor localization of a mobile agent using low-cost IMU and UWB wireless sensor network. *IFAC Proceedings Volumes*, 45(22):735–740, 2012.

[34] F. Bonin-Font, A. Ortiz, and G. Oliver. Visual navigation for mobile robots: A survey. *Journal of intelligent and robotic systems*, 53(3):263, 2008.

[35] B. Bridges. How laser trackers work. *Quality Digest*, 25, June 2009.

[36] F. Brunet. *Contributions to parametric image registration and 3D surface reconstruction*. PhD thesis, Université d'Auvergne, November 2010.

[37] Y. Chen, Y. He, and M. Zhou. Modeling and control of a quadrotor helicopter system under impact of wind field. *Research Journal of Applied Sciences, Engineering and Technology*, 17(6):3214–3221, 2013.

[38] D. Conrad and G. N. DeSouza. Homography-based ground plane detection for mobile robot navigation using a Modified EM algorithm. In *IEEE International Conference on Robotics and Automation*, pages 910–915, 2010.

[39] C. Costopoulos, A. J. Brown, Z. Teng, S. P. Hoole, N. E. West, H. Samady, and M. R. Bennett. Intravascular ultrasound and optical coherence tomography imaging of coronary atherosclerosis. *The international journal of cardiovascular imaging*, 32(1):189–200, 2016.

[40] A. J. Davison. Real-time simultaneous localisation and mapping with a single camera. In *Proceedings Ninth IEEE International Conference on Computer Vision*, volume 2, pages 1403–1410, 2003.

[41] J. D. Day and H. Zimmermann. The OSI reference model. *Proceedings of the IEEE*, 71(12):1334–1340, 1983.

[42] J. Delon and B. Rougé. Small baseline stereovision. *Journal of Mathematical Imaging and Vision*, 28(3):209–223, 2007.

[43] C. Depenthal. Path tracking with iGPS. In *International Conference on Indoor Positioning and Indoor Navigation*, pages 1–6. IEEE, September 2010.

[44] N. A. Ebrahim. Virtual R&D teams: A new model for product development. *International Journal of Innovation*, 3(2):1, 2015.

[45] H. Elmer. *Improved ultrasonic distance measurement in air*. PhD thesis, Vienna University of Technology, September 2005.

[46] P. Fleischmann and K. Berns. A stereo vision based obstacle detection system for agricultural applications. In *Field and Service Robotics*, pages 217–231. Springer, 2016.

[47] M. Hankel and B. Rexroth. The Reference Architectural Model Industrie 4.0 (RAMI 4.0). 2015.

[48] E. A. Hartmann and M. Bovenschulte. Skills needs analysis for "Industry 4.0" based on roadmaps for smart systems. In *Using Technology Foresights for Identifying Future Skills Needs. Global Workshop Proceedings*, pages 24–36, 2013.

[49] S. F. Hoerner. *Fluid dynamic drag - theoretical, experimental and statistical information*. Published by the author, 1965.

[50] G. Hunter, R. Okojie, P. Neudeck, G. Beheim, G. Ponchak, G. Fralick, J. Wrbanek, and L. Chen. High temperature electronics, communications, and supporting technologies for venus missions. *Electrical and Electronic Engineering*, pages 27–30, 2006.

[51] F. P. Incropera, A. S. Lavine, T. L. Bergman, and D. P. DeWitt. *Fundamentals of heat and mass transfer*. Wiley, 2007.

[52] B. Jachimczyk, D. Dziak, and W. J. Kulesza. Performance analysis of an RFID-based 3D indoor positioning system combining scene analysis and neural network methods. *Scientific Papers of Faculty of Electrical and Control Engineering Gdansk University of Technology*, (34):29–33, 2013.

[53] C. Jandl. Introduction to the processes of steelmaking. RHI AG, Basic training presentation, 2002.

[54] R. Jia, M. Jin, and C. J. Spanos. SoundLoc: Acoustic method for indoor localization without infrastructure. *ArXiv e-prints*, 2014.

[55] M. P. Jones. HC-SR04 user guide. Available at: https://www.mpja.com/download/hc-sr04_ultrasonic_module_user_guidejohn.pdf. Accessed 29-March-2017.

[56] J. Kemper and H. Linde. Challenges of passive infrared indoor localization. In *5th Workshop on Positioning, Navigation and Communication*, pages 63–70. IEEE, 2008.

[57] K. Khoshelham. Automated localization of a laser scanner in indoor environments using planar objects. In *International Conference on Indoor Positioning and Indoor Navigation (IPIN)*, pages 1–7. IEEE, 2010.

[58] K. Kidono, J. Miura, and Y. Shirai. Autonomous visual navigation of a mobile robot using a human-guided experience. *Robotics and Autonomous Systems*, 40(2):121–130, 2002.

[59] S. Kim and H. B. Kim. High resolution mobile robot obstacle detection using low directivity ultrasonic sensor ring. In *Advanced Intelligent Computing Theories and Applications. With Aspects of Artificial Intelligence*, pages 426–433. Springer, 2010.

[60] M. Köhler, S. Patel, J. Summet, E. Stuntebeck, and G. Abowd. Tracksense: Infrastructure free precise indoor positioning using projected patterns. *Pervasive Computing*, pages 334–350, 2007.

[61] R. Korthauer. *Handbuch Lithium-Ionen Batterien*. Springer, 2013.

[62] M. Kotaru, K. Joshi, D. Bharadia, and S. Katti. Spotfi: Decimeter level localization using WiFi. In *ACM SIGCOMM Computer Communication Review*, volume 45, pages 269–282. ACM, 2015.

[63] A. Kugi, W. Kemmetmüller, A. Steinböck, and T. Glück. Modellbildung. Vorlesungsskriptum, TU Wien, Institut für Automatisierungs- und Regelungstechnik, 2017.

[64] G. Lammer. Refractory control system APO. RHI AG, presentation, March 2013.

[65] X. Li, J. Wang, A. Olesk, N. Knight, and W. Ding. Indoor positioning within a single camera and 3D maps. In *Ubiquitous Positioning Indoor Navigation and Location Based Service (UPINLBS)*, pages 1–9. IEEE, 2010.

[66] S.-W. Lin, B. Miller, J. Durand, G. Bleakley, A. Chigani, R. Martin, B. Murphy, and M. Crawford. *The Industrial Internet of Things volume G1: reference architecture*. Industrial Internet Consortium IIC, January 2017.

[67] J. Lipnack and J. Stamps. Virtual teams: The new way to work. *Strategy & Leadership*, 27(1):14–19, 1999.

[68] R. Mautz. Overview of current indoor positioning systems. *Geodezija ir kartografija*, 35(1):18–22, 2009.

[69] R. Mautz. Indoor positioning technologies. ETH Zurich, Department of Civil, Environmental and Geomatic Engineering, Institute of Geodesy and Photogrammetry Zurich, 2012.

[70] W. H. McAdams. *Heat transmission*. McGraw-Hill, third edition, 1958.

[71] E. Mok, L. Xia, G. Retscher, and H. Tian. A case study on the feasibility and performance of an UWB-AoA real time location system for resources management of civil construction projects. *Journal of Applied Geodesy*, 4(1):23–32, 2010.

[72] E. Mouragnon, M. Lhuillier, M. Dhome, F. Dekeyser, and P. Sayd. Generic and real-rime structure from motion using local bundle adjustment. *Image and Vision Computing*, 27:1178–1193, 2009.

[73] J. E. Muelaner, Z. Wang, J. Jamshidi, P. Maropoulos, A. R. Mileham, E. Hughes, and A. Forbes. iGPS – An initial assessment of technical and deployment capability. In *3rd International Conference on Manufacturing Engineering*, pages 805–810. University of Bath, 2008.

[74] D. Murray and J. J. Little. Using real-time stereo vision for mobile robot navigation. *Autonomous Robots*, 8(2):161–171, 2000.

[75] B. Neubauer. Basic bricks for steel industry incl. alumina-carbon-bricks. RHI AG, presentation, 2016.

[76] A. Nüchter. *3D robotic mapping: the simultaneous localization and mapping problem with six degrees of freedom*, volume 52. Springer, 2008.

[77] H. S. Oluwatosin. Client-server model. *IOSR Journal of Computer Engineering (IOSR-JCE)*, 16(1):67–71, 2014.

[78] H.-H. Pham, T.-L. Le, and N. Vuillerme. Real-time obstacle detection system in indoor environment for the visually impaired using Microsoft Kinect sensor. *Journal of Sensors*, 2016.

[79] S. A. Raza and W. Gueaieb. Intelligent flight control of an autonomous quadrotor. In *Motion Control*. InTech, 2010.

[80] C. R. Russell, J. Jung, G. Willink, and B. Glasner. Wind tunnel and hover performance test results for multicopter UAS vehicles. *American Helicopter Society (AHS) International Annual Forum and Technology Display*, May 2016.

[81] A. M. Sabatini. Quaternion-based extended Kalman filter for determining orientation by inertial and magnetic sensing. *IEEE Transactions on Biomedical Engineering*, 53(7):1346–1356, 2006.

[82] J. Sagar and A. Visser. Obstacle avoidance by combining background subtraction, optical flow and proximity estimation. In *International Micro Air Vehicle (IMAV) Conference and Competition*. Delft University of Technology, August 2014.

[83] M. Sak, N. Duric, P. Littrup, M. E. Sherman, and G. L. Gierach. Using ultrasound tomography to identify the distributions of density throughout the breast. In *SPIE Medical Imaging*. International Society for Optics and Photonics, 2016.

[84] H. S. Sameshima and E. Katz. Experiences with cricket/ultrasound technology for 3-dimensional locationing within an indoor smart environment. 2009. Published by: Carnegie Mellon University – Silicon Valley Campus.

[85] F. Schiano, J. Alonso-Mora, K. Rudin, P. Beardsley, R. Siegwart, and B. Siciliano. Towards estimation and correction of wind effects on a quadrotor UAV. In *International Micro Air Vehicle (IMAV) Conference and Competition*. Delft University of Technology, August 2014.

[86] O. Schreer. *Stereoanalyse und Bildsynthese*. Springer, 2005.

[87] T. Sebastian. Temperature effects on torque production and efficiency of PM motors using NdFeB magnets. *IEEE Transactions on Industry Applications*, 31(2):353–357, 1995.

[88] H. E. Siekmann and P. U. Thamsen. *Strömungslehre: Grundlagen*. Springer-Verlag, 2013.

[89] K.-T. Song and J.-H. Huang. Fast optical flow estimation and its application to real-time obstacle avoidance. In *IEEE International Conference on Robotics and Automation*, volume 3, pages 2891–2896. IEEE, 2001.

[90] M. Sterner and I. Stadler. *Energiespeicher-Bedarf, Technologien, Integration*. Springer-Verlag, 2014.

[91] R. Strydom, S. Thurrowgood, and M. Srinivasan. Visual odometry: autonomous UAV navigation using optic flow and stereo. In *Proceedings of Australian Conference on Robotics and Automation*, 2014.

[92] N. Sydney, B. Smyth, and D. A. Paley. Dynamic control of autonomous quadrotor flight in an estimated wind field. In *IEEE 52nd Annual Conference on Decision and Control (CDC)*, pages 3609–3616. IEEE, 2013.

[93] J. Tang, Y. Chen, A. Jaakkola, J. Liu, J. Hyyppä, and H. Hyyppä. Navis - an UGV indoor positioning system using laser scan matching for large-area real-time applications. *Sensors*, 14(7):11805–11824, 2014.

[94] V. H. Tran. Entwicklung und Aufbau eines luftgekoppelten Ultraschall-Inspektionssystems. Master's thesis, Darmstadt University of Technology, 2016.

[95] Verein Deutscher Eisenhüttenleute VDEh, Stahlinstitut. *Stahlfibel*. Verlag Stahleisen, 2007.

[96] A. Viertauer. Metalurgy and customer demands - advanced training. RHI AG, presentation, October 2016.

[97] M. Vossiek, L. Wiebking, P. Gulden, J. Weighardt, and C. Hoffmann. Wireless local positioning-concepts, solutions, applications. In *Radio and Wireless Conference*, pages 219–224. IEEE, 2003.

[98] H.-G. Wagemann and H. Eschrich. *Grundlagen der photovoltaischen Energiewandlung: Solarstrahlung, Halbleitereigenschaften und Solarzellenkonzepte*. Teubner, 1994.

[99] H. Wallach. The direction of motion of straight lines. *Perception*, pages 201–216, 1976.

[100] R. Want and A. Hopper. Active badges and personal interactive computing objects. *IEEE Transactions on Consumer Electronics*, 38(1):10–20, 1992.

[101] M. Westoby, J. Brasington, N. Glasser, M. Hambrey, and J. Reynolds. Structure-from-motion photogrammetry: A low-cost, effective tool for geoscience applications. *Geomorphology*, 179:300–314, 2012.

[102] O. J. Woodman. An introduction to inertial navigation. Technical report, University of Cambridge, Computer Laboratory, 2007.

[103] Z. Zhou, T. Chen, and L. Xu. An improved dead reckoning algorithm for indoor positioning based on inertial sensors. In *International Conference on Electrical, Automation and Mechanical Engineering (EAME)*, May 2015.

[104] H. Zou, H. Wang, L. Xie, and Q.-S. Jia. An RFID indoor positioning system by using weighted path loss and extreme learning machine. In *IEEE 1st International Conference on Cyber-Physical Systems, Networks, and Applications (CPSNA)*, pages 66–71. IEEE, 2013.

Eidesstattliche Erklärung

Hiermit erkläre ich, dass die vorliegende Arbeit gemäß dem Code of Conduct – Regeln zur Sicherung guter wissenschaftlicher Praxis (in der aktuellen Fassung des jeweiligen Mitteilungsblattes der TU Wien), insbesondere ohne unzulässige Hilfe Dritter und ohne Benutzung anderer als der angegebenen Hilfsmittel, angefertigt wurde. Die aus anderen Quellen direkt oder indirekt übernommenen Daten und Konzepte sind unter Angabe der Quelle gekennzeichnet. Die Arbeit wurde bisher weder im In- noch im Ausland in gleicher oder in ähnlicher Form in anderen Prüfungsverfahren vorgelegt.

Wien, im September 2017

Johannes Pagitsch